IN VITRO-DETECTED EARLY EVENTS TO UNRAVEL SPORADIC NEURODEGENERATION

Aleksandar Sebastijanović

Doctoral Dissertation
Jožef Stefan International Postgraduate School
Ljubljana, Slovenia

Supervisor: Prof. Dr. Janez Štrancar, Jožef Stefan Institute, Ljubljana, Slovenia
Co-Supervisor: Asst. Prof. Dr. Iztok Urbančič, Jožef Stefan Institute, Ljubljana, Slovenia

Evaluation Board:
Prof. Dr. Igor Križaj, Chair, IPS and Jožef Stefan Institute, Ljubljana, Slovenia
Prof. Dr. Aleš Fajmut, Member, Faculty of Natural Sciences and Mathematics, University of Maribor, Maribor, Slovenia
Prof. Dr. Shanbeh Narui-Zienolddiny, Member, National Institute for Occupational Health – STAMI, Oslo, Norway

MEDNARODNA PODIPLOMSKA ŠOLA JOŽEFA STEFANA
JOŽEF STEFAN INTERNATIONAL POSTGRADUATE SCHOOL

Aleksandar Sebastijanović

IN VITRO-DETECTED EARLY EVENTS TO UNRAVEL SPORADIC NEURODEGENERATION

Doctoral Dissertation

IN VITRO ODKRITI ZGODNJI DOGODKI ZA RAZUMEVANJE SPORADIČNE NEVRODEGENERACIJE

Doktorska disertacija

Supervisor: Prof. Dr. Janez Štrancar

Co-Supervisor: Asist. Prof. Dr. Iztok Urbančič

Ljubljana, Slovenia, February 2024

Acknowledgments

I extend my deepest gratitude to my mentors Janez and Tilen, whose guidance not only imparted knowledge but also encouraged me to think outside of the box, consistently pushing me to strive for excellence and innovation professionally and privately. Heartfelt thanks to my parents and my sister for their unwavering belief in my abilities, providing the foundation for everything I did and will do in my life. Special appreciation goes to my fiancée, a pillar of support during the toughest moments, offering boundless strength, love, and wisdom that fueled my perseverance. She is my GOAT. This work is a reflection of the collective encouragement and belief bestowed upon me by these remarkable individuals. Thank you for believing in me, my beloved people.

Graphical Abstract

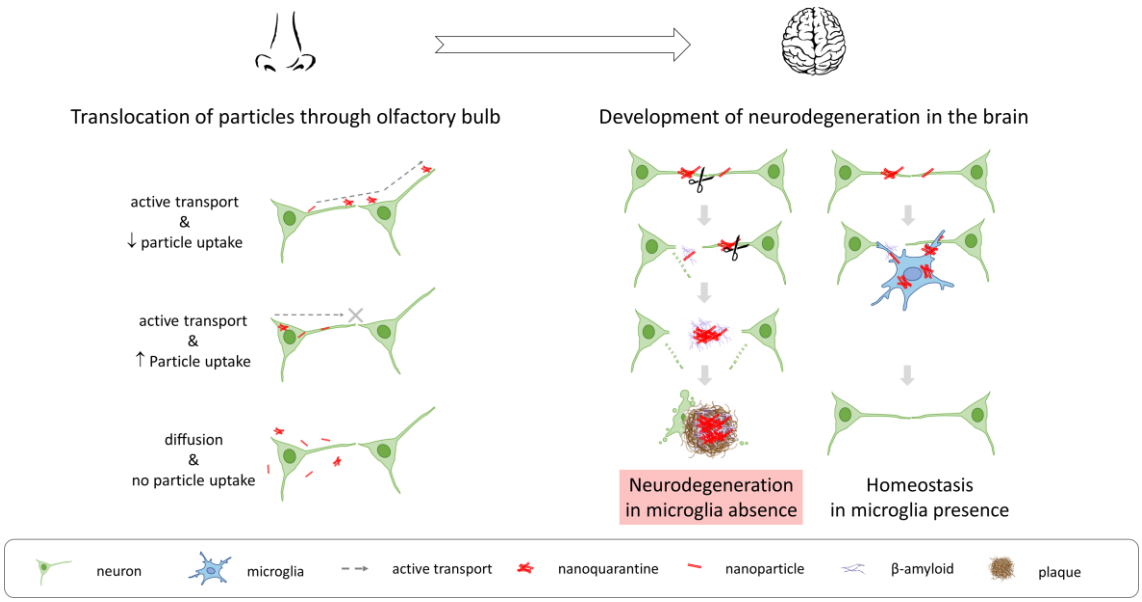

Exposure of neurons to nanoparticles capable of binding to motor proteins via neuronal plasma membrane components but evading internalization results in a long-distance cell-to-cell transport along the neuronal membrane surface. Upon reaching the brain, these nanoparticles inflict structural damage to axons and dendritic spines, triggering the release of Aβ. This sustained damage culminates in neuronal death, with the released Aβ accumulating into plaques resembling those found in Alzheimer's patients, comprising both nanomaterial and other neuronal constituents. In the presence of microglia, these pathological events are omitted due to their removal of hazardous particles through the process of phagocytosis.

Abstract

Alzheimer's disease (AD) is the most prevalent form of dementia, ranking as the 7th deadliest world's disease. Over 99% of cases are triggered by unknown environmental factors. Despite decades of research, the exact cause remains elusive, and effective treatments are yet to emerge.

Recent epidemiological evidence strongly links cognitive decline to exposure to fine airborne particulate matter (PM2.5), hinting at air pollution's potential role in AD pathogenesis. However, the precise relationship between these particles and neurodegeneration remains elusive.

Employing advanced time-lapse microscopy and analysis, we demonstrate potential mechanism of transport of TiO_2 anatase nanotubes from nasal mucosa to the brain after inhalation using a co-culture of immortalized differentiated neuronal SH-SY5Y and microglial HMC3 cell lines. These particles induce structural damage of neurons, triggering key AD hallmarks: amyloid-β (Aβ) plaques, Tau protein aggregation, and neuronal loss. Contrary to common belief, our results suggest the that particles first trigger neuronal structural damage which then translates into pathological changes, with Aβ plaque formation as a consequence. A swift removal of hazardous particles by microglia through phagocytosis reduces axonal damage, neuronal death and results in formation of more compact Aβ plaques, thus mitigating neurodegenerative phenotype observed in monoculture, further strengthening our proposal that neuronal structural damage drives neurodegeneration.

Collectively, we experimentally demonstrate, for the first time, how an environmental factor, like TiO_2 nanotubes, could penetrate the brain and instigate a pathological cascade, resembling AD symptoms observed in human patients.

Povzetek

Alzheimerjeva bolezen je najpogostejša oblika demence in sedma najsmrtonosnejša bolezen na svetu. Več kot 99 % primerov bolezni izzovejo neznani okoljski dejavniki, ki kljub desetletjem raziskav ostajajo skriti, hkrati pa še vedno nimamo učinkovitih zdravil.

Nedavne epidemiološke študije povezujejo upad kognitivnih sposobnosti z izpostavljenostjo finim delcem v zraku (PM2.5), kar nakazuje na možno vlogo onesnaženega zraka pri nastanku Alzheimerjeve bolezni. Vendar pa natančen odnos med temi delci in nevrodegeneracijo ostaja nejasen.

Z uporabo naprednih mikroskopij in analiz naša študija odkriva potencialen mehanizem prenosa nevarnih delcev, TiO_2 nanotub, iz nosne sluznice v možgane po vdihu. Po izpostavitvi diferencirane nevronske SH-SY5Y in mikroglia HMC3 celične linije tem delcem opazimo strukturne poškodbe nevronov, podobne tistim, ki jih najdemo pri bolnikih z Alzheimerjevo boleznijo: amiloida- plaki (Aβ), agregacija tau proteina ter odmiranje nevronov. V nasprotju s splošnim prepričanjem naša časovno razrešena mikroskopija identificira strukturno poškodbo nevronov kot glavnega sprožilca te patološke kaskade, pri čemer je tvorba Aβ plakov le posledica. Poleg tega hitro odstranjevanje teh nevarnih delcev s strani mikroglije s fagocitozo bistveno zmanjša patološke spremembe, kar dodatno podpira našo hipotezo.

Skupno gledano ta študija prvič eksperimentalno kaže, kako lahko okoljski dejavniki, kot so TiO_2 nanotube, pridejo v možgane in sprožijo patološke procese, podobne simptomom Alzheimerjeve bolezni, opaženim pri ljudeh.

Contents

List of Figures

Abbreviations

Aβ	...	Amyloid Beta
AD	...	Alzheimer's disease
APD	...	Avalanche Photodiode Detector
APP	...	Amyloid Precursor Protein
ATP	...	Adenosine Triphosphate
CMDR	...	Cellmask Deep Red
CMO	...	CellMask Orange
CTG	...	Celltracker Green
CTO	...	Celltracker Orange
CTRL	...	Control
DMEM	...	Dulbecco's Modified Eagle's Medium
FBS	...	Fetal Bovine Serum
FOV	...	Field of View
MSD	...	Mean Square Displacement
MWCNT	...	Multi-walled carbon nanotubes
NA	...	Numerical aperture
PBS	...	Phosphate Buffer Solution
PM2.5	...	Particulate Matter 2.5
ROI(s)	...	Region of Interest(s)
rpm	...	Rotations per minute
STED	...	Stimulated Emission Depletion Microscopy

Symbols

g	. . .	gram
h	. . .	hour
L	. . .	liter
n	. . .	nano
m	. . .	mili
min	. . .	minute
p	. . .	pico
s	. . .	second
W	. . .	Watt
µ	. . .	micro
λ	. . .	lambda

Glossary

A

Alzheimer's disease: Alzheimer's is a progressive neurodegenerative disorder that primarily affects cognitive functions, leading to memory loss, impaired thinking, and behavioural changes. It is the most common cause of dementia, characterized by the accumulation of abnormal protein deposits, including amyloid plaques and tau tangles, in the brain. As the disease advances, it disrupts communication between neurons, causing their damage and eventual death. This results in the decline of cognitive abilities, affecting memory, reasoning, and daily activities. The exact cause of Alzheimer's is not fully understood, but it is believed to involve a complex interplay of genetic, environmental, and lifestyle factors. Presently, there is no cure for Alzheimer's, and available treatments aim to manage symptoms and slow the progression of the disease.

Amyloid-β: A peptide, often associated with Alzheimer's disease, formed from the amyloid precursor protein. It is known for its propensity to aggregate and form plaques in the brain.

Amyloid precursor protein (APP): A transmembrane protein involved in the synapse formation in healthy neurons. During neurodegenerative disorders, it is involved in the formation of amyloid beta. It is implicated in the pathogenesis of Alzheimer's disease.

Amyloid plaques: Amyloid plaques are abnormal accumulations of amyloid beta proteins that form insoluble deposits in the spaces between nerve cells in the brain. The presence of these plaques is associated with the progressive decline of cognitive functions and memory in affected individuals.

Antibody: A specialized protein produced by the immune system that identifies and neutralizes foreign objects. In research, antibodies are intentionally produced in animals to act as specific markers for targets of interest. They can also be labelled with fluorescent tags for visualization using specific microscopes.

Adenosine triphosphate (ATP): ATP is a nucleoside triphosphate and a fundamental energy carrier in cells. Comprising an adenine base, a ribose sugar, and three phosphate groups, ATP stores and releases energy within its high-energy phosphate bonds. This energy currency is vital for numerous cellular processes, including metabolism, enzymatic reactions, and cellular transport. Upon hydrolysis of its terminal phosphate, ATP releases energy necessary for various biological activities.

Apoptosis: Programmed cell death characterized by specific cellular changes such as cell rounding and condensation, followed by the controlled self-destruction of cells. This

process maintains tissue health by removing unwanted or damaged cells without causing inflammation. Apoptosis is vital for normal development, immune response, and the elimination of unhealthy or mutated cells. Dysregulation of apoptosis can contribute to diseases like cancer and neurodegenerative conditions.

Arborisation: The intricate branching pattern or structure formed by the extensions of neurons, namely axons and dendrites. Neurites, encompassing both axons and dendrites, exhibit arborisation to form complex networks, allowing for extensive connections and communication among nerve cells.

Axons: Long, slender projections of neurons that conduct electrical impulses away from the cell body to other neurons. These fibres facilitate communication between neurons and play a key role in transmitting signals within the nervous system.

B

Binary mask: A binary mask of an image is a representation where the image is converted into a black-and-white format, typically for identifying regions of interest. In this representation, the areas of interest, often identified by specific pixel values or characteristics, are depicted in white (usually assigned a value of 1), while the remaining areas are represented in black (assigned a value of 0).

C

Cell Line: A population of cells derived from a single original cell or a primary tissue sample, which have been adapted to continuous growth in laboratory conditions. These cells are immortalized and can be perpetually cultured under controlled conditions, often retaining specific characteristics or genetic traits from the original cell.

D

Dendrites: Branched projections of nerve cells that receive electrical signals from other neurons. These structures function as receptive sites, collecting and transmitting information towards the cell body of the neuron.

F

Field of view (FOV): The area visible through the microscope under the current settings, determining the extent of the sample or specimen observed within the microscope's view.

H

Hippocampus: A region in the brain responsible for memory formation, learning, and spatial navigation. In Alzheimer's disease, the hippocampus is one of the earliest and most severely affected brain regions. The accumulation of amyloid plaques and tau tangles is believed to lead to damage and shrinkage of the hippocampus, contributing to memory loss and cognitive decline in affected individuals.

I

***In vitro*:** Refers to experiments or studies conducted with cells or biological materials in laboratory dishes or controlled environments outside a living organism. These investigations enable observations and testing of specific cellular or molecular processes in a controlled setting.

***In vivo*:** Refers to experiments or studies conducted within a living organism, such as animals or humans, rather than in a laboratory setting. This involves observing biological processes or testing hypotheses in a living system.

M

Mean square displacement (MSD): MSD is a measure used in particle movement analysis, quantifying the average squared displacement of particles or molecules from their initial position over a specified time interval. Computed by tracking particle positions and averaging squared displacement values, MSD distinguishes between diffusive behaviour resulting from random motion and directed movements influenced by factors such as cellular motor proteins or other active processes. It aids in differentiating between passive diffusion and active transport within biological systems, contributing to the understanding of their distinct behaviours and underlying mechanisms.

Microglia: Microglia are the resident immune cells of the central nervous system, primarily functioning as the first line of defence against pathogens and foreign substances. These cells play a critical role in maintaining the brain's health by monitoring its environment and responding to injury or infection. When activated, microglia can eliminate damaged cells, clear debris, and modulate inflammation. Besides immune functions, they are involved in various neurological processes, contributing to brain development and overall neural health.

Mitochondria: Membrane-bound organelles within eukaryotic cells known for their pivotal role in energy production via cellular respiration. Mitochondria also play crucial roles in cellular signalling, metabolism, and regulating processes related to cell growth and programmed cell death.

N

Nanomaterial: Nanomaterials are substances engineered or naturally occurring at a nanoscale, typically with at least one dimension between 1 and 100 nanometres**.**

Neurites: A general term encompassing the projections extending from the cell body of a neuron, including both axons and dendrites. They are responsible for transmitting and receiving electrical signals within the nervous system.

Neurodegeneration: Un umbrella term that refers to the progressive degeneration or loss of structure and function of neurons in the nervous system. This process, characteristic of various neurological disorders, results in the decline of cognitive function, motor abilities, and other nervous system functions. Common neurodegenerative diseases

include Alzheimer's, Parkinson's, Huntington's, and amyotrophic lateral sclerosis (ALS). Neurodegeneration often involves the accumulation of abnormal proteins, inflammation, oxidative stress, and disrupted cellular processes, leading to the gradual decline and eventual death of neurons, contributing to the symptoms and progression of these conditions.

Neurons: Fundamental units of the nervous system responsible for transmitting information throughout the body. These specialized cells process and transmit electrical and chemical signals via a network of connections, comprising a cell body, dendrites (receiving extensions), and an axon (transmitting extension).

O

Olfactory nerve: The olfactory nerve, also known as cranial nerve I, is responsible for the sense of smell. It transmits sensory information related to odours from the nasal cavity to the olfactory bulb in the brain.

P

Particulate matter PM2.5: PM2.5 refers to fine airborne inhalable particles with diameters smaller than 2.5 micrometres. These particles are small enough to penetrate deep into the respiratory system and can have adverse health effects when inhaled. Long-term exposure to PM2.5 is associated with respiratory, cardiovascular and neurodegenerative issues.

Phagocytosis: Cellular process involving the engulfing and digestion of particles or cells by specialized cells like macrophages. It plays a crucial role in immune responses and tissue maintenance by eliminating pathogens and cellular debris.

Proteome: The proteome encompasses the entire complement of proteins produced or expressed by a cell, tissue, or organism. It represents the entirety of proteins present in a specific biological sample at a given time.

R

Region of interest (ROI): A specific portion within the FOV that encompasses structures or events potentially interesting within the context of the experiment. ROIs are identified for further detailed observation or analysis due to their relevance to the study or experiment.

S

Secondary neuronal death: Secondary neuronal death refers to the subsequent degeneration and loss of neurons that were initially spared from the primary injury or insult. After an initial brain injury, trauma, or a neurological event, secondary neuronal death occurs due to a cascade of events triggered by the primary insult. These secondary processes can include inflammation, excitotoxicity, oxidative stress, and other damaging mechanisms that affect nearby neurons, leading to their degeneration and eventual death, exacerbating the initial injury's impact.

Segmentation: Segmentation refers to the process of partitioning or dividing an image into distinct and meaningful regions or segments. In image processing and computer vision, this technique aims to identify and separate specific objects, areas, or features within an image based on defined criteria, such as colour, texture, intensity, or other visual characteristics. Segmentation is a fundamental step used to extract and isolate regions of interest, enabling further analysis, object recognition, or extraction of pertinent information from the image.

Spheroid: A spheroid refers to a three-dimensional cellular model or culture system composed of aggregated cells grown in a spherical structure, mimicking tissue organization. Spheroids are utilized in scientific research to simulate *in vivo*conditions, allowing for a more biologically relevant context compared to traditional cell cultures.

Sporadic Alzheimer's disease: Alzheimer's disease encompasses various forms, with the most common being sporadic Alzheimer's disease. This type develops randomly, lacking a clear genetic link, and typically affects older individuals. 'Sporadic AD' may be influenced by environmental factors, such as toxins or pollutants, but lacks a definitive known cause. 'Idiopathic Alzheimer's disease' describes cases where the cause is unknown or cannot be identified, often used interchangeably with sporadic AD.

T

Tau: A protein that plays a role in stabilizing microtubules in axons of nerve cells. In neurodegenerative diseases such as Alzheimer's, abnormal tau can form tangles, contributing to neuron damage and cognitive decline.

Tau aggregates:

Intracellular tau tangles: Intracellular tau tangles, also known as neurofibrillary tangles, are abnormal accumulations of twisted tau protein fibres that form within neurons. These tangles, a key feature of neurodegenerative diseases such as Alzheimer's, are correlated with a disruption of the normal structure and function of neurons.

Extracellular tau aggregates: Extracellular tau aggregates refer to abnormal accumulations of aggregated tau protein found outside neurons in the interstitial spaces of the brain or in the cerebrospinal fluid. These deposits of aggregated tau, observed in certain neurodegenerative conditions, are of interest due to their potential role in the transmission of pathology between brain regions, contributing to the progression of the disease.

Transcriptome: The transcriptome comprises the complete set of messenger RNA (mRNA) molecules transcribed from genes within a cell, tissue, or organism at a particular time. It provides insights into the gene expression patterns and activity levels, shedding light on which genes are actively producing mRNA.

Tubulin: A vital protein essential for forming microtubules, crucial components of the cytoskeleton. These microtubules provide structural support, shape, and pathways for intracellular transport within neurons. Tubulin's dynamic nature allows for the assembly and disassembly of microtubules, playing a significant role in neuronal growth, development, and maintaining cellular structure. This protein is integral to neuron

function, contributing to processes like axonal transport, neurite outgrowth, and synaptic plasticity.

W

Wallerian degeneration: Wallerian degeneration is a process involving the breakdown and disintegration of a nerve fibre following an injury or severance. When a nerve fibre is damaged, the portion of the axon distal to the injury site undergoes Wallerian degeneration, characterized by the breakdown of the axon and myelin sheath.

Chapter 1

Material and Methods

1.1 Cell Lines

SH-SY5Y human neuroblastoma (CRL-2266 - ATCC)
HMC3 human microglia (CRL-3304 - ATCC)

1.2 Chemicals

PBS: phosphate buffer saline (Gibco)
100x dcb: 100-times diluted bicarbonate buffer, pH 10, osmolarity 5 miliosmolar, mixed in-house
F-12K: cell culture medium for LA-4 (Gibco)
RPMI 1640: cell culture medium for MH-S (Gibco)
Trypsin (Sigma)
Penicillin-Streptomycin (Sigma)
Non-essential amino acids (Gibco)
BSA: bovine serum albumin (Sigma)
KCl (Kemika)
HCl (Merck)
KOH (Carlo Erba)
DMEM (Sigma-Aldrich, France, Saint-Quentin-Fallavier)
4 mM L-glutamine (SIGMA-G7513)
Triton (Sigma-Aldrich, France, Saint-Quentin-Fallavier)

1.3 Software

Stedycon gallery
Imspector (version 16.2.8282-metadata-win64-BASE), provided by Abberior
Fiji, ImageJ 1.52p (NIH)

1.4 Materials

#1.5H μ -Slide 18-well (Ibidi)
#1.5H μ -Slide 8-well (Ibidi)

1.5 Labels and Labelling Structures

For microscopy, we used fluorescent labels compiled in Table 1. The selection of these labels was careful and based on their suitability for long-term live-cell imaging. We focused on factors such as cell viability, motility, morphology, and the morphology of subcellular organelles. Additionally, we investigated the cell's capability to form nanoquarantines in response to exposure to TiO_2 nanotubes. This cellular response involves actively "burying" the material in lipids, proteins and other biological molecules to diminish the hazardous surface area of particles, limiting their potential interaction with the cells. By doing so we tested cell's ability to retain their various functions after labelling.

The chosen combinations of labels were designed to minimize cross-talk and ensure negligible interference between labels. All live samples were labelled and imaged immediately after exposure to nanomaterial. If not, the procedure was explained where the respective experiment was described.

Table 1: List of fluorescent labels and antibodies used in this thesis with their relevant characteristics.

Fluorophore	*Manufacturer (cat. nr)*	*Excitation peak (nm)*	*Emission peak (nm)*	*Concentration (μM)*
CellTracker™ Green CMFDA (CTG)	Thermo Fisher (#C2925)	492	517	1
ATTO490 LS conjugated to anti-TAU ab	ATTO-TEC	495	658	0.01
CellMask™ Deep Red (CMDR)	Thermo Fisher (#C10046)	650	685	1
Alexa-647 conjugated to anti-Aβ ab	Thermo Fisher (#A20006)	650	665	0.01
MitoTracker™ Green FM	Thermo Fisher (#M7514)	490	516	0.05

Before mixing, we labelled microglia in the suspension with the CellTracker Orange (CTO, Thermo Fisher, cat. nr. C34551) to stain their cytoplasm. Microglia were incubated for 45 minutes with approximately 1-5 µM concertation of the label. Thereafter they were washed 3 times with PBS and centrifugated (2 x 500 rpm for 5 min) to remove all of the surplus label in the media, and added to neurons. After mixing, co-culture was labelled with the CMDR.

If other labels were used, they will be mentioned with the respective experiment.

1.6 Nanoparticles

Table 2: Selection of nanomaterial used in the thesis with their physical characteristics and final dispersion concentration.

Material	*Mass (mg)*	*Volume (mL)*	*Size (DxL) (nm)*	*BET (m^2 g^{-1})*	*Final concentration (mg mL^{-1})*
TiO_2 nanotubes	1.0	1.6	10 x 100	150	0.65
TiO_2 nanocubes	1.0	1.0	15 x 20	97	1.00
MWCNT 401	1.0	1.4	67 x 4000	140	0.71

1.7 Preparation of Nanoparticles

The synthesis of TiO2 nanotubes and nanocubes followed a rigorous procedure and has been extensively documented. In brief for nanotubes, the process began with the controlled hydrothermal synthesis of sodium titanate nanotubes. These sodium titanate nanotubes were subsequently subjected to ion exchange to transform them into hydrogen titanate nanotubes. Finally, through a carefully conducted thermal treatment, the hydrogen titanate nanotubes were successfully converted into the desired TiO2 nanotubes. The detailed methodology and experimental conditions can be found in the comprehensive study by Umek et al. [1].

Multi-walled carbon nanotubes (MWCNT; NM-401) were a kind gift from the Joint Research Centre (JRC).

We employed a dispersion technique using cup horn sonication to disperse materials from Table 2 in a buffer. The buffer solution utilized in this study was 1 mM bicarbonate buffer with a pH of 10, which was specifically chosen due to its low osmolarity and high pH properties that minimize the charge screening of the active surface of the materials.

To ensure uniform dispersion of the materials in the bicarbonate buffer, the materials were resuspended so that each 3 µL of the dispersion contained 3 cm2 of the material surface. The weighted mass of each material and the volumes of bicarbonate buffer utilized to prepare the solutions are presented in Table 2.

1.8 Cell Lines, Sample Preparation and Exposure

Human neuroblastoma cell line SH-SY5Y commercially available from the American Type Culture Collection (ATCC, www.atcc.org or www.lgcstandardsatcc.org, catalogue number CRL-2266™) grew as a mixture of floating and adherent cells in DMEM/F-12 (Gibco) medium supplemented with 1% penicillin/streptomycin (Sigma-Aldrich), 2 mM GlutaMax (Gibco), and 10 % FBS (BioChrom AG). For SH-SY5Y differentiation into neurons, we seeded 2 x 10^4 cells cm^{-2} on the collagen-coated microscopy-adapted plates (8-wells or 18-wells; Ibidi). After 24 hours we added the differentiation medium containing Dulbecco's modified eagle medium DMEM/F12 without phenol red (#21041025, Thermo Fisher), supplemented with 1% P/S (Sigma-Aldrich), 2 mM GlutaMax (Gibco), 0,5 % FBS (BioChrom AG) and 10 uM retinoic acid (fisher scientific, #AC207341000). Old media was replaced with 100 µL fresh differentiation media every other day, until 7th day when we terminated the differentiation.

HMC3 is a human brain microglia cell line commercially available from the American Type Culture Collection (ATCC, www.atcc.org or www.lgcstandardsatcc.org, catalogue number CRL- 3304™), cultured in DMEM (Gibco), supplemented with 100 U/M penicillin, 100 µg ml^{-1} streptomycin (Sigma-Aldrich), 2 mM GlutaMax (Gibco), and 10 % FBS (Gibco). Microglia were seeded at 7 x 103 cells cm^{-2}, or as necessary to reach a certain ratio with respect to neurons, on the microscopy-adapted glass bottom plates (8-wells or 18-wells; Ibidi).

Where the co-culture of these cells was used, we mixed neurons and microglia in the ratio of 5:1 (neurons: microglia; or different if specifically mentioned) using the 10:1 mixture of neuronal media to microglia media, lest we risk de-differentiation of neurons due to a too high FBS fraction. We added microglia to neurons on the 6th day of differentiation.

1.9 Imaging

For long-term live-cell imaging, we used a state-of-the-art imaging system consisting of a Microscope Stage Top Chamber (Okolab H301-MIN) incubator mounted on the Olympus (Olympus IX83) confocal fluorescent microscope, equipped with the STED laser (Stedycon, Abberior). Stage top incubator maintains atmosphere with the 37°C, 5% CO2, and >95% humidity to enable long-term imaging of living cells.

The microscope was equipped with either a 20x magnification objective and 0.8 numerical aperture (NA) lens or a 60x magnification objective with a 1.2 NA lens. System incorporates four pulsed laser sources (Abberior) with a pulse duration of 120 ps and a maximum power of 50 µW at the sample plane. Additionally, four avalanche photodiode detectors (APD) were utilized for signal detection. Table 3 provides the most frequently used combinations of lasers and filters employed during the experiments. The STED depletion laser, operating at a wavelength of 775 nm, had a pulse duration of 1.2 ns, and a maximum power of 170 mW at the sample plane. In cases where were we adjusted the microscope settings for maximal resolution during specific experiments, we described these alongside the corresponding images later in the text.

Table 3: Stedycon laser-detector combinations.

Laser $\lambda_{EXCITATION}$ *(nm)*	*Laser* $\lambda_{EMISSION}$ *(nm)*
488	485-495
488	505-550
561	575-625
488	650-700
647	650-700

Nanoparticles were detected in the label-free, backscatter detection mode, utilizing the 488 / 488 ± 5 nm excitation / detection combination. Due to the large coherence of the laser, the backscattered light exhibited a strong speckle pattern, which was removed by Fourier transform bandpass filter (1 – 500 pixels) on scattering images. These images were subsequently binarized to obtain nanomaterial masks.

1.10 Image Analysis

To track the motion of nanoparticles and mitochondria on individual images or a smaller number of images we have used Fiji's (ImageJ) Manual tracking plug-in.

For the analysis of long-term time-lapse experiments, we utilized algorithms developed in-house and implemented using Python. The detailed explanation of each algorithm's concept will be provided within the context of the specific experiment where it was applied.

To get further insights into the analysis and algorithms, we welcome you to reach out to us directly at the Laboratory of Biophysics, Condensed Matter Physics Department F5, Jožef Stefan Institute, Ljubljana

Chapter 2

Introduction

2.1 Alzheimer's Disease and the Lack of Early Diagnosis

Dementia is a general term encompassing a wide range of medical conditions resulting in a loss of memory and other cognitive abilities [2], [3]. It is caused by the neurodegeneration or, more specifically, damage to the brain cells and shrinkage of brain tissue in different regions of the brain. For example, the most common neurodegenerative disease qualifying as dementia is Alzheimer's disease (AD), where memory loss is one of the earliest symptoms, and the brain cells in the region responsible for learning and memory, called the hippocampus, are the first to be damaged [4]. Given its prevalence, AD accounts for over 80% of dementia cases [5], making it the central focus of our study.

Traditionally, AD diagnosis is established according to the genetic predispositions and manifested symptoms, with growing support from brain imaging, cerebrospinal fluid, and blood biomarkers to pinpoint disease type and progression stage [6], [7]. However, such methods are ineffective in identifying AD prior to symptom manifestation, particularly in sporadic cases of disease. Consequently, by the time of diagnosis, extensive brain region atrophy, primarily characterized by axonal degeneration and widespread neuron loss, has already occurred [8]. This progressive atrophy manifests as shrinking brain volume and a gradual decline in cognitive function, often leading to complete dependence on caregivers for daily activities. Following diagnosis, an expected survival of AD patients ranges between 3 to 8 years [9], making it the 7th most often cause of death in the world [10].

2.2 Alzheimer's Disease Hallmarks Recognized, Yet Causally Elusive, as Evidenced by Treatment Failures

Despite more than half a century of research, the causes of neurodegeneration, including AD, still remain unknown and no effective treatment yet exists [4]. During this period, a substantial portion of research efforts has been dedicated to unravelling the properties of amyloid-β (Aβ) and tau, fibrillation-prone proteins with a tendency to oligomerize and aggregate, giving rise to distinctive extracellular structures known as Aβ plaques. The presence of these plaques correlates positively with the severity of the disease's outcomes [11], [12], thus rendering them as primary subjects of intense research within the context of AD.

2.2.1 Reconsidering the amyloid cascade hypothesis: a twenty-year stalemate

Initially, Aβ protein, constituting up to 80% of Aβ plaques, was deemed an aberrant protein implicated in AD initiation [12]. However, subsequent insights revealed Aβ's role as a crucial membrane protein involved in processes like synaptogenesis, axon arborisation, and synaptic plasticity [13], [14]. It is normally present in axons as the amyloid precursor protein (APP), where it, among other roles, acts as a synaptic contact protein for other neurons and microglia [14], [15]. On the other hand, upon cleavage from the membrane, a fragment known as Aβ peptide—prone to aggregation—gets secreted and deposits within Aβ plaques.

The amyloid cascade hypothesis emerged, proposing Aβ plaques as a central player in AD pathology, prompting extensive research to comprehend and counter the disease [16]. It was soon discovered that the damage to synapses and neuronal network [17][18] – events central to AD [19] – appeared in the proximity of the extracellular Aβ plaques, inviting further scrutiny. Furthermore, Aβ plaque-laden brains in human patients and transgenic mice showed an increased number of microglia with elevated expression of pro-inflammatory markers, a unique response not caused by other proteins [20].

With mounting evidence of Aβ plaque toxicity, researchers vigorously sought compounds to hinder plaque formation and mitigate disease progression. Contrary to all expectations, pharmacological interventions targeting Aβ plaques failed to slow, stop, or reverse the disease development [4]. This lack of success, further encouraged with the important study by Lambert et al. published in 1998, caused a pivotal shift of focus from insoluble Aβ plaques to soluble Aβ oligomers, which showed even greater correlation with the adverse outcome of the disease [14]. The study revealed that the soluble Aβ oligomers were responsible for dendritic spine loss and impaired synaptic signalling [21], with the prevalence of these events in the proximity of plaques [22].

Novel therapeutic avenues emerged, targeting downstream enzymes β or γ secretase to preclude APP cleavage, and consequently, soluble Aβ oligomer accumulation. Yet, the severe side effects of these compounds rendered them unusable, and no effective therapeutics were discovered [23]. Alternative strategies aimed to targeted existing Aβ plaques in the brain using the monoclonal antibodies as opsonin or by inducing the immune system microglia to clear the protein. This approach aimed to enhance microglia natural propensity to clear Aβ oligomers and small plaques [24], [22], and while it showed promise in animal studies, none of the potential drugs from this group improved cognitive decline of AD patients [6].

While elevated levels of soluble and aggregated Aβ peptides negatively correlate with the AD outcome, their exact mechanisms of toxicity remain unclear. Combined with their propensity to form up to two decades before symptom onset [4], [18], [25], understanding their role in sporadic AD pathogenesis proves challenging. The lack of mechanistical understanding of Aβ toxicity, coupled with over 400 failed treatment trials in last 20 years [26] and postmortem studies revealing individuals can live with substantial Aβ plaque burdens without cognitive impairments [27], raised doubts about the Aβ peptide being the

main culprit in the AD pathology [28]. Nevertheless, the importance of Aβ in AD pathogenesis still persists, as it acts as a seed for the accumulation of tau protein. Their interaction results in the formation of large aggregates containing both Aβ and tau, a phenomenon exclusively observed in patients that exhibit AD symptoms, including cognitive decline [22], [29].

2.2.2 Tau protein aggregates thought to play an important role in AD but treatments fail

Tau protein is a tubulin-associated protein involved in its stabilization within axons. Aberrant changes of tau protein appear early in the onset of neurodegeneration while the aggregates, deemed crucial for the development of extensive neurodegeneration, form years later [4], [20].

Hyperphosphorylation-induced post-translational modifications disrupt tau protein stability, prompting its detachment from tubulin and subsequent migration within axons and soma. Given its early implication in neurodegeneration, substantial efforts have focused on modifying enzymes engaged in tau protein phosphorylation, resulting in over 20 compounds undergoing clinical trials since 2004 [29]. While several have effectively reduced tau protein phosphorylation *in vitro* and *in vivo*, breakthroughs in AD patient trials have remained elusive [29]. A lone exception emerges in a small clinical study involving lithium chloride, which displayed marginal cognitive decline reduction in patients [30]. Although the precise mechanism of action of lithium remains unclear, recent research suggests its potential to modulate macrophage-mediated inflammation [31], indirectly linking neurodegeneration to inflammatory processes.

Dissociation of tau protein from microtubules increases its cytoplasmic levels, consequently multiplying the potential of tau-tau interactions and promoting aggregation. Neurons laden with tau aggregates show a reduced number of synapses [20], [32] and impaired axonal trafficking of organelles, which is believed to result in metabolic imbalances across the neural network leading to neuronal dysfunction and death [33]. Despite promising outcomes in animal models, the majority of tested compounds targeting these aggregates have failed to manifest significant improvements in cognitive decline during later-stage clinical trials [29].

2.3 Reassessing Alzheimer's Disease Treatment Trials: Do Our Disease Models Hold the Answer?

Taken together, pharmaceutical trials of potential drugs against Aβ and tau, the primary therapeutical focus for AD, have yielded negative results [34], [35], [36] culminating in a staggering 99.6% failure rate [37]. On the other side, the pursuit for Aβ and tau alternatives is not mature enough to open new avenues for new prospective therapeutics, resulting in a roster of 143 agents in the AD drug development pipeline for 2022, covering a broad array of mechanisms of action [6]. A wide variety of these compounds, including

caffeine and nicotine, do not convey the confidence of directed research, but rather appear like a desperate screening for potential candidates on the largest scale.

Consequently, the pharmaceutical industry, a pivotal force in drug discovery, is increasingly halting investments in novel AD therapies, due to the formidable failure rates, exorbitant expenses, and prolonged development timelines [38]. This caused a great concern in scientific community, prompting experts into expressing the urgent need for disease models with greater predictive power [39].

Current AD research and development predominantly rely on genetically engineered models "programmed" to emulate one or more molecular hallmarks of the disease. Yet, a stark contrast arises: while over 99% of real-world AD cases emerge from environmental rather than genetic origins, our prevailing models predominantly mimic the latter [40].

2.4 Could Particulate Matter Hold the Clue to Transitioning Alzheimer's Disease Models from Genetic to Environmental Causes?

Mounting epidemiological evidence suggests a strong correlation between cognitive decline and exposure to ambient concentrations of fine particulate matter smaller than 2.5 µm (PM2.5) – a revelation that implicates air pollution as a potential contributor to AD pathogenesis [7], [41], [42]. Disturbingly, approximately 60% of dementia cases occur in developing countries [43], where the air PM2.5 levels are generally suboptimal [44]. Moreover, epidemiological insights suggest a direct correlation: higher PM2.5 exposure appears to correlate with accelerated cognitive decline [45].

Beside the epidemiological data, several studies have found traces ambient PM2.5 within Aβ plaques, hinting at a possible connection between airborne PM2.5 and AD pathology. Post-mortem examinations of brain biopsies from young individuals residing in densely polluted urban locales have revealed the presence of Aβ plaques and tau neurofibrillary tangles [40], [41], [46]. In another study, imaging of a thin section of Aβ-plaque cores, obtained from the autopsy of AD patients for neuropathological examination, uncovered the presence of ambient magnetite nanoparticles within Aβ plaques [47].

However, while the data emphasizes the potency of PM2.5 as a potential trigger, the precise link between airborne particles and neurodegeneration remains a topic of fervent debate. The cause of this controversy resides largely in the lack of conclusive experimental findings that unequivocally link inhaled PM2.5 to brain translocation. The question of whether inhaled nanoparticles can even reach the brain remains a topic of intense debates.

The presumed routes of inhaled particle migration comprise traversal through the blood-brain barrier or translocation along the olfactory nerve. Both pathways begin with the inhalation of airborne particles, whereafter mucus and ciliary protrusions of cells in the upper respiratory region trap the majority of inhaled particles. Only PM2.5 and smaller particles, including nanoparticles with at least one dimension under 100 nm, can evade these defence mechanisms, eventually reaching the alveoli of the lower respiratory tract. In

the ensuing weeks, majority of these nanoparticles are dissolved or excreted from the body via various mechanisms [48], while a subset remain and become sequestered [49]. Some of these nanoparticles can relocate from the alveoli to the bloodstream [50]. However, due to the minute volume of translocated nanoparticles and the large volume of blood, the accumulation of these nanoparticles at the blood-brain barrier in quantities needed for pathological changes would require countless years of inhaling air polluted with 40 µg m-3 PM2.5 [46], making the first hypothesis less plausible.

On the contrary, the second pathway, involving nanoparticle translocation along the olfactory nerve, emerges as a more plausible route, because the distance between the brain and nasal mucosa is only a few centimetres. Furthermore, axons of olfactory neurons extend to the nasal mucosa on one end, and synapse with regions intrinsically related to neurodegeneration, including the hippocampus, hypothalamus, and prefrontal cortex [51], on the other. Curiously, while this very relationship has been harnessed in the realm of drug nanocarrier development, wherein inhaled therapeutic agents are delivered directly to the brain [52], it remains a topic of heated debates in the field of neurotoxicology.

2.5 Formulating Hypotheses for a Novel Sporadic Alzheimer's Disease Model

In summary, existing *in vivo*and *in vitro* models of AD fall short in predicting disease progression and therapeutic effectiveness. Nonetheless, there is consensus that an effective predictive model of neurodegeneration should possess the capacity to:

- Replicate established neurodegeneration hallmarks, including Aβ plaque formation, tau deposition in plaques, axonal atrophy, immune system activation, and neuronal loss,
- Track molecular/cellular events in living neurons and brain immune cells, such as microglia,
- Trigger AD through exposure to environmental factors, like PM2.5

The emergence of Aβ plaques, tau deposits, axonal atrophy, and inflammation leading to neuronal loss are later-stage developments in AD etiology, akin to symptomatic manifestations of an already advanced disease. This may account for the repeated therapeutic failures targeting these advanced events. While in the best-case scenario, such interventions might decelerate disease progression, decades of failed clinical trials underscore a different reality, suggesting that the potential answer lies in events earlier along the timeline.

To effectively cure or prevent a disease, a comprehensive understanding of its triggers is imperative, coupled with the capability to experimentally reproduce the disease within a controlled laboratory environment. If we can systematically induce the disease under controlled conditions, armed with the knowledge of the subsequent key molecular/cellular events and their causal relationships, we can quantitatively evaluate its progress and gain the possibility to modulate it.

To address these gaps, **this dissertation defines the following hypotheses**:

1. Some nanoparticles, present in ambient air, can be transported along neuronal axons, representing the basis for long-distance particulate matter relocation from the nose to the brain.
2. In a non-genetically AD predisposed *in vitro* co-culture of neurons and microglia, exposure to some nanoparticle can induce AD and reproduce all the known hallmarks of neurodegeneration, including amyloid-β plaques, tau deposits in plaques, axonal atrophy, and neuronal death. Microglia might exert local influences, potentially preventing, delaying or diminishing hallmarks of neurodegeneration.
3. Non-genetically modified neurons that reproduce AD hallmark events have the capacity to unveil early molecular/cellular events that lead to the occurrence of these late-stage pathological changes.

Chapter 3

Results and Discussion – Translocation of Particles from the Nose to the Brain

The opening chapter of this dissertation explores the transport mechanism of three distinct nanoparticles along axons of differentiated human SH-SY5Y cell line-derived neurons. The nanoparticles under scrutiny include inflammatory TiO_2 nanotubes, non-inflammatory TiO_2 nanocubes with identical chemistry but lacking the capacity to induce inflammation, and inflammatory multi-walled carbon nanotubes (MWCNT) characterized by distinct chemical and physical properties compared to the first two. Employing advanced long-term live imaging techniques and analysis, we propose that certain nanomaterials, notably TiO_2 nanotubes, can undergo long-range transport facilitated by an active, motor-protein-driven process akin to cellular organelle movement. Furthermore, we validate this transport phenomenon within a 3D neuronal spheroid, emphasizing its preservation in more complex environments. Taken together, our results hint at the potential mechanism of axonal transport of these nanoparticles, thus giving a plausible explanation for their potential migration from the nasal mucosa to the brain via the olfactory nerves.

3.1 Axonal Transport

We begin this study with the investigation of the potential transport mechanism of TiO_2 nanotubes, established inflammatory nanoparticles [49], along axons of human neurons *in vitro*. To achieve this, we have devised a simple *in vitro* model comprising differentiated neurons capable of forming long axons. While we acknowledge the structural simplicity of this model compared to real tissue, we are also keenly aware of its inherent strengths. Namely, the ability to replicate a long-distance particle translocation along axons rich in motor proteins.

The neurons of the human olfactory system are naturally interconnected throughout the entire length of the structure, facilitating the successful relay of olfactory information from the environment to the brain. Similarly, our *in vitro* neurons extend long axons, establish connections with other neurons and are capable of long-distance transport of macromolecules and organelles, indicative of numerous motor proteins in their axons.

Consequently, our *in vitro* model, despite its simplicity, conserves crucial functional traits observed in living animals, essential for exploring the axonal transport of particulate matter.

By employing a time-lapsed confocal imaging of neurons labelled with the plasma membrane label CellMask Orange (CMO) and exposed to TiO_2 nanotubes (red), we observed the motion of nanotubes along the length of the axons (green) (Figure 1A-B, Movie M1A and M1B). Notably, this motion was distinctly unidirectional (Figure 1D) and steady, as indicated by the almost constant maximal speed at all lag times in Figure 1F, initiating at the one end of the axon and terminating at the opposite. Such directed transport in cells is normally achieved via the interplay between the tubulin and associated motor proteins from the kinesin and dynein superfamilies [53].

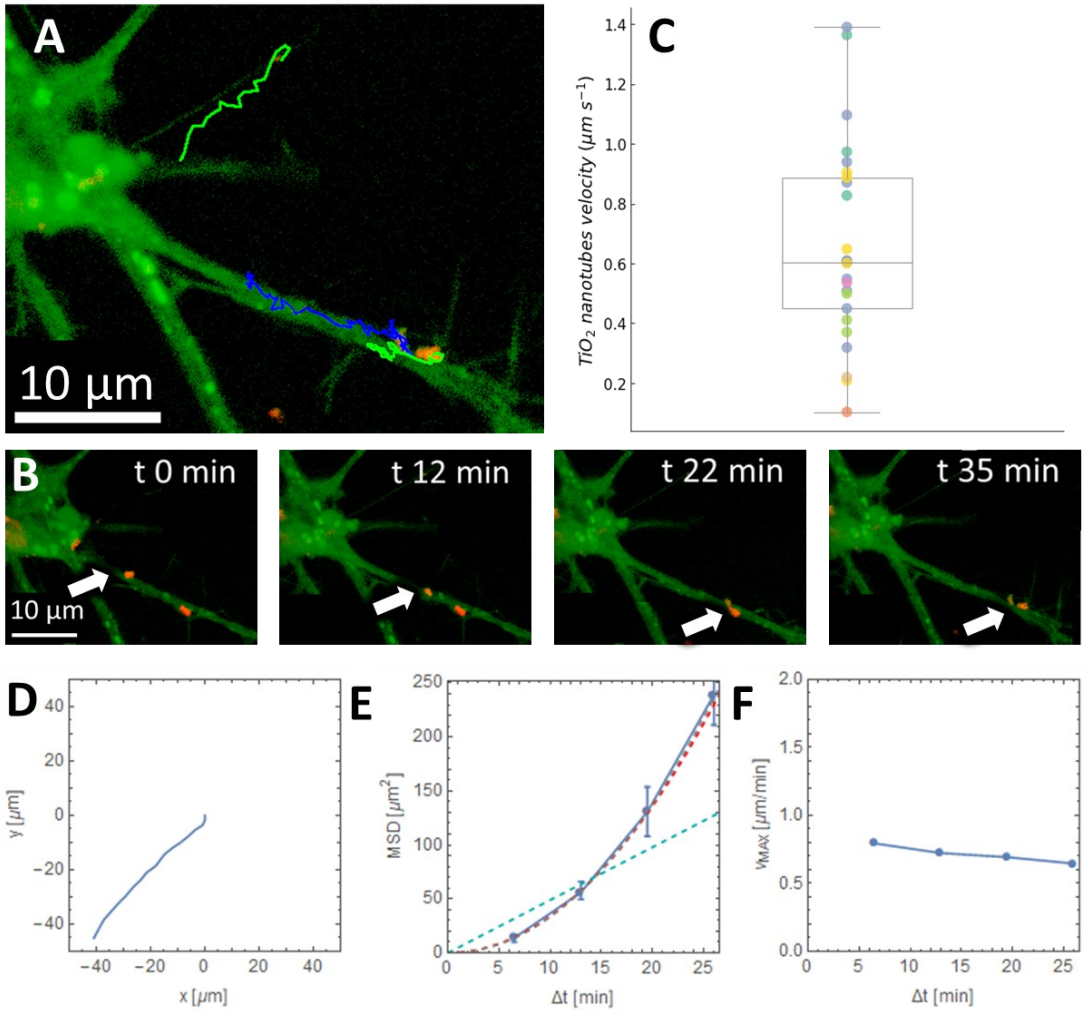

Figure 1: **Confocal timelapse of axonal transport of TiO_2 nanotubes**. A) Coloured tracks represent trajectories of Alexa647-labelled TiO_2 nanotubes (red) traversing axons of a neuron labelled with the plasma membrane CellMask Orange fluorescent label (green); B) selected frames extracted from a time lapse at 0, 12, 22, and 35 minutes. White arrows trace the displacement of TiO_2 nanotube composite along the axon; C) distribution of

average velocities (µm min^{-1}) derived from multiple axonal transport experiments (different colours) involving TiO2 nanotubes; D) x and y coordinates of a typical TiO_2 nanotube track depicting its directed motion; E) a full blue line represents the fitted MSD curve obtained through the analysis of TiO_2 nanotube trajectories. Potential MSD curve fit overlaps almost perfectly with the model of directed, linear motion (dashed red line) and not diffusion (dashed blue line); F) a maximal velocity of moving TiO_2 nanotubes (µm min^{-1}) measured at 5-minute time-lag intervals during axonal transport.

To investigate if these motor proteins drive observed motion of TiO_2 nanotubes within living cells presents various challenges that could impede direct observation. Traditional intracellular labelling methods using antibodies, for instance, are incompatible with live-cell experiments due to the need for cell membrane perforation. Furthermore, introducing the physical bulk of antibodies to motor proteins inside the cell can alter or hinder their normal functioning. Another typical approach is through a genetic engineering, involving time-consuming methods that are not easily accessible in most laboratories. Given these limitations, we opted for analysis of different motional descriptors, such as the mean square displacement (MSD) and velocity, as a powerful tool to study the mode of axonal transport of TiO_2 nanotubes within the living neuronal culture.

The analysis of TiO_2 nanotube trajectories along axons gave indications that their motion is indeed an actively driven process rather than a diffusion. In case of diffusion, the MSD exhibit a linear increase with time, while in case of a motor-assisted motion, the MSD increases quadratically with time, which is clearly seen in Figure 1E (full blue line). Moreover, the calculated mean motion velocity of 0.6 µm min^{-1} (Figure 1C) closely resembles that of cellular organelle transport, a process known to rely on motor proteins [54]. This consistency further indicates that the observed motion of TiO_2 nanotubes could be associated with an integral part of the intracellular transport machinery.

An intriguing parallel occurs with the way in which viruses exploit motor-protein machinery for transport. Namely, they attach to heparan sulphate at the cell surface, which is connected to various transmembrane proteins that interact with motor proteins within the cell [55], [56]. Consequently, cell's own transport machinery moves viruses around. An indication of similar interaction between the TiO_2 nanotubes and the cell's transport complexes comes from the enrichment in actin, tubulin, kinesin, and dynein components in the coronome (corona proteome) of the same TiO_2 nanotubes following the exposure to lung epithelial cells. For that reason, we propose that active axonal transport of TiO_2 nanotubes may be a consequence of a similar process observed in the transport of viruses. The surface of TiO_2 nanotubes exhibits a high affinity for phosphates and amides, abundant in plasma membranes, leading to rapid coordinate bonding with these molecules [49]. Therefore, binding of TiO_2 nanotubes to any phosphate- or amide-rich membrane structure that is connected to motor proteins could facilitate their translocation along the cell surface.

The important distinction lies in the fact that viruses eventually get taken up by cells, while TiO_2 nanotubes must reach the brain without getting trapped within neurons or multiple barriers encountered along the way. Understanding the mechanisms that enable their uninterrupted transport from neuron-to-neuron is a crucial next step in unravelling their full path to the brain.

3.2 Transport of Particles Across the Neuronal Network

The plausible answer comes from a 30-hour long time-lapse observation of neurons exposed to non-labelled TiO_2 nanotubes. Already within 30 minutes of exposure, TiO_2 nanotubes were aggregated and co-localized with lipids and other biological material on neuronal bodies and axons (Figure S2), akin to the process of nanoquarantining that occurs in the lungs during the exposure to the same material [49]. Unlike the stationary nanoquarantines seen in lung epithelial cells, axons of neighbouring neurons detached and moved these structures within the first 3 hours (Movie M2). The interaction is visually depicted in the series of time-shot sections in Figure 2C, indicated with arrows.

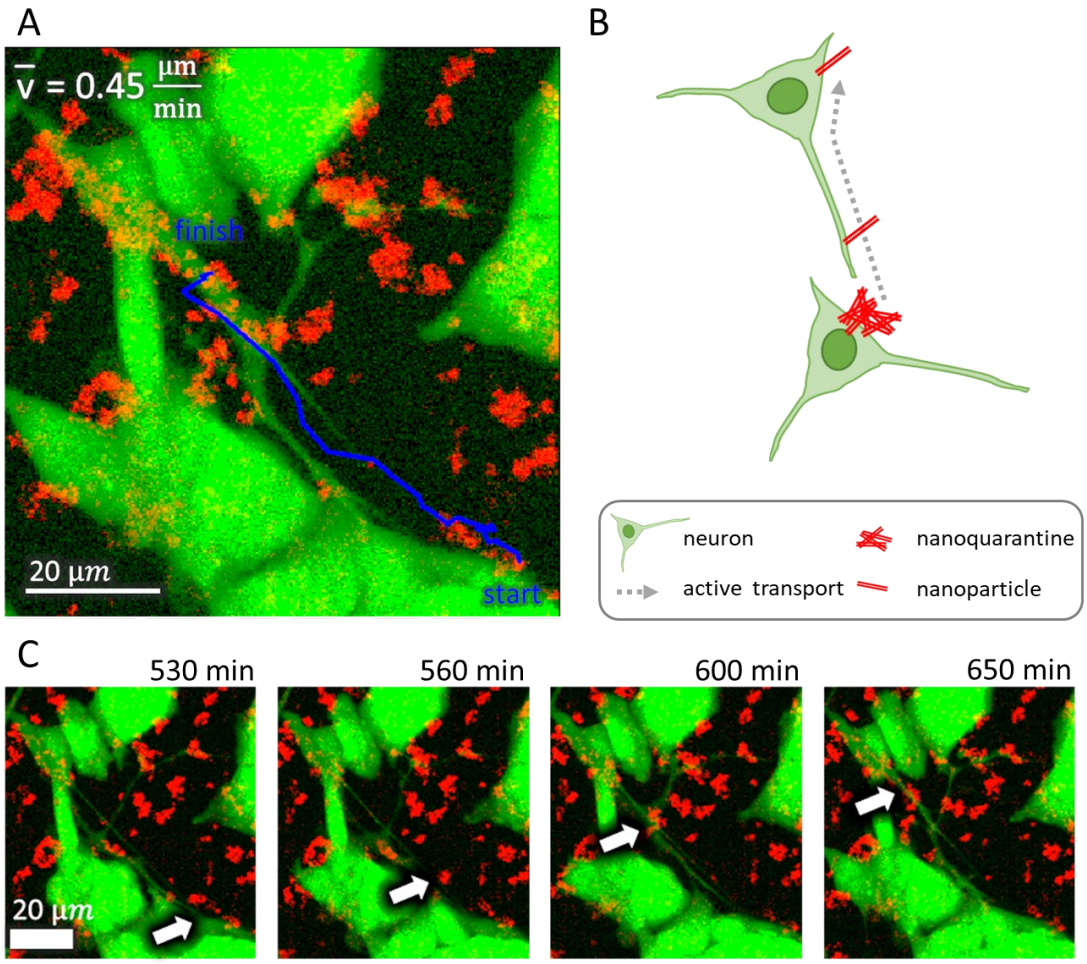

Figure 2: **Relocation of TiO_2 nanotube aggregates between two distinct neurons facilitates the long-distance transport (log transformed).** A) The "finish" neuron's axon (green) disassembles the TiO_2 nanotube aggregate (red) from the "start" neuron and actively transports aggregate's fractions along its own axon. This unique phenomenon facilitates TiO_2 nanotubes motion between neurons. B) A simplified cartoon illustrates a process derived from the micrograph on the left, showcasing the trajectory of a nanoparticle (red), starting from the lower neuron and transporting along the axon of the upper neuron. C) Representative time-lapse frames from the 120-minute interval depict the translocation

of a TiO_2 nanotube aggregate covering approximately 60 µm. The transport trajectory (shown in blue) indicates an average velocity of 0.45 µm min^{-1}. This velocity can be extrapolated to 10^4 minutes for a distance of 5 cm, suggesting a timeframe of 2-3 months for inhaled particles to reach the brain

To determine if the transport features observed for TiO_2 nanotubes apply to other particles, we examined two other nanomaterials: non-inflammatory TiO_2 nanocubes [49] and multi-walled carbon nanotubes (MWCNT), associated with various pleural chronic complications [57], [58] after inhalation. While TiO_2 nanocubes share the same chemistry as TiO2 nanotubes, they have a different shape and surface. MWCNT, on the other hand, exhibit distinct chemical compositions and physical properties, including uptake rates and mechanisms.

In these time sections, an axon of a neuron situated approximately 50 µm away from the initial position of the TiO_2 nanoquarantine made a direct contact with the nanoquarantine, leading to its fragmentation to smaller units. Subsequently, these fragments were transported further along the axon to the body of distant neuron. One such fragment's trajectory is represented in blue colour in Figure 2, clearly indicating the passage of TiO_2 nanotubes between two neurons (start and stop positions). If this process were continuously repeated, it could facilitate the transport of nanotubes across the neuronal network, allowing them to reach distant locations, theoretically enabling their passage to remote locales, such as the hippocampus in the brain.

The experiment was conducted in a similar fashion as with the TiO_2 nanotubes. We exposed neurons to these materials and conducted a 3D time-lapse acquisition, to facilitate identification of nanoparticles within neurons. In addition to the MSD analysis of obtained nanomaterial trajectories, we performed an analysis of acquired micrographs that included nanomaterial and cell segmentation at each time-point of the time-lapse. This allowed us to quantify the amount of material present in cells and in nanoquarantines. All nanomaterial-related objects that were larger than 3 µm in diameter, were classified as nanoquarantines, and the cumulative scattering intensity within these objects was normalized and plotted in Figure 3D. A similar algorithm was applied for the nanoparticles located within cells (Figure 3E), except these values were normalized to the cumulative scattering intensity of all nanomaterial in that respective field of view (FOV) and we omitted the size threshold 3 µm, because we wanted to quantify the amount of nanomaterial taken up by the cell, regardless of it being in the form of single particles or aggregates.

The results revealed contrasting transport behaviour of MWCNT compared to TiO_2 nanotubes and nanocubes. Unlike these two materials, MWCNT were not actively transported, as suggested by a linear increase in MSD with lag time, indicative of diffusive motion (Figure 3F; Movies MS118, MS119). They were also not quarantined (Figure 3D, blue line) nor were they taken up by neurons (Figure 3C and E, blue line), as can be told from the lack of the yellow colour, indicative of co-localization of green (membrane) and red (nanomaterial). This can probably be attributed to their large aspect ratio resulting from their considerable length, making their uptake difficult, even for professional phagocytes, leading to frustrated phagocytosis [59].

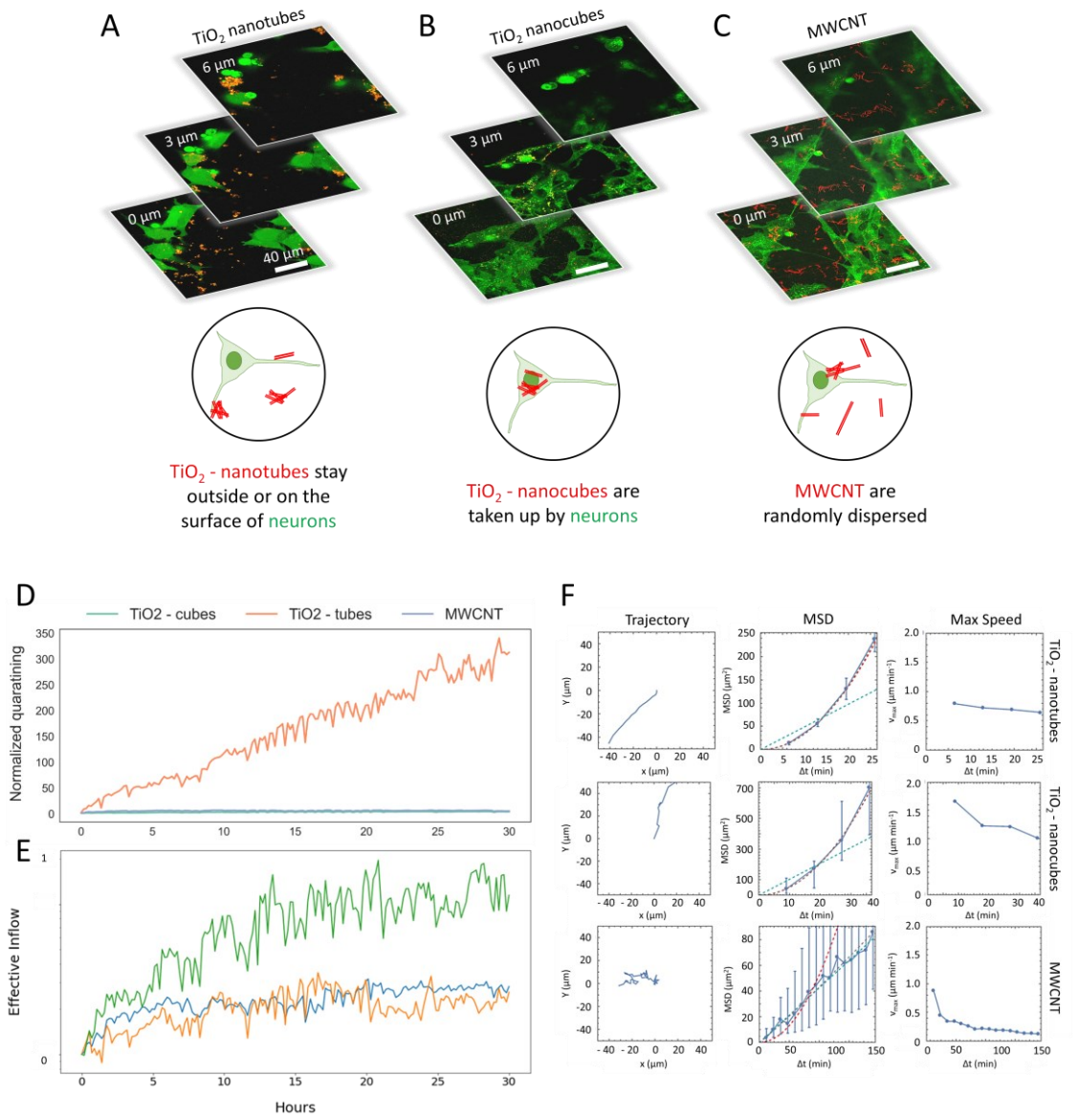

Figure 3: **Long-distance transport requires active transportation of nanomaterials rather than uptake by neurons**. A-C) Three z-sections at 0, 3, and 6 µm height of neurons labelled with the plasma membrane label CellMaks Deep Red (green) exposed to a 10:1 dose of non-labelled A) TiO_2 nanotubes (red), localized mostly outside on the neuron surface; B) TiO2 nanocubes, showing significant uptake as indicated by the yellow signal (red and green co-localization) within neurons; C) MWCNT that are randomly dispersed across the field of view without obvious co-localization with membrane structures (no yellow colour); D) TiO_2 nanotubes, TiO_2 nanocubes and MWCNT scattering intensity was filtered and binarized. Scattering intensity integral within objects larger than 3 µm in diameter (nanoquarantining) was plotted with orange, green and blue lines, respectively. Each dataset was normalized to its first value; D) effective inflow represents the fraction of material that has been taken up by cells; E) trajectories, mean square displacement (MSD), and maximal velocities of TiO_2 nanotubes, TiO_2 nanocubes, and MWCNT obtained from the analysis of particle trajectories.

In contrast, we observed that TiO_2 nanocubes were actively transported along axons, as indicated by the potential fit of MSD curve in Figure 3F. Moreover, the average speed of their motion was very similar to that of TiO2 nanotubes (Figure S1F). However, TiO_2 nanocubes did not form large nanoquarantines (Figure 3D, green line). This lack of nanoquarantining likely enabled neurons to take up the majority of small nanocubes, resulting in their intracellular localization (yellow objects – green and red co-localisation – within neurons in Figure 3B). The amount of nanocubes taken up by neurons was quantified and plotted in Figure 3E, showing a steadily rising green line over time that plateaued only after 15 hours. We suggest that, as a consequence of this uptake, their transport beyond the initial neuron would be hindered, which might also explain why we did not observe cell hopping for TiO_2 nanocubes, as opposed to TiO_2 nanotubes.

Based on the experimental data presented thus far, it is reasonable to infer that some nanoparticles can bind to certain structures in neuronal plasma membrane, which facilitates their connection to cellular motor proteins that interact with these membrane structures. This pivotal event, in turn, serves as the driving force behind the active transportation of nanoparticles along the axons. The extent of nanoparticle transportation over long distances is dependent on the neuron's capability to take them up, where lower uptake potentially allows for increased transportation. Consequently, inhaled nanoparticles may pose a conceivable threat to the brain, given their potential to be transported to this vital organ. Conversely, nanoparticles that are not taken up by neurons may not reach the brain, potentially mitigating any associated risks.

For instance, when considering TiO_2 nanocubes that were actively transported, their rapid uptake by neurons would likely impede extensive translocation to locations distant to the entry point. Due to the swift rate of uptake, the timescale required for such translocation might surpass the relevance within a typical lifetime. On the contrary, TiO_2 nanotubes, with a slower uptake rate, would most probably be capable of traversing long distances. Finally, nanoparticles such as MWCNT, are unlikely to undergo long-distance transport due to their limited interaction with motor proteins despite the fact that they are not taken up by the neurons. This is reflected in the absence of observable active transport. Instead, these particles move with the cells when directly positioned on neuronal bodies or are pushed around during cellular movement.

3.3 Long-Distance Transport Traits are Conserved in 3-Dimensional Spheroids

In our 2D *in vitro* system, the observed translocation routes were limited, and the cell density was significantly lower compared to the densely packed and complex environment of the human nasal mucosa and olfactory barrier. In such natural environments, neurons coexist with numerous other cells and structures, potentially influencing nanoparticle transport dynamics. Consequently, it remains uncertain whether the rules and characteristics of active long-distance transport, as observed in the simplified 2D system, apply in a larger, more complex 3D environment.

To address this question, we aimed to recreate a simplified 3D system comprising a densely populated spheroid created from differentiated SH-SY5Y cell line with the

established capacity to form long axons, crucial for nanoparticle long-distance transport. Additionally, the spheroid's dimensions were approximately 500 × 500 µm, sufficiently large to attribute significance to any nanotubes potentially found within it. We labelled spheroids with the CellMask Orange (CMO) plasma membrane label to facilitate visualization of all axons and incubated them with non-labelled TiO_2 nanotubes for a period of three days.

After incubation, we discovered TiO_2 nanotubes deep inside the spheroid in the form of aggregates and small particles. The majority of large particle aggregates accumulated near the spheroid's border (Figure 4, white asterisks), likely deposited and quarantined from the surrounding media. Interestingly, some larger aggregates were distant from the spheroid's border and penetrated almost 100 µm inside the spheroid, along the z-axis, (Figure 4A, white square). This depth represents the limit of detection of our confocal microscope, and it is possible that there were aggregates even deeper in the spheroid that we could not see. A diffusion simulation suggests that the observed penetration depth of these aggregates far exceeds what would be expected by diffusion only. Namely, according to the simulation, an aggregate with a 1 µm hydrodynamic radius would require at least 3 days to diffuse at the distance of 20 µm in the environment as viscous as the cell membrane (Figure 4D). Yet, Figure 4A and Figure 4B provide evidence of a 10 µm large aggregate situated at the depth of almost 100 µm within the spheroid in less than 72 hours. This discrepancy suggests that some other mechanisms, or active transport process, may be involved in facilitating the penetration of these aggregates so deep into the spheroid.

Upon investigating various sections of the spheroid for axon-like structures that could facilitate the active transport of nanotubes, we identified thick plasma membrane-rich structures marked with white arrows in Figure 4A. A closer examination revealed a notably higher presence of TiO_2 nanotubes on these structures compared to other areas of the spheroid (Figure 4C). Employing super-resolution STED imaging of small regions of interest (ROIs) containing these structures (Figure 4B, white arrows) we revealed that they comprise bundles of axon-like elongated, membrane-wrapped fibres, closely resembling nerve-like structures previously observed in another study [60]. Based on our findings regarding axonal transport of particles in 2D systems, we propose that the explanation for deep penetration of nanotube aggregates and the preference for spatial co-localization of these particles with these nerve-like structures lies in their function. These structures are most likely transport tracks that enable active translocation of nanoparticles within the spheroid.

To assess a potential role of identified nerve-like assemblies in nanotube transport, we conducted time-lapsed tracking of TiO_2 nanotubes positioned on one of these structures, approximately 50 µm within the spheroid. Indeed, the results revealed that TiO_2 nanotubes exhibited a motion along the portion of the bundle with a recognizable average speed of 0.5 µm min^{-1} (Figure 4E-G, Movie MS131 and MS132).

The deep penetration of nanoparticles within the spheroid indicates the potential conservation of transport mechanisms observed in simpler 2D systems to more complex 3D settings. Results of this experiment bolster our hypothesis that certain inhaled nanoparticles, including TiO_2 nanotubes, could indeed be transported through the olfactory nerve network, translocating from the nasal mucosa to interconnected brain areas, including hippocampus.

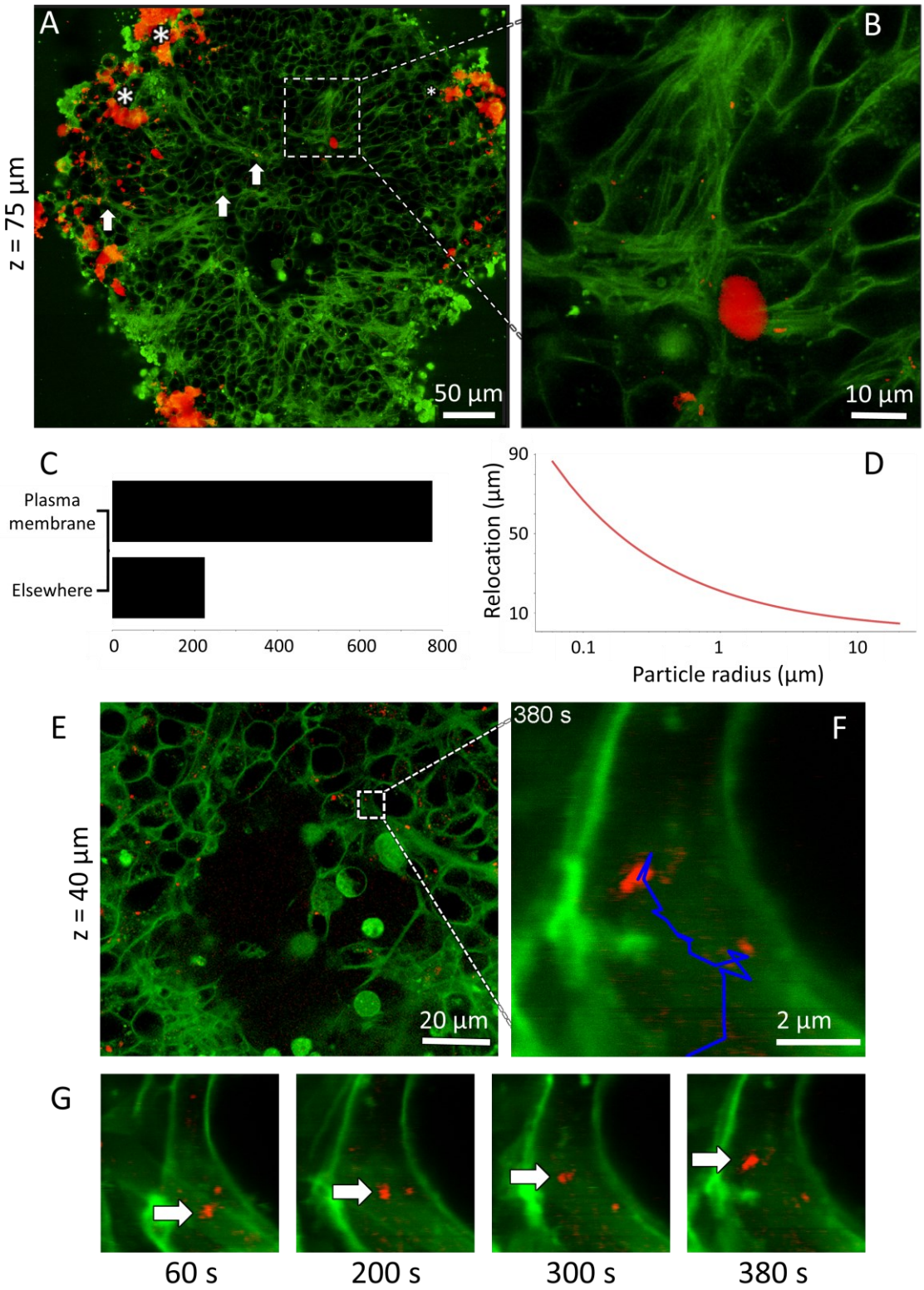

Figure 4: **An active transport of TiO_2 nanotubes with average speed of 0.5 µm min^{-1} conserved within large 3D neuron spheroids**. A) XY-section of a neuron spheroid at 75 µm depth, imaged as a 4X4 matrix with a 60X objective magnification. Neurons are labelled with the plasma membrane label CellMask Deep Red (green), exposed to TiO2 nanotubes (red) for almost 72 hours. White arrows indicate bundles of axons

forming nerve-like structures. White asterisks mark large nanotube aggregates at the spheroid's borders. The white square highlights region B) with a 10 µm large nanotube aggregate positioned deep within the spheroid after 72 hours; C) smaller nanotube singles and aggregates are scattered throughout the entire spheroid and predominantly co-localized with membranous structures; D) diffusion through the membrane modelled for objects with hydrodynamic radius in the range from 0.1 – 10 µm for 72-hour period; E) section of the same spheroid at 40 µm height, showing many small nanotubes scattered within the slice. The white square indicates region F) zoomed-in to show an ≈ 6 µm long trajectory of a nanotube aggregate tracked for 380 seconds within the spheroid; G) white arrows indicate the position of that nanotube aggregate at 60, 200, 300, and 380 seconds.

Chapter 4

Results and Discussion – Sporadic *in vitro* Alzheimer's Disease Model Replicates All Relevant Pathological Hallmarks

In this chapter, we present an innovative approach utilizing a wild-type human neuron-microglia co-culture *in vitro* system for investigation of the pathological changes observed in AD that can occur after inhaled nanoparticles get transported to relevant brain regions. Recognizing the pivotal roles of both neurons and microglia in AD progression [22], [24], [61], [62], our investigation revolves around exposing this co-culture to TiO_2 nanotubes, a nanomaterial for which long-distance transport has been previously confirmed.

We discover that the earliest response to nanotube exposure triggers structural impairments in axons, potentially impeding axon-dependent functions. For the first time, we correlate some of these early events, in cells that were not genetically modified towards AD, with the subsequent release and extracellular deposition of Aβ and tau in AD-like plaques. These changes coincide with the significant loss of neurons, a pathological event observed in biopsies of AD patients characterized by extensive brain atrophy.

The presence of microglia proves to be a pivotal factor, nearly entirely mitigating these pathological events. This finding underscores the invaluable role of brain defence mechanisms against inhaled foreign particles like TiO_2 nanotubes, illuminating a potential avenue for mitigating AD-related pathological shifts.

4.1 Early Events in Alzheimer's Disease

4.1.1 Axonal atrophy

The fundamental function of a healthy central nervous system at all stages of development is communication between and within neurons, which is primarily facilitated by axons through signal transduction. Axonal damage and degeneration, known as axonal

atrophy, has been identified as an early event in neurodegenerative diseases, closely associated with the loss of memory and brain functions [33], [63]. To investigate the effects of TiO_2 nanotubes on axonal health, we performed a time-lapse confocal imaging of live neuronal cultures that were exposed to these particles immediately before the experiment.

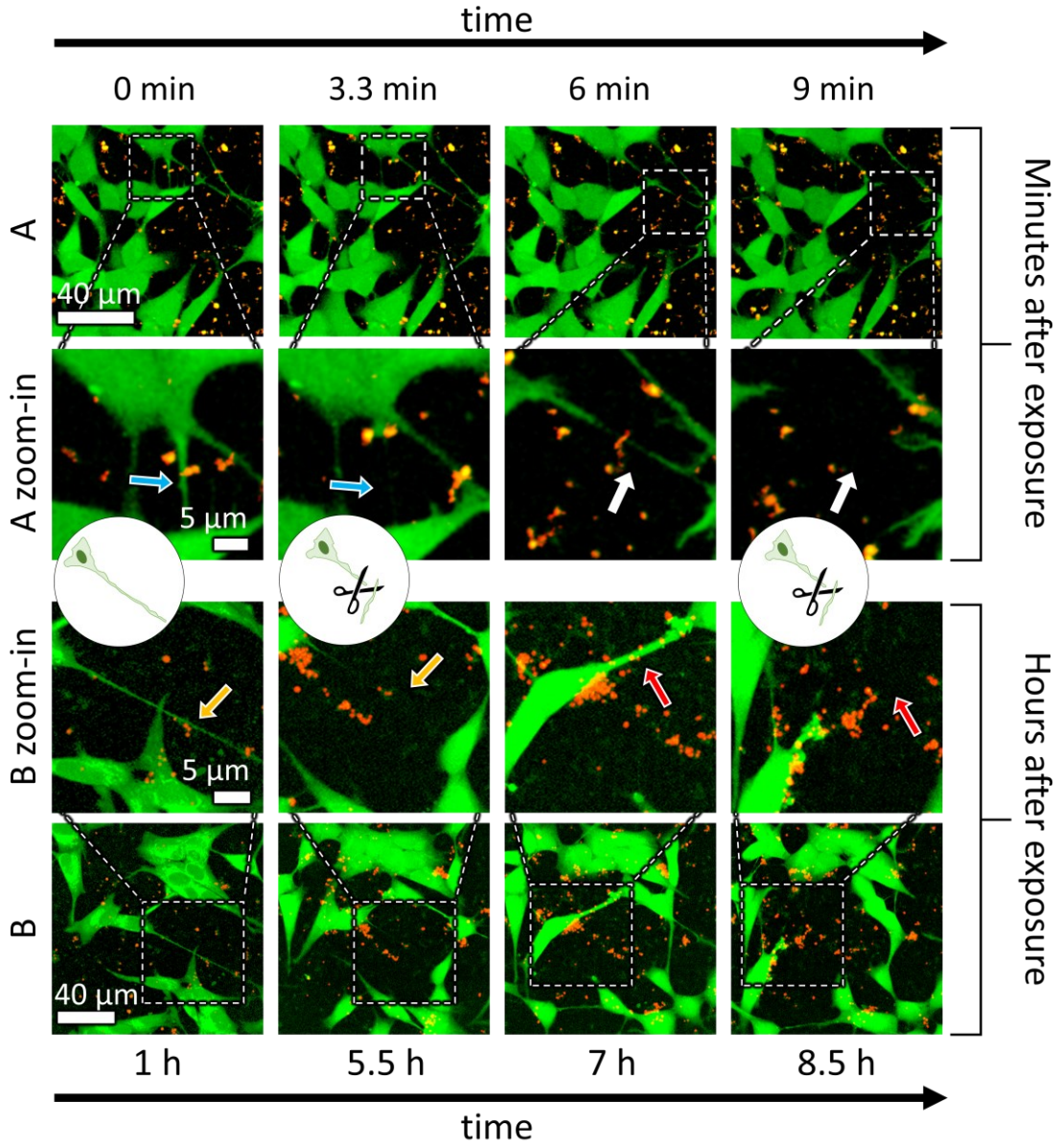

Figure 5: **Axonal atrophy caused by TiO_2 nanotubes**. Time-lapse of neurons labelled with CMDR showcasing axonal atrophy occurring A) within minutes after nanoparticle exposure, and B) several hours after exposure. Arrows in A and B zoom-ins point to neurites, which collapsed after contact with nanotubes.

Our results indicate that exposure to TiO_2 nanotubes caused rapid retraction of axons already within first minutes of exposure. This retraction occurred on axons that had nanotubes located on them, leading to the loss of connections between affected neurons

(Figure 5A zoom-in – 3.3- and 9-minute marks, blue and white arrows, respectively and Movie M5A).

The rapidity of the observed axonal atrophy led us to posit that this early loss of synapses can be attributed to the structural damage arising from the interaction of axons and nanotubes, including the observed tubulin severing (Figure S4) and lipid drainage due to the membrane wrapping, identified elsewhere [50]. Considering that neuronal communication depends on the axonal integrity, presence of particles, such as TiO_2 nanotubes anywhere in the central nervous system could have potentially adverse effects on this elemental neuronal function. When synapses brake, during axon disconnection, other previously connected neurons are at risk, due to the lack of synaptic input. This could contribute to the spread of neuronal degeneration in the process of secondary neuronal death [64]. The implications could be particularly pronounced if such effects were to be long-lasting.

The extended imaging of neurons exposed to nanotubes revealed that axonal atrophy persisted for hours after the initial exposure (Figure 5B zoom-in – 5.5 and 8.5 hours, yellow and red arrows, respectively and Movie M5B). This is important observation, because majority of nanoparticles is typically deposited from the media in a span of hours and one would intuitively anticipate that the axonal atrophy, occurring as a consequence of interactions between axons and particles, also drops.

This delayed axonal atrophy hints at multiple mechanisms of toxicity that extend beyond the immediate contact with the TiO_2 nanotubes and acute disconnection. It appears that axons that do not undergo acute atrophy continue to experience a more gradual ongoing damage that inevitably resulted in their collapse. However, the specific mechanisms responsible for this delayed damage remain unclear from current experiments. Nevertheless, during this period before the delayed axonal atrophy occurs, adverse effects of TiO_2 nanotubes may impair normal processes in axons and disturb neuronal homeostasis. This, in turn, may lead to changes in organelle dynamics, including mitochondria, making them a viable option for indicators of axonal health [65].

4.1.2 Mitochondrial fragmentation and transport impairment indicate axonal pathology

Within axons, tubulin acts as a "railroad" for mitochondria, facilitating their transport to distant regions of the neuron, away from the cell body. This transport is crucial for providing the energy needed to sustain neuronal activity and support essential processes such as protein and neurotransmitter synthesis at these distant sites, including synapses [66].

To assess axonal ability for mitochondrial transport, we performed time-lapse imaging over a 48-hour period, capturing the behaviour of mitochondria in the absence and presence of TiO_2 nanotubes (Figure 6A). Our findings demonstrate that mitochondria located near TiO_2 nanotubes exhibited lower transport speeds, compared to mitochondria in the absence of these nanoparticles, which were transported much faster. This is clearly seen in Figure 6C, where the distribution of average transport speeds of mitochondria located in axons

without TiO_2 nanotubes resulted in a bivariate distribution (blue), with one population at approximately 0.5 μm min^{-1} and the other around 7 μm min^{-1}. In contrast, mitochondria in axons clogged with nanotubes (red) moved with average velocity of 0.3 μm min^{-1}. Population of fast mitochondria was almost completely lacking in these nanomaterial laden axons, as can be seen by almost complete absence of the second peak on the velocity distribution in Figure 6C (red). Furthermore, a whole distribution is left-shifted indicating that both, slow and fast movement modes have been affected by TiO_2 nanotubes. However, we did not look into the distance covered by mitochondria within these two groups.

Mitochondria close to TiO_2 nanotubes showed extremely limited displacement, mostly oscillating in place or moving up and down without covering any distance further from the starting point (Figure 6A red arrows and Movie M6B). Consequently, they exhibited negligible displacements after analysis (Figure 6B, red line).

Similar transport impairments are known to occur regularly in traumatic brain injury. They are caused by axonal deformations resulting in the dislocation and accumulation of tau [37], transport products, axonal swelling, secondary axonal disconnection and Wallerian degeneration [65]. We too have observed instances of axonal swelling (MS151), also known as “axonal bulb” which is believed to represent complete axonal disconnection following cytoskeletal disruption correlated with secondary axonal disconnection that manifests as the retraction of axons [67]. Also, mitochondria can be seen accumulating in these swellings, indicating complete cessation of transport in those regions. Therefore, we suggest that the delayed axonal atrophy observed in our experiments is the so-called secondary disconnection, a well-known phenomenon in neuro pathology that is correlated with the cytoskeletal damage.

Contrary to mitochondria in nanotube-laden axons, mitochondria in axons free of this material displayed unrestricted and freely moving behaviour as indicated with blue arrows in Figure 6A (Movie M6A). These mitochondria also demonstrated large displacements (Figure 6B blue line) and no structural changes, such as axonal swelling or delayed atrophy.

These results suggest that TiO_2 nanotubes can disrupt axonal transport, either by clogging the axons or by damaging tubulin (Figure S4) and possibly other components essential for proper transport. As a consequence, mitochondria in axons affected by nanotubes were unable to traverse its entire length, leading to severe transport impairments. The absence of mitochondria in axons, caused by such transport impairments, can have significant consequences for neuronal function. Mitochondria are crucial for providing energy in the form of ATP to support various cellular processes distant to the cell body, including synapses. The impaired supply of ATP and other essential molecules due to disrupted mitochondrial transport can hinder synaptic communication [33] and compromise other previously connected neurons, leading to widespread dying [64], [65]. Mandelkow et al. have demonstrated detrimental consequences of impaired transport caused by the increased levels of tau in axons that often occurs during its destabilization through injury. The authors showed that the excessive tau clogged axons and stalled the axonal transport, even though axonal tubulin was visually intact. This destabilized ATP delivery, causing shortening of axons and increased neuronal susceptibility to stress [37].

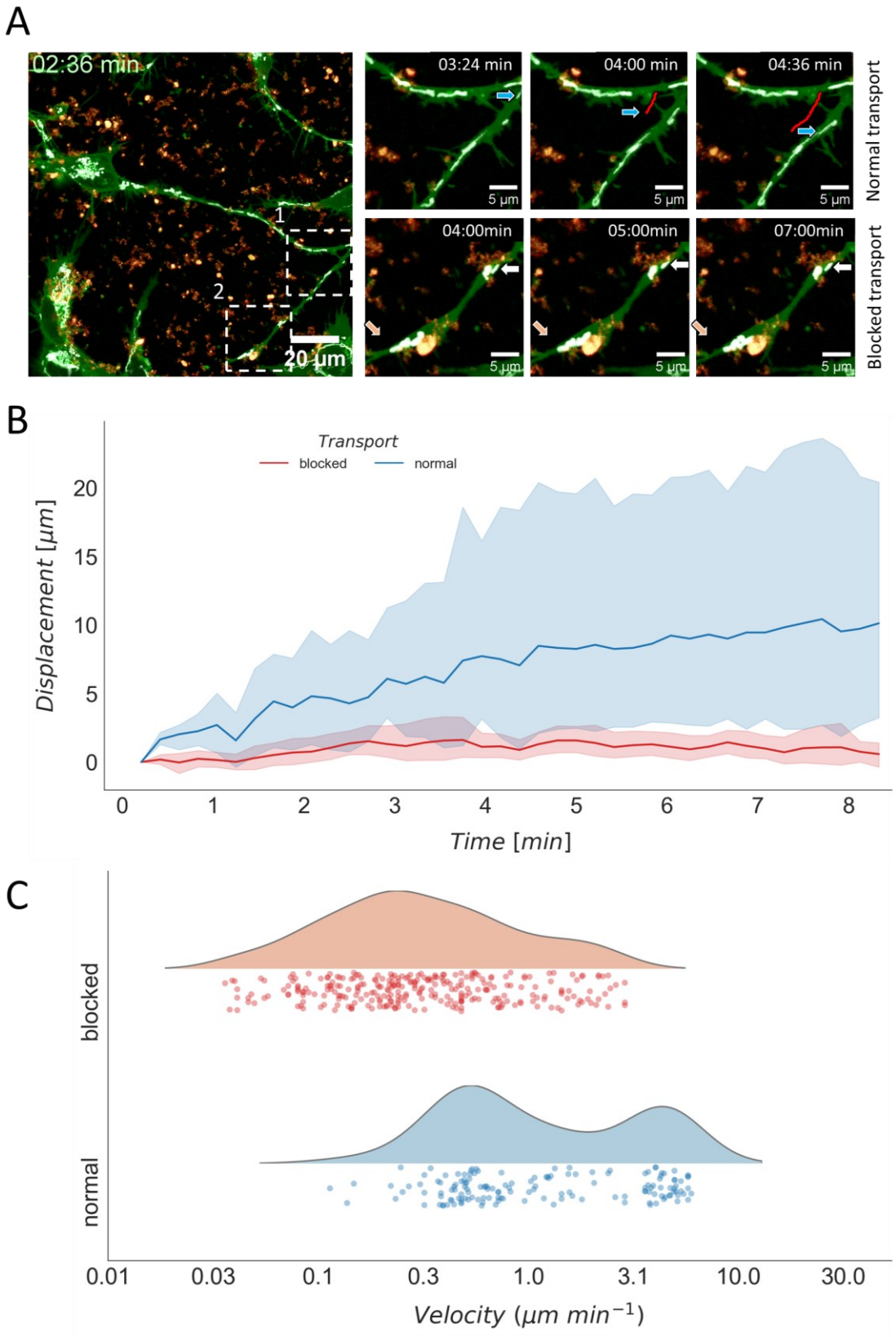

Figure 6: **TiO_2 nanotubes cause a reduction in mitochondrial average transport speed and block their translocation along axons**. Confocal micrograph of neurons

labelled with CMO (green) and MitoTracker Green (gray), exposed to 10:1 TiO_2 nanotubes. The image captures a single frame (at 02:30 min) from a time lapse acquired approximately one hour after the exposure to nanotubes. The white square marked with number 1 indicates a region of the axon where the path was unblocked by TiO_2 nanotubes. Mitochondrion in this region moved ≈10 µm in 1 minute as indicated by blue arrows and red trajectory. The white square with number 2 indicates the zone where TiO_2 nanotubes blocked the path of mitochondria that remained almost stationary for 7 minutes. B) Line plot showing the calculated distances covered by mitochondria in axons filled with TiO_2 nanotubes (red) and in those without them (blue). The analysis is based on tracks from 7 experiments; C) distribution of average velocities (µm min^{-1}) of the same mitochondria in axons with and without TiO_2 nanotubes. Each dot represents average velocity of one mitochondria trajectory.

Even though we demonstrated that TiO_2 can clog axons or damage tubulin, it is reasonable to hypothesize that they might also have adverse effects on other axonal constituents, including tau, that can contribute to the observed impaired transport. While assessing the localization of tau, or other intracellular proteins, within living neurons can be challenging, we propose an alternative approach, using mitochondrial morphology descriptors. As mitochondria shape is closely correlated with their functioning, certain changes in their morphology can indicate cellular stress or dysfunction [68]. By quantifying mitochondrial morphology descriptors, such as their fragmentation and aspect ratio, we can assess TiO_2 nanotube potential for adverse effects on the internal axonal components.

To do so, we closely tracked mitochondrial fusion and fission, quality control processes that ensure maintenance of healthy mitochondria and mitophagy of ones that are faulty [65]. Our observations revealed a striking transformation in individual mitochondria already within hours of exposure to TiO_2 nanotubes that spread to a whole population after 24 hours.

Detected transformation includes a sharp decrease of their aspect ratio, caused by the change from connected elongated to disconnected circular-shaped organelles. This phenomenon, known as fission, can be observed in mitochondria from nanotube exposed and unexposed neurons in Figure 7A (grey in fluorescence or white binary masks).

Mitochondria originating from unexposed neurons (CTRL-mask) maintain their elongated and branched structures consistently over the course of 24 hours, as evidenced by the blue magnifying glass highlighting selected mitochondria in a binary mask in Figure 7A. Conversely, following prolonged exposure to TiO_2 nanotubes, mitochondria exhibited a disconcerting inability to restore their elongated forms after undergoing fission. A significant portion of mitochondria within these neurons displayed a distinct circular morphology as early as 1-hour post-exposure, and this circular shape persisted even after 24 hours, as indicated by the red magnifying glass in Figure 7A (TiO_2-mask).

We conducted a comprehensive analysis of the aspect ratios across the entire population of mitochondria over time to further quantify the effects of observed fission. Analysis was conducted for both exposed and unexposed neurons, and the resulting distributions are depicted in Figure 7B. The red histogram corresponds to mitochondria from TiO_2 nanotube-exposed neurons, while the blue histogram represents mitochondria from control neurons.

Up to an aspect ratio value of 6, the two histograms are remarkably similar, potentially signifying the representation of the simplest shapes, beyond which mitochondria typically do not change (transparent histogram parts). However, the perceptible shortening of the mitochondrial length within exposed sample (red histogram), becomes evident as early as 5 hours (marked area between the two histogram fits in Figure 7B), underscoring the observed prevalence of fission throughout the mitochondria population of exposed neurons. The persistence of contraction of the histogram at the 24-hour mark provides additional confirmation that the mitochondria have indeed lost their capacity to revert to their initial elongated forms.

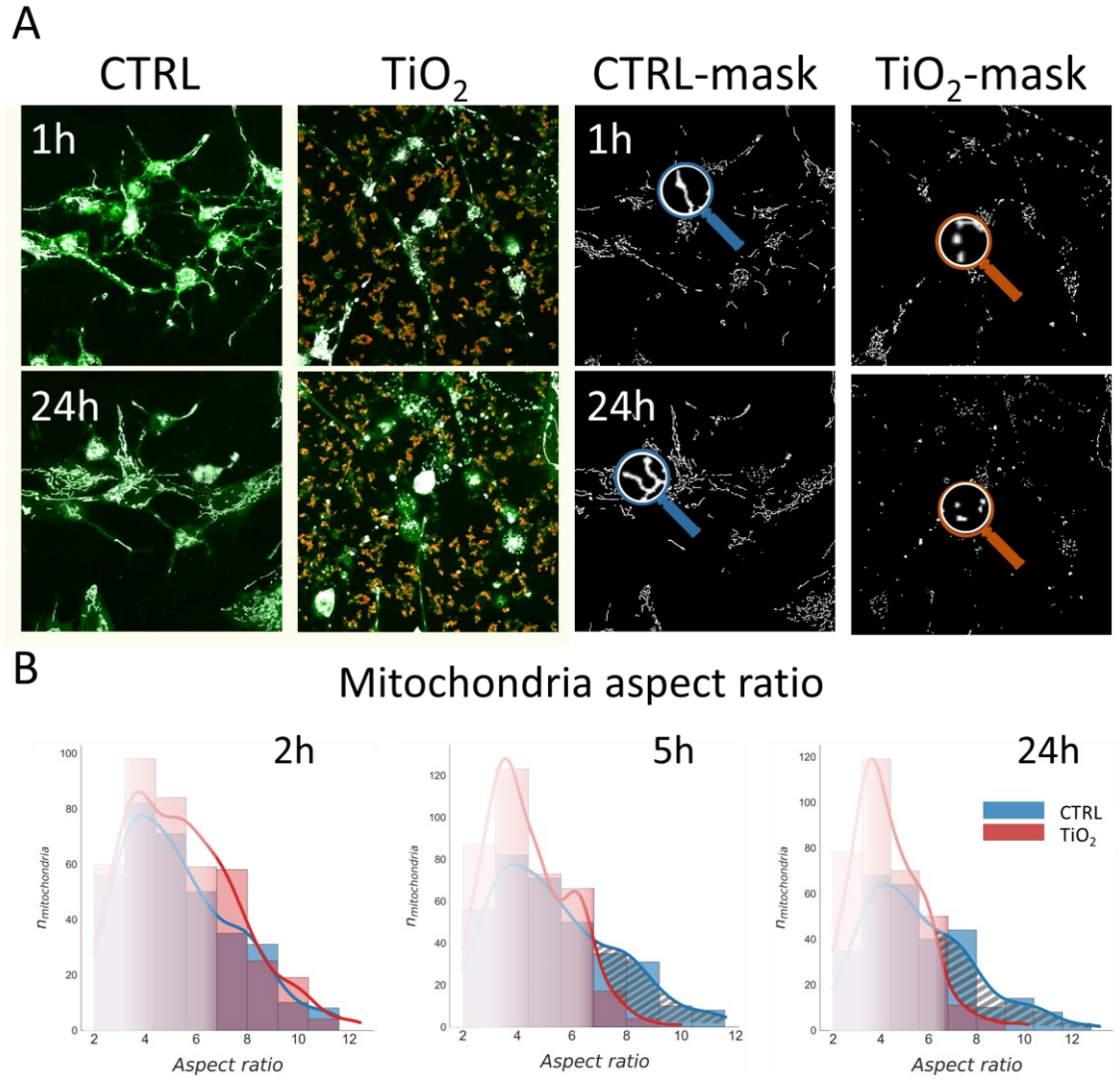

Figure 7: **Mitochondrial aspect ratio drastically decreases after exposure to TiO_2 nanotubes and remains reduced even after 24 hours**. Images of exposed and unexposed neurons are named "TiO_2" and "CTRL", respectively. A) Confocal fluorescent micrograph of neurons labelled with CMO (green) and MitoTracker Green (gray) exposed to a 10:1 surface dose of Alexa647-labeled TiO_2 nanotubes (red) (TiO_2), along with

unexposed neurons (CTRL) at 1 and 24 hours. Mitochondrial fluorescent signals were binarized to create masks for easier visualization of mitochondrial shapes. Blue and red magnifying glasses highlight representative mitochondria at each time point in control and exposure, respectively. B) Mitochondrial form masks were segmented into individual objects, and their aspect ratios were measured and plotted in histograms at 2, 5, and 24-hour time points. Notably, exposed neurons (red) exhibit a lack of large aspect ratio mitochondria compared to unexposed control samples (blue) at same time point.

These results indicate disruption of mitochondrial morphology control caused by TiO_2 nanotubes. Impaired mitochondria transport has been often observed in concert with fragmentation of the mitochondrial network, indicating at the fusion-fission disbalance, and extensively associated with compromised ATP production in axons, hindered transport processes, synapse loss and the onset of neurological disorders [22], [63], [65]. These links have been established not only through *in vitro* and animal models but also in the context of human AD patients [69], [70], [71].

As the detrimental effects of nanotubes on axons and intra-axonal structures persist, damage slowly accumulates, potentially leading to delayed axonal atrophy. If unresolved, such sequence of events could pose a risk of significant axonal and neuronal loss.

Interestingly, damaged axons have shown a remarkable ability to regrow synapses to full functionality. Study by Jin et al. demonstrated this neuronal trait within the living mice brain after stab injuries that severed a large number of neuronal axons [72]. Furthermore, Fu et al. found that microglia, in addition to neurons, played a crucial role in supporting neuronal survival and promoting axonal regrowth over an 8-week period after spinal cord injury [73]. Recognizing the regenerative potential of neurons and the supporting role of microglia, we propose that the fate of synapses, axons, and ultimately neurons will depend on their ability to remedy injuries suffered after exposure to TiO_2 nanotubes.

4.1.3 Arborisation does not rescue lost axons

To better understand axonal potential for recovery, our study involved a detailed time-lapsed examination of axonal structures, with a specific focus on the damage-recovery balance during a 30-hour incubation with TiO_2 nanotubes. The crucial role of microglia in axonal maintenance and recovery after injury prompted us to incorporate a human microglia cell line HMC3 (ATCC CRL-3304) to create a co-culture with neurons. Our aim was to investigate the interplay between TiO_2 nanotubes, neuronal axons, and microglia, in order to gain insights into the mechanisms underlying axonal degeneration and recovery in the presence of this nanomaterial.

Within the first hour of exposure to TiO_2 nanotubes, axons of neurons began to branch and develop numerous small neurite outgrowths along their entire length (Figure S9 and Movie M7-1, M7-2a and M72b). This process, known as arborisation, plays a crucial role in the synaptogenesis during the brain development [74], and remains prominent in the hippocampus of mature brains as new connections are established [75]. Small neurite outgrowths that formed on larger axon shafts during this process are referred to as dendritic spines. In a healthy nervous system, these dendritic spines are essential for the

establishment of new synaptic connections and are involved in memory formation processes [76], [77]. These specialized structures are the interface between presynaptic and postsynaptic axons, facilitating signal transduction. It has been observed that their density depends on the synaptic activity of a neuron: it increases if synaptic activity drops, and decreases when the stimulation is excessive [78]. Therefore, we decided to quantify this parameter and use it as a descriptor of neuronal potential to form new synaptic connections. The more dendritic spines a neuron has, the more potential new synapses it can form.

We conducted a comprehensive analysis of arborisation, which refers to the branching of axonal processes, in both mono- and co-culture of neurons and microglia, covering a substantial population of cells across several ROIs that spanned nearly 1.5 mm^2 and involved over 100 neurons per setting. The analysis detected and quantify numerous small protrusions that contribute to the overall increase in axonal perimeter, providing insights into the intricate structural changes of axonal outgrowths in response to TiO_2 nanotube exposure.

The analysis results, with each data set normalized to its initial value, revealed that arborisation of neurons in monoculture (Figure 8E, red line) started to decline after approximately 10 hours post exposure (Figure 8E, red line). Within 30 hours, exposed neurons in monoculture suffered almost complete loss of dendritic spines. In contrast, unexposed (control) monoculture of neurons exhibited a slight increase in arborisation (dashed green arrow between grey and red lines in Figure 8E indicates the difference). Interestingly, the arborisation dynamic of exposed neurons in the co-culture closely mirrored that of their control (Figure 8F-G), showing neither an increase nor a decrease of dendritic spine density following incubation with TiO_2 nanotubes.

To visually illustrate these findings, representative images of exposed monoculture used in the analysis (Figure 8D, red TiO_2) clearly show that neurons were heavily branched already 1 hour after exposure to nanotubes, but they lost their dendritic spines within the first 10 hours. While this was not apparent from Figure 8E (red line), due to data normalization, it explains the significant drop in arborisation on that same plot. Images of monoculture control (Figure 8D, gray CTRL), nanotube-exposed co-culture, and its control (Figure 8F blue TiO_2 and black CTRL, respectively) demonstrate the unchanged nature of their dendritic spines, thus aligning with their respective plots in Figure 8E and Figure 8G.

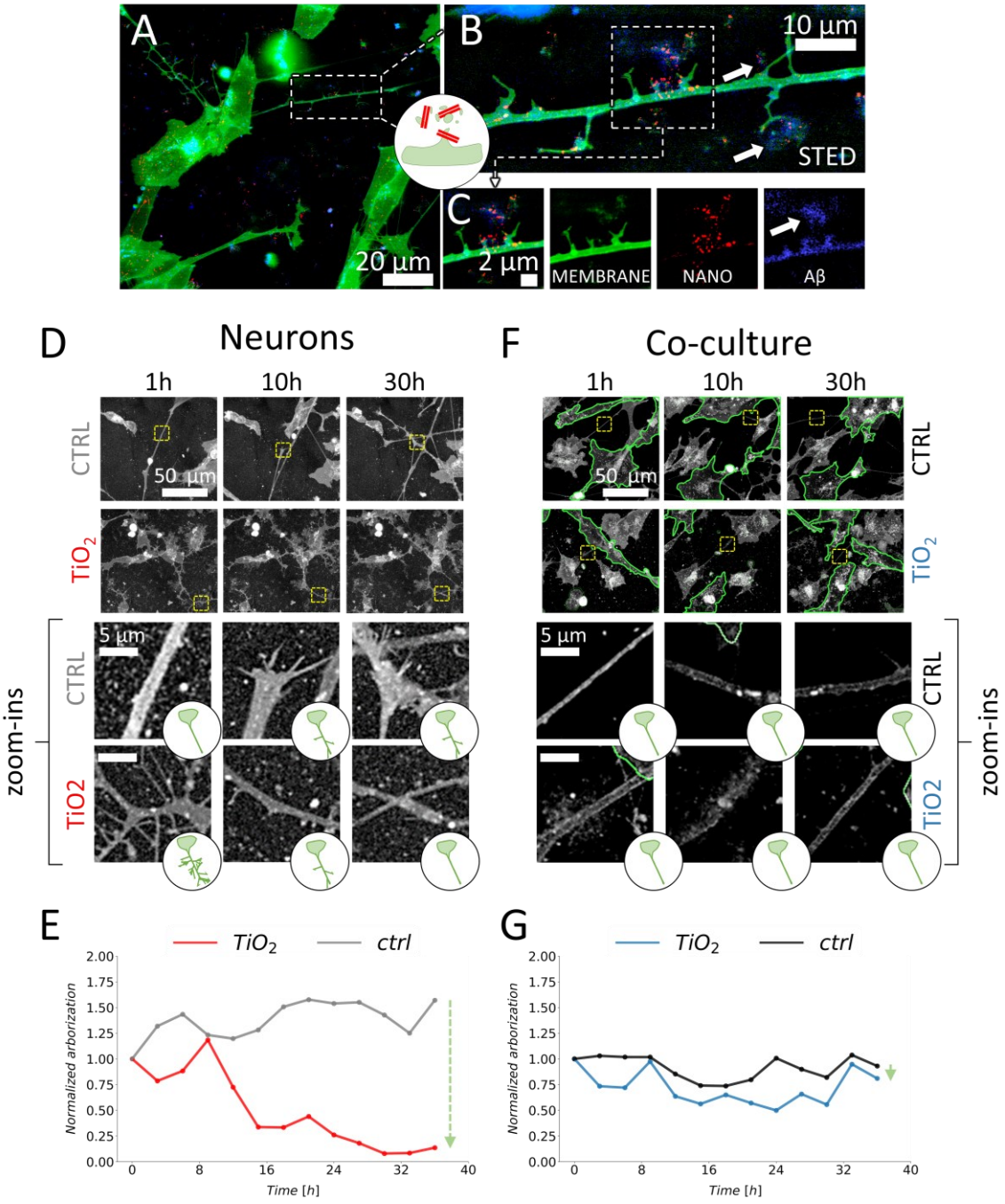

Figure 8: **Arborisation and dendritic spine atrophy caused by TiO_2 nanotubes**. A) Confocal fluorescent micrograph of neurons labelled with CellTracker™ Green (green) exposed to TiO_2 nanotubes (red) for 24 hours, along with fluorescently labelled primary anti-Aβ antibody (blue). The dashed square highlights the axon imaged with B) advanced super-resolution STED microscope, revealing dendritic spines protruding from the main axon shaft with diffuse Aβ signal around nanotube-damaged dendritic spines (white arrows). The dashed square is further decomposed in C) at individual channels, showing co-localization of nanotubes with damaged dendritic spines and Aβ signal, D) three representative time points from a time-lapse of monoculture of neurons (gray) exposed to

a 10:1 dose of TiO_2 nanotubes, showing axon arborisation in unexposed (CTRL) and exposed (TiO_2) samples. Zoom-ins of regions marked with yellow squares provide detailed observation, with cartoon pictograms depicting the level of branching; E) neurons on the images were binarized, and the arborisation descriptor is plotted. Gray and red colours correspond to unexposed and exposed samples, respectively; F) three representative time points from a time-lapse of co-culture of neurons (gray) and microglia (green contours) exposed to 10:1 dose of TiO_2 nanotubes showing axon arborisation; G) only neurons were binarized, and the ratio of precise to imprecise edge-length is plotted. Gray and blue colours correspond to unexposed and exposed samples, respectively.

Interestingly, similar temporal dynamics have been observed in other studies, in the absence of nanoparticles, following neuronal stimulation with neurotransmitters. Dendritic spines density was found to increase within minutes after neurotransmitter addition [79]–[81], and then undergo shrinkage on the scale of hours after neurotransmitter withdrawal [82]–[84]. This process is believed to be driven by the influx of calcium ions (Ca^{2+}), which activates a serine/threonine protein phosphatase called calcineurin. Calcineurin induces the severing of F-actin, which forms the base of a dendritic spine [81], [82], [85], [86]. In our experiment, there might be another plausible explanation for the drop in dendritic spine density. As neurites enlarged their surface area through extensive branching, they may have come into more frequent contact with TiO_2 nanotubes, resulting in an increased injury per unit of time due to tubulin and actin damage, as well as the drainage of lipids, proteins, and other cellular constituents that occur after interaction with this material [49]. These damaging effects could have contributed to the observed reduction in dendritic spine density over time.

To explore this hypothesis further, we employed a super-resolution STED imaging of axons of neurons exposed to TiO_2 nanotubes. By comparing axons that had dendritic spines with and without nanotubes in the same FOV (Figure 8A-B), we clearly confirmed that nanotubes had detrimental effects on these structures. In Figure 8B-C, small parts of dendritic spines (green) were scattered around red TiO_2 nanotubes (white arrows and the zoom-in box), indicating that nanotubes damaged dendritic spines, leading to their fragmentation. Furthermore, the presence of a distinct green haze of plasma membrane label surrounding the nanotubes in Figure 8B further bolsters our previous observation. This finding suggests that the interaction between the nanotubes and dendritic spines resulted in disruption of the plasma membrane leading to the free diffusion of phospholipids together with our label, previously incorporated in the membrane. What is more, by adding fluorescently labelled anti-Aβ antibodies, we were also able to observe diffusion of Aβ(blue) at these exact sites of nanotube-induced damage (Figure 8B-C). The Aβ is a transmembrane protein abundant in axons and synapses [14], [15]. Its release during structural damage has been established before, also in human brain trauma patients, who had increased levels of Aβ close to the sites of trauma correlated with the mechanical stress and injury of axons [87], [88].

Overall, the co-localization of TiO_2 nanotubes with fragmented dendritic spines surrounded by the haze of plasma membrane and Aβ strongly supports the notion that this material exhibits destructive effects on spines. The stark contrast observed in dendritic spines that had no nanotubes in proximity (Figure 8B), showing unharmed spines without the surrounding haze of plasma membrane or Aβ, further reinforces this assumption.

We propose that the transient arborisation was a neuronal response to a rapid axonal atrophy caused by nanotubes. Neurons expressed numerous dendritic spines in an attempt to form new synapses to compensate for the incurred losses. However, the axonal arborisation, typically correlated with the regrowth and greater network complexity, inadvertently increased axonal surface area and consequently amplified the extent of structural damage upon contact with nanotubes. It likely led to a higher degree of tubulin destruction, as well as the drainage of lipids, proteins and other biological molecules per unit of time. Consequently, exposure to TiO_2 nanotubes culminated in a reduction of dendritic spine density. This phenomenon mirrors observations in patients afflicted with depression, AD and numerous other neuropsychiatric disorders [77], [89], [90]. Notably, AD patients lost their ability to form new synapses and accordingly exhibited a significant reduction in synaptic density relative to cognitively healthy individuals. Furthermore, their cognitive prowess was in a direct correlation with the synapse density [91], [92].

Intriguingly, nanotube-exposed neurons in the co-culture appeared remarkably similar to their control at the end of the experiment without any changes in dendritic spine density. The primary distinguishing factor between the monoculture and the co-culture was the presence of microglia, which led us to believe that the absence of discernible response in terms of dendritic spines may stem from the microglia's potential to mitigate axonal and synaptic harm—factors that originally propelled the outgrowth of dendritic spines. This hypothesis prompted us to better comprehend the mechanism by which microglia safeguard axons after exposure to TiO_2 nanotubes.

4.1.4 Guardians of neurons – microglial phagocytosis is a key protective mechanism

To further assess the microglia role in the prevention of detrimental TiO_2 nanotube effects, we focused on interactions between neurons and microglia during the 14.5-hour incubation with this material. Acquired time-lapse micrographs were obtained with the 20x magnification objective that enabled a significant enlargement of the FOV surface area to approximately 0.2 mm^2, encompassing approximately 100 cells and imaging at the higher frame rate to obtain better temporal resolution.

We have discovered that microglia were actively engaged in removing hazardous nanotubes from the environment, as well as from the laden neurons. This process, known as phagocytosis, is one of the crucial microglial functions. It is a fundamental mechanism employed by professional phagocytes to maintain homeostasis by clearing foreign substances, invading microorganisms, damaged cells, and remaining cellular debris.

Visual representation of these phagocytic events is captured in representative images taken at time points 1, 7, and 14.5 hours after exposure, as shown in Figure 9A. In the lower portion of the FOV, where microglia (blue cells) were abundant (indicated by the blue square brackets), the red signal corresponding to TiO_2 nanotubes disappears from the neuronal surroundings within 7 hours (Figure 9A). The process of nanotube phagocytosis from laden neurons within the region highlighted by the blue dashed square in Figure 9A is further illustrated through a series of zoom-in screenshots in Figure 9C, along with a corresponding video in Movie M9C.

To quantitatively evaluate the phagocytosis of nanotubes from neurons, we calculated the integral of nanotube scattering intensity within neuronal and microglial binary masks individually over time, normalizing it to their respective surface areas at each time point. Results plotted in Figure 9D emphasize the flow of material from neurons to microglia as indicated by the downward trend of green line and rising of the blue line increase, respectively. Conversely, in the upper half of the FOV, where microglia were scarce (indicated by the red brackets), nanotubes were scattered haphazardly throughout space or accumulated in the large aggregates that formed on neurons.

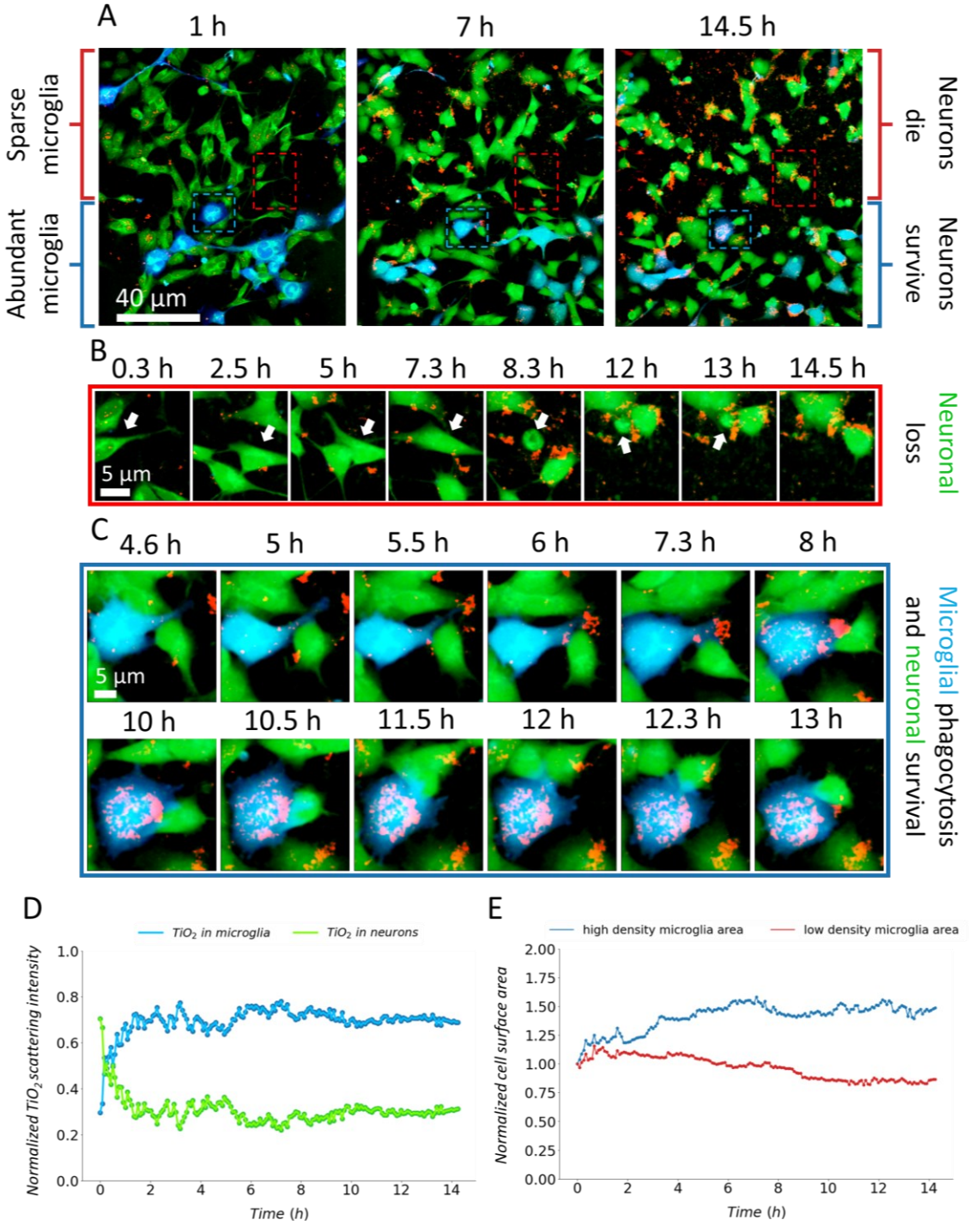

Figure 9: **Microglia safeguard neurons by phagocyting TiO_2 nanotubes**. A) Time points 1, 7 and 14.5 hours of the time-lapse of co-culture exposed to 10:1 surface dose of TiO_2 nanotubes (red) for 14.5 hours. The region of high microglia (blue) abundance is marked with blue square brackets, while the region of low microglia abundance and more dead neurons (green) with red square brackets; B) a zoom-in from the region with low microglia abundance (red-dashed square) showing lone neurons taking up TiO_2 nanotubes and undergoing cell death, indicated by the round-up morphology; C) a zoom-in from the region with high microglia abundance (blue-dashed square) showing microglia (blue) phagocytizing TiO_2 nanotubes (red) from neurons that did not undergo cell death; D) integral of the nanomaterial scattering intensity within neuronal mask (green line) and microglial mask (blue line) representing the amount of material taken up by neurons and microglia, respectively, and E) surface area of neurons in low-microglia-abundance region (red line) and high-abundance-microglia region (blue line).

Through the active removal of hazardous TiO_2 nanotubes from neurons, microglia promoted their survival. This was particularly evident in the lower half of the FOV, where a majority of neurons remained viable, characterized by their elongated morphology. In contrast, in the absence of microglia, neuronal viability was reduced, with individual neurons initiating the process of cell death already around 7 hours (Movie M9B) after exposure. These dying neurons can be identified by distinct features, such as the round-up bodies, a characteristic trait of apoptotic cells [64] (Figure 9B starting after 7.3 hours).

As neurons rounded-up and shrank during apoptosis, their surface area diminished accordingly. Thus, we utilized neuronal surface area as an indicator of cellular growth and death. This parameter was quantitatively assessed in regions with abundant and scarce microglia and subsequently plotted in Figure 9E with blue and red lines, respectively. The results highlight a decline in neuronal surface area in the absence of microglia, in contrast to their surface area increase in the presence of microglia, further reflecting a crucial role of these immune cells in safeguarding neurons.

To further validate our findings, we conducted a larger-scale experiment to explore the impact of microglial density and phagocytosis on neuron survival after exposure to TiO_2 nanotubes. This extended experiment involved monitoring 10 different ROIs over a 36-hour period. Each ROI covered an area of 130x130 μm^2 and was observed using a 60X magnification objective. We captured images in 3D, taking slices at heights of 0 µm, 3 µm, and 6 µm, allowing us to better distinguish nanotubes within cells from those outside and quantify phagocytosis more accurately. Additionally, within each ROI, we tracked changes in neuronal and microglial surface areas, shedding light on their growth patterns, and the exchange of material between these compartments over time.

The graphical representation in Figure 10, visualized as a 4D scatter plot, offers a depiction of the interrelationships among the examined variables. Time is denoted along the x-axis, while the y-axis signifies neuronal surface area, a proxy for neuronal viability. The z-axis delineates the ratio of nanomaterial scattering within microglia to that within neurons, serving as an indicator of phagocytic activity. The colour of each data point corresponds to the microglial proportion within the specific ROI, according to the colour legend.

By examining the plot, a bifurcation in the data along the temporal dimension emerges, resulting in the two distinct clusters. The cluster on the left (green ellipse), predominantly composed of green and yellow dots, corresponds to regions of higher microglia presence. In this cluster, microglia demonstrated an increasing trend in nanotube phagocytosis (z-axis). Additionally, neurons within this cluster divided, leading to higher surface area values along the y-axis. Conversely, the other cluster (red ellipse) is primarily comprised of red-shaded dots, with some yellows interspersed. This cluster represents ROIs where the outcomes varied between instances where microglia were moderately abundant and neurons neither divided nor died (yellow dots), and cases where neuronal death occurred in the absence of microglia (red dots), as indicated by the downward trend on the y-axis.

A closer analysis of individual regions in Figure S14 reveals an intriguing pattern. Regions from the first cluster that contained dividing neurons had very few microglia initially. However, these regions soon experienced an increase in microglial presence, as characterised by the transition of initial red dots into subsequent green dots. The accumulation of microglia correlated with the progressive increase in phagocytosis of dangerous nanotubes (z-axis), likely enabling division of neurons. In regions where microglia were moderately present initially (yellow-orange dots) and remained so throughout the experiment, neuronal surface remained largely unchanged. Conversely, instances where the initial microglia fraction remained low and failed to increase before the 10-hour mark post-exposure were marked by a decline in neuronal surface. This underscores the detrimental impact of nanotube exposure on neurons in the absence of microglial intervention.

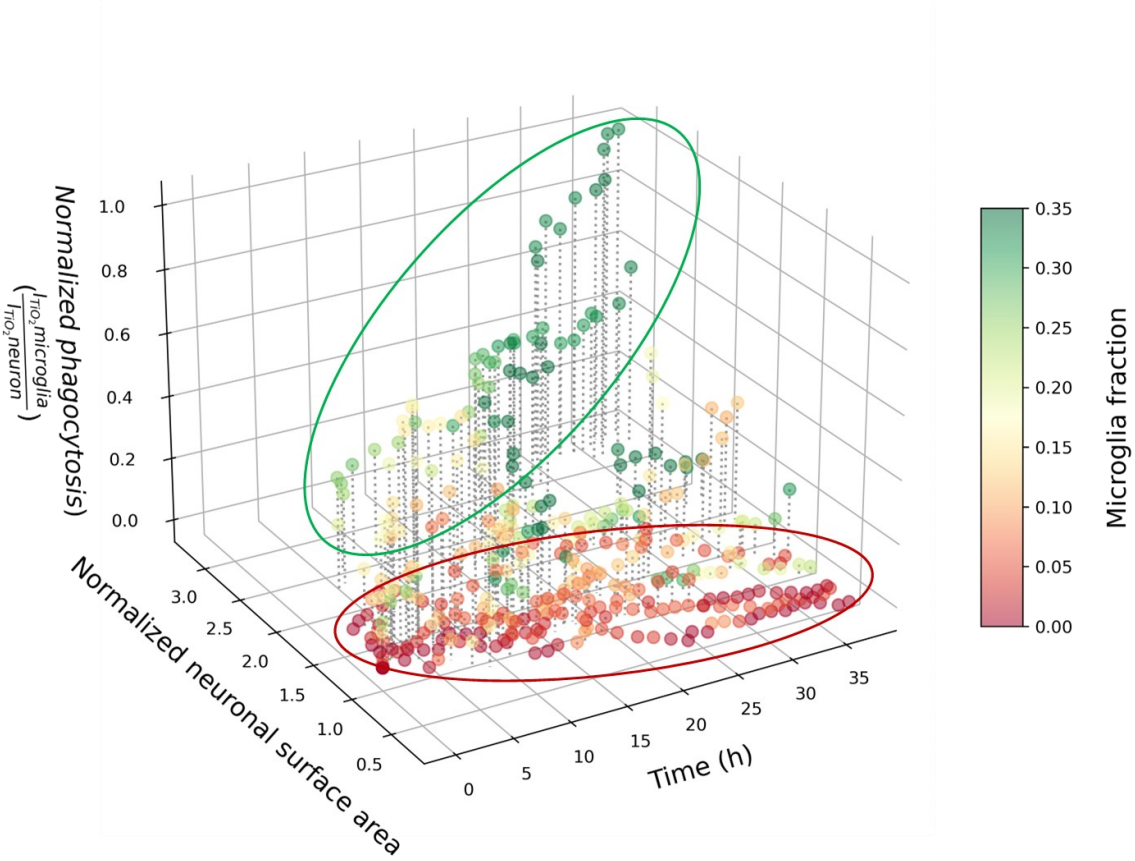

Figure 10: **Microglial in vicinity of neurons phagocyte hazardous TiO_2 nanotubes and promote neuronal survival**. Time-lapse imaging of 10 ROIs of a co-culture of neurons and microglia was conducted for 36 hours. Image segmentation of neurons, microglia and nanomaterial was performed for all cells in ROIs for all time points. On the y-axis, neuronal surface area values of each ROI were normalized to their respective first value. Time is represented on the x-axis. The fraction of microglia in cell population was color-coded according to the colour scale. On the z-axis, the integral of TiO_2 nanotubes scattering intensity in the microglial mask, normalized to the integral of material scattering intensity in the neuronal mask, represents accumulation of material in microglia – interpreted as phagocytosis.

Gathering from our results, we propose that microglia play a critical role in protecting neurons from the detrimental effects of TiO_2 nanotube exposure through phagocytosis. Microglia effectively prevent direct contact between nanotubes and neurons by removing them from the neuronal environment. Even when nanotubes come into contact with neurons and local microglia are nearby, the microglia swiftly remove the nanotubes, thereby ensuring neuronal safety. This mechanism also offers a plausible explanation for the consistent dendritic spine density observed in co-culture settings during our arborisation experiments. The preservation of dendritic spines in the presence of microglia is likely due to phagocytosis of nanotubes that prevented their direct interaction with axons. As a result, axons remained intact, and neurons did not trigger compensatory regrowth mechanisms, arborisation, to restore lost connections.

These findings are consistent with recent research conducted by Shabestari et al., which demonstrated that ablation of microglia from AD mice brains resulted in a more severe form of AD and premature death. Remarkably, when the wild-type microglia were reintroduced back into brains of the same animals, authors have reported fast repopulation of the microglia niche and a complete reversal of pathological changes observed during their absence [93]. In a separate study, Lee et al. have transfected microglia with the human TREM2 gene to enhance their phagocytic activity within AD mice. Brains of these animals showed reduction in neuritic damage and Aβ plaque burden, compared to non-enhanced AD mice. Furthermore, enhanced mice demonstrated improvement in cognitive deficit, measured with the fear-conditioning test. In this hippocampus-dependant memory test, TREM2-enhanced mice performed almost as well as the wild type mice, while AD mice showed robust cognitive deficits [62]. On the other hand, the inhibition of TREM2 gene in another study showed that almost 40% less hippocampal microglia associated with plaques and that the neurite damage in these animals was significantly higher than in the wild types [61].

4.2 Recapitulating Late-Stage Alzheimer's Disease Characteristics *in vitro*

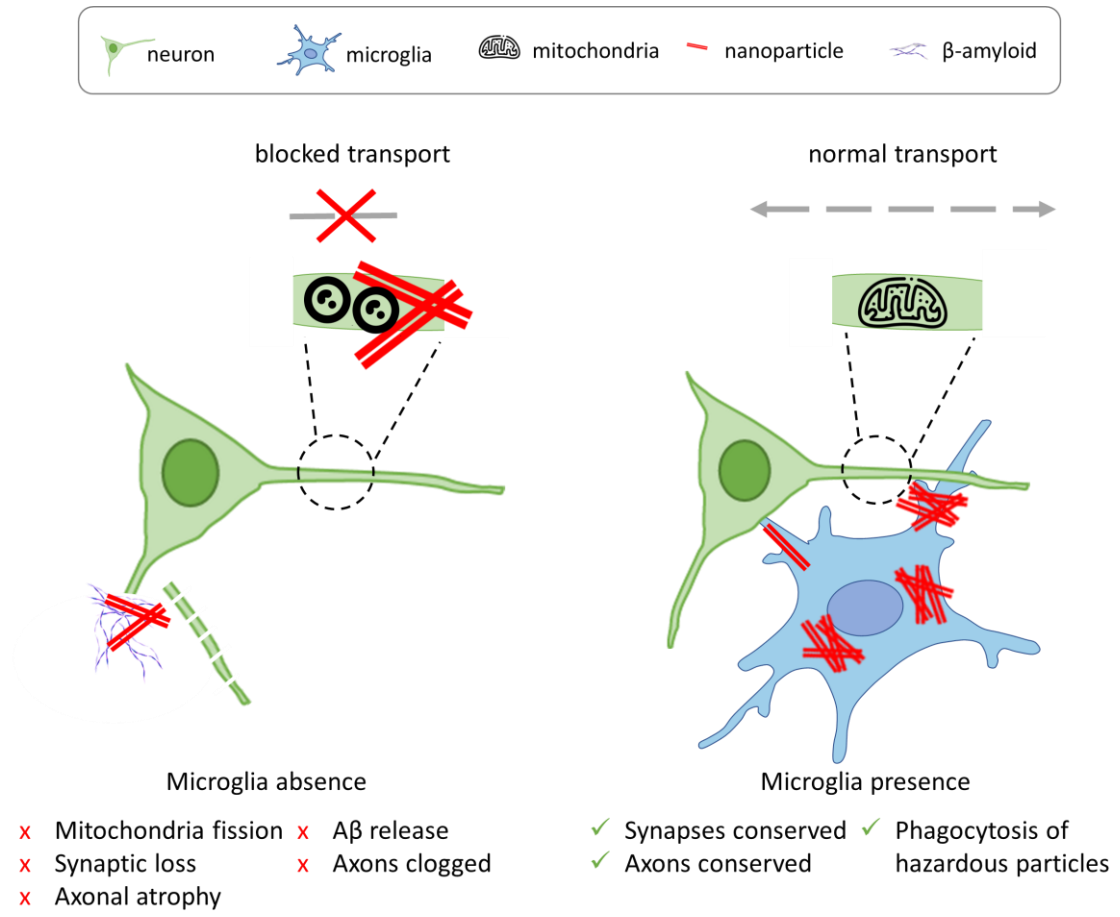

In a brief summary of the previous chapter, it is important to note that upon the initial interaction with TiO_2 nanotubes, neurons experienced rapid axonal atrophy. While some axons initially appeared visually intact, they later suffered impairments, including disrupted mitochondrial transport, irregularities within axons, and delayed axonal atrophy. To counter the loss of connections, in the process of arborisation neurons initiated the formation of numerous dendritic spines along their remaining axons, in an effort to increase the potential for new synapse creation. Surprisingly, this compensatory process inadvertently increased the frequency of contact with nanotubes, ultimately exacerbating axonal degeneration and leading to neuronal demise.

Remarkably, the presence of microglia had a significant impact on this process, reducing or even mitigating axonal atrophy and neuronal loss. Microglia demonstrated active phagocytosis of hazardous nanomaterial, thus safeguarding axonal integrity and preserving neuronal vitality even during prolonged exposure to TiO_2 nanotubes.

Nonetheless, it is crucial to underline the nature of the observed events in this study up to this point. While axonal atrophy, mitochondrial pathology, synaptic atrophy, neuronal loss, and microglial activation are shared characteristics across various neurodegenerative diseases, each specific neurodegenerative disorder also presents distinct

events unique to the affected brain region. Although these specific events were not experimentally addressed in our study so far, they were briefly mentioned earlier.

Consequently, the upcoming chapter will delve into the potential of our *in vitro* model to replicate pathological events more specific to AD patients. This will encompass phenomena like Aβ release, tau dislocation, their deposition in AD plaques and the potential of microglia to modulate these processes. These events are repeatedly associated with the advanced stages of the disease, contributing to brain atrophy, cognitive decline, and ultimately, mortality [24], [33] ,[38], [92].

4.2.1 Aβ and tau containing plaques form after exposure to TiO_2 nanotubes *in vitro*

To explore whether TiO_2 nanotubes exposure results in the accumulation of Aβ and tau extracellularly, we incubated neurons with this material for 2 days. To facilitate visualization of neurons, we added the cytosolic label CTG (Figure 11A-C green), which fluoresces only when it enters the cytosol after cleavage by cytoplasmic esterases [96]. For identification of potential extracellular deposits of Aβ, we employed immunostaining with a mouse monoclonal antibody raised against amino acids 1-40 of Aβ of human origin, recommended for detection of APP and Aβ (Figure 11A-C blue). Finally, we labelled the extracellular tau deposits with tau (Tau-5) mouse monoclonal antibody (Figure 11A-C white) and imaged samples after 48 hours of incubation with nanotubes.

Upon inspection of micrographs, we conclude that our results are consistent with imaging studies and investigations of postmortem AD brains, showing protein deposits containing both Aβ and tau, closely resembling structures observed in mice and patients by He et al [97]. To determine the properties of extracellular Aβ plaques, we analysed 15 ROIs, each covering 400 x 400 μm^2. We plotted properties of over six thousand plaques in a 5-dimensional graph in Figure 11F. The x, y, and z axis represent surface densities of the tau protein, Aβ, and the density of the cytosolic label, respectively. Each sphere in the graph represents one plaque, with the size of the sphere proportional to the plaque radius and the colour representing the density of the nanomaterial according to the colour scale. Our analysis revealed that majority of the plaques contained Aβ, as indicated by the y-axis in Figure 1F. These plaques also had nanomaterial (colour) and cytoplasmic components (z axis). Interestingly, some plaques lacked tau (x axis), whereas others contained lots of it. This observation aligns with the heterogeneous nature of plaques found in AD patients, where there are oscillations in abundance of all plaque components save for Aβ, which is universally present [98]. Notably, the amount of Aβ in our plaques was proportional to the amount of cytosolic label observed, indicating that it originates from within the cells because CTG label does not fluoresce if not cleaved by esterases present in cell cytoplasm (Figure 11F distribution of green dots in an amyloid-neuronal cytosol plane). This is in accordance with the findings of initial intracellular plaque formation and subsequential extracellular accumulation of fibrillar Aβ [99], [99], [100]. Moreover, many other cell proteins have been identified within plaques. For example, a comparison of biomolecules from within Aβ-rich plaques of human plaque regions versus non-plaque regions of AD patients and healthy controls revealed significantly higher levels of various neuronal proteins [12], [101], [102], further strengthening the idea that the plaques initially form within the neuron.

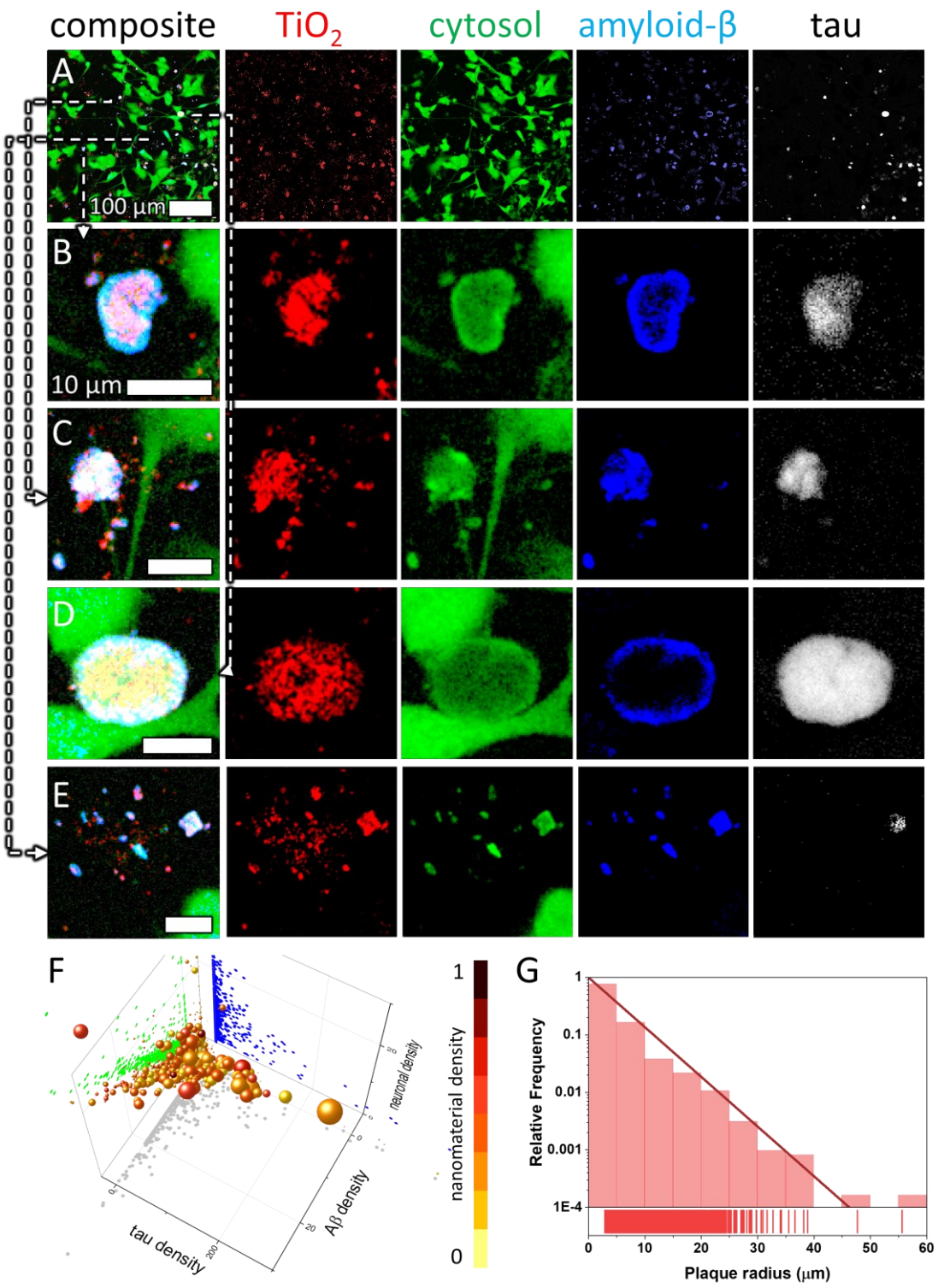

Figure 11: **SH-SY5Y-derived neurons exposed to anatase TiO_2 nanotubes form Aβ and Tau protein-containing extracellular plaques and show neurite atrophy**. (A) Representative image of differentiated SH-SY5Y cells in culture. Note the altered morphology and pronounced neurite outgrowth upon differentiation. Live cell culture was stained with cytosolic fluorophore CellTracker™ Green (green), which fluoresces only

within the cell, a mouse monoclonal antibody raised against amino acids 1-40 of Aβ of human origin, for detection of APP and Aβ (blue), and Tau-5 mouse monoclonal antibody against total tau (white). (A) Representative image with large field of view; (B-E) examples of heterogeneous extracellular plaques at higher magnification: B-D) large plaques with low Aβ density and high tau density; E) small plaques with high Aβ density and low tau density; (F) properties of all the Aβ plaques from 15 ROIs, each covering 400 x 400 μm^2 in terms of surface densities with x-axis: tau antibody, y-axis: Aβ-antibody, z-axis: neuronal cytosolic label, size of a sphere: plaque radius, and colour: density of nanoparticles in a plaque, each sphere representing one plaque. Most plaques contain Aβ, nanomaterial, and cytoplasmic components at their core, while tau can be missing; (G) the size distribution of the plaques, showing exponential decay of the number of plaques versus plaque size.

The size distribution of plaques follows the power law (Figure 11G), with most plaques having a radius below 40 μm, corresponding to cross-section area of 5000 μm^2. The size distribution, including the power-law behaviour and maximum size, is similar to the distribution of Aβ oligomeric structures observed *in vitro* on lipid membranes by Tahirbegi et al. [103] and *in vivo* in AD mice brains [61]. However, the plaque sizes we observed are larger than suggested by Serrano-Pozo et al., who showed that in AD patients maximum plaque sizes reach up to 500 μm^2 [104]. Nevertheless, the size of plaques seems to be loosely governed by the density of tau and Aβ proteins within them. Larger plaques tend to have a higher density of tau, and smaller ones have higher Aβ density (Figure 11D-E – small plaques have low density of tau (gray) while large ones have a lot of it).

Exposure of neurons to TiO_2 nanotubes confirmed that the presence of this material induces the deposition of both Aβ and Tau into extracellular plaques. However, it is important to note that this observation was based on a neuronal monoculture system and a single 48-hour time point. Although it suggests a causal relationship between TiO_2 nanotubes and plaque formation, because nothing else was changed except for the addition of TiO_2 nanotubes compared to the unexposed control, the static nature of the experiment limits our interpretation of the dynamics involved in the process. It is crucial to investigate the progression of plaque formation in time and its modulation by microglia to gain a comprehensive understanding of the underlying mechanisms.

4.2.2 Microglia attenuate the late-stage Alzheimer's disease progression

To investigate the spatiotemporal distribution of Aβ plaques in relation to the presence of TiO_2 nanotubes and the interactions between neurons and microglia, we conducted a time-lapsed experiment using both monoculture of neurons and co-culture with microglia. Both neurons and microglia were labelled with the plasma membrane label CMO, while cytoplasmic CTG label was used specifically for microglia to distinguish them from neurons and facilitate the subsequent analysis. Aβ was labelled with the fluorescently labelled primary anti- Aβ antibody, as before. We selected 10 different ROIs, each with a surface area of 130 x 130 μm^2. To capture detailed information, we acquired images at three different z-positions within each ROI, covering 6 μm in height, using a 60x magnification objective.

During the initial 24-hour period following the exposure to TiO_2 nanotubes, both monoculture (Figure 12B) of neurons and the co-culture with microglia exhibited relatively undisturbed behaviour (Figure 12H). Notably, the size of TiO_2 aggregates (red) devoid of Aβ (blue) in the monoculture was already large at 3 hours after exposure, compared to the co-culture, where the nanomaterial seemed much more homogeneously dispersed. Importantly, this distinction occurred despite the use of the same material identical conditions for both setups. The underlying reason for this discrepancy remains elusive at present. Regardless of that, in monoculture, large plaques rich in Aβ, TiO_2 and membrane (green) components occurred only at later time points accompanied with the loss of axons and neurons (Movie M8-1 and Figure S28A). Similarly, such plaques with all three components were also observed in the co-culture, yet they were notably smaller in size by almost an order of magnitude. Furthermore, the extensive neuronal loss that occurred in the monoculture was not observed to the same extent in the co-culture (Figure 12H, Figure S28B and Movie M8-2).

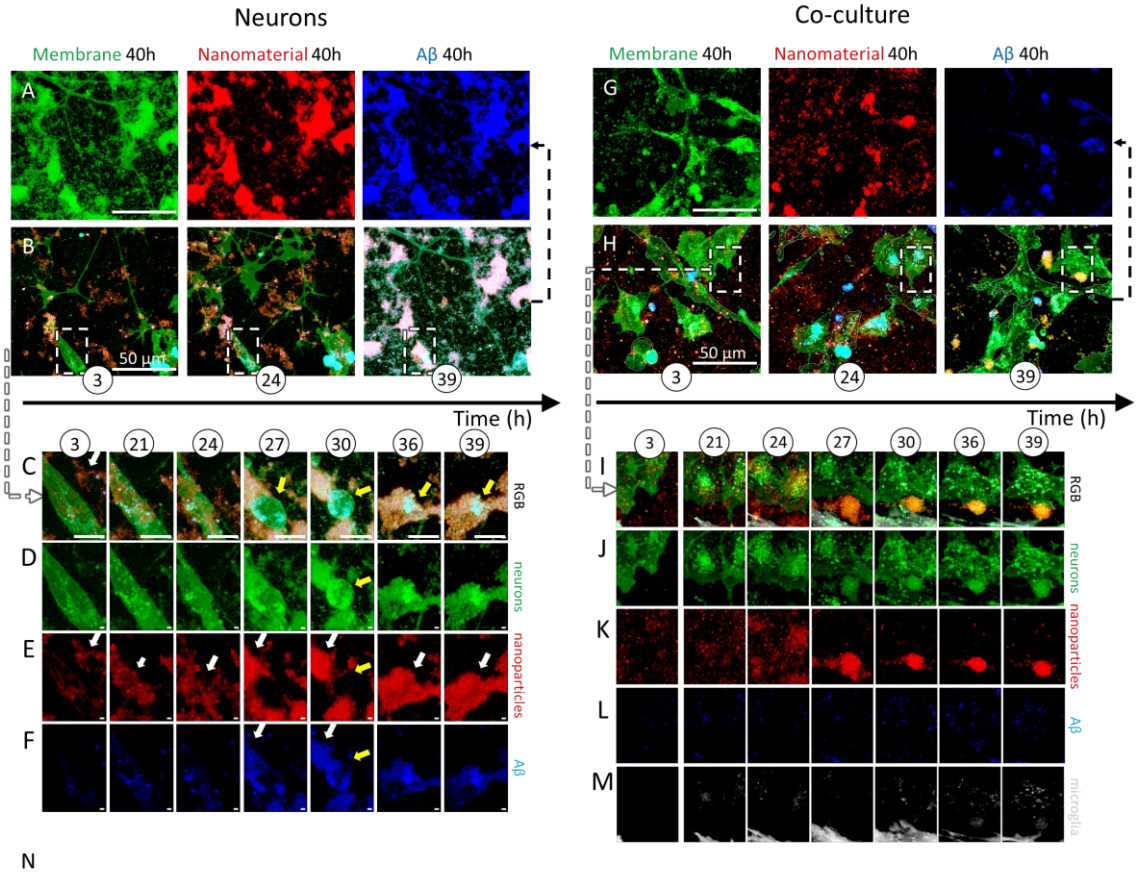

Figure 12: **Distinct formation of large Aβ plaques, axonal atrophy, and neuronal loss in neuronal monoculture contrasted by absence of the same events in microglia co-culture**. A) The last time point of the neuronal monoculture time-lapse after exposure to a 10:1 surface dose of TiO_2 nanotubes. Decomposed three channels, represented by green, red, and blue colours, correspond to log-transformed intensities of the fluorescent plasma membrane label, TiO2 nanotube scattering, and anti- Aβ antibody fluorescent signals, respectively, and B) RGB overlays of these channels at time point 3, 24 and 39 hours after exposure, C) time evolution of events detected in the dash-square

marked zoom-ins from B) image, with D) green plasma membrane, E) red TiO_2 nanotube scattering, and F) blue Aβ fluorescent signal. G) The last time point of the co-culture time-lapse after the exposure to 10:1 surface dose of TiO_2 nanotubes, with the same three channels as before, H) RGB overlays of these channels at time point 3, 24 and 39 hours after exposure. I) a time evolution of events detected in the dash-square marked zoom-ins from H) image, with J) green plasma membrane fluorescence, K) red TiO_2 nanotube scattering, L) blue Aβ fluorescence, and M) microglia cytoplasmic fluorescence.

To deepen our understanding of the processes underlying this initial experimental overview, we conducted a more detailed examination of the events that could potentially coincide with the initial formation of plaques within individual neurons, both in monoculture and co-culture (Figure 12C-F and Figure 12I-K). This examination encompassed the tracking of neuronal and microglial surface area to assess their survival, the exchange of materials between these compartments, and the quantification of Aβ - plaque sizes. Aβ plaques were identified as objects with co-localized Aβ and nanotube signals. We represented the size of Aβ plaques by plotting the cumulative anti-Aβ antibody fluorescent intensity within these objects. In the following section, we will provide a detailed account of the chronological sequence of events surrounding the formation of Aβ plaques, axonal atrophy, and neuronal loss—central events in AD, as observed in our study.

Examination of fluorescent micrographs revealed a gradual and consistent uptake of TiO_2 nanotubes by monoculture neurons over the initial 24 hours. This uptake is evident from the progressive increase in red signal intensity, indicated by white arrows, within neurons between 3 and 24 hours in monoculture (Figure 12C and Figure 12E). As a result, a slight aggregation of material occurred within these neurons. In contrast, co-culture neurons demonstrated a lower degree of nanotube uptake within the same period. This trend was further confirmed through the analysis of nanotube uptake by neurons across all ROIs for each time point (Figure 13C). Interestingly, the signal intensity of Aβ within monoculture neurons (Figure 12F) and the size of Aβ plaques changed very little (Figure 13A-B, black lines) in this timeframe.

Not long after, monoculture neurons strongly increased their uptake of nanotubes (Figure 12E and Figure 13C, red line from 20 hours onwards). At the peak of the uptake, occurring between 27 and 30 hours, we observe formation of larger structures filled with nanotube, membrane and Aβ signal in Figure 12C-F (co-localization of red, green, and blue colour plaques within neurons). This trend was observed across the whole population of neurons in monoculture sample in this period, as indicated by the exponential increase of the Aβ-plaque size after 27 hours in Figure 13A (all monoculture images can be viewed in Figure S24-S34). These were the earliest Aβ plaques that we observed, and they were typically contained within neurons.

In comparison to the continuously growing plaques in monoculture, co-culture plaques achieved their maximum size by the 30-hour mark, soon after they formed (Figure 13B). Not only were these plaques more compact in the co-culture setting, but they also displayed a distinct rounded morphology (Figure 12G-H), unlike those in monoculture neurons (Figure 12A-B). Interestingly, microglia (grey) often positioned themselves in proximity to these newly formed compact and round plaques, as exemplified in Figure 12I and Figure 12M (all co-culture images can be viewed in Figure S20-S30).

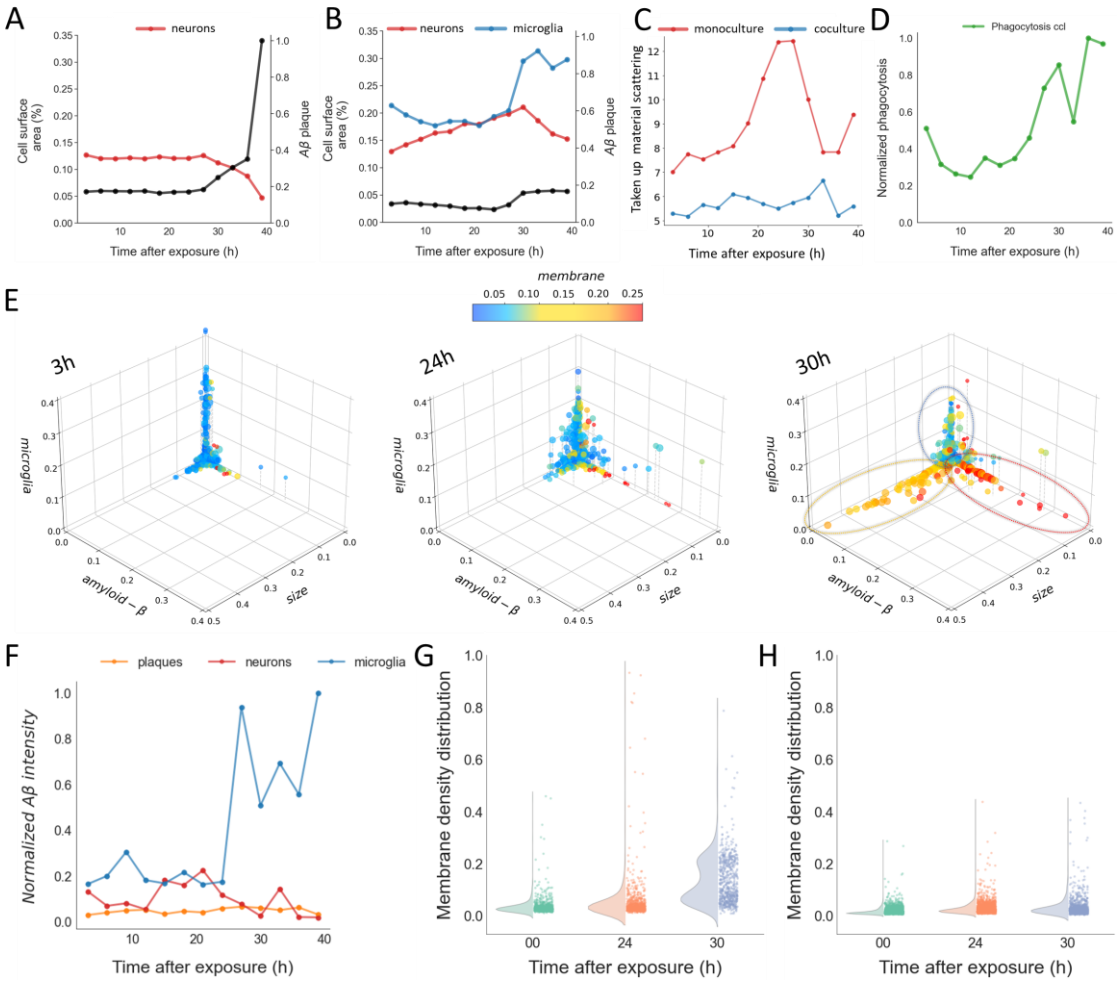

Figure 13: **Analysis of various parameters reveals the crucial role of microglia in mitigating late-stage events associated with Alzheimer's disease: insights from long-term time-lapse imaging of neuronal monoculture and co-culture with microglia**. A) Surface area of neurons in monoculture normalized to the surface are of FOV (red line) and the size of Aβ plaques as anti- Aβ antibody fluorescent intensity within the plaque mask (black line), B) surface area of neurons (red line) and microglia (blue line) in co-culture, and the size of Aβ plaques (black line), C) nanomaterial scattering intensity within the neuron mask in monoculture (red line) and co-culture (blue line), D) phagocytosis of nanomaterial defined as the nanomaterial scattering intensity within microglia mask, normalized to its maximal value, E) 4D scatter plots analysing multiple parameters for individual plaques at each time point (3-39). The diameter in µm is plotted on the y-axis, densities of Aβ on the x-axis, cytoplasmic microglia signal on the z-axis, and membrane density is color-coded according to the scale. Values of all parameters were normalized to the maximal values in monoculture. Red, yellow, and blue ellipses at the last time point identify three subpopulations of plaques: 1) small plaques with very high density of Aβ and membrane but no microglial cytoplasmic signal, 2) large plaques with low Aβ and moderate membrane density without microglia signal, and 3) small plaques with high microglia cytoplasmic density and low membrane and Aβ densities, respectively; F) integral

of Aβ fluorescent signal intensity within the microglia (blue line), neurons(red line), and plaques (yellow line) mask in the co-culture, G) distribution of membrane fluorescence signal densities within all individual plaques for time point 0, 24 and 30 hours after exposure in monoculture, normalized to the maximal values, and H) distribution of membrane fluorescence signal densities within all individual plaques for time points 0, 24, and 30 hours after exposure in the co-culture, normalized to the maximal values in monoculture.

As this sequence of events unfolded, monoculture neurons began to exhibit a distinctive rounding-up phenomenon (Figure 12C, from 27 hours onward, marked with yellow arrows), accompanied by a reduction in their surface area (Figure 13A, red line) and the extrusion of Aβ-rich plaques from within cells. Plaque externalization is evident in Figure 12C, where large structures with co-localized red, green and blue signal were gradually exiting the rounding-up neurons starting at 27 hours.

During the course of their rounding and shrinking, neurons brought the plaques even closer together, resulting in the formation of larger structures measuring several dozen micrometres in diameter. These structures were replete with Aβ, membrane components, and TiO_2 nanotubes (Figure 12C-F, 36-39 hours and Figure 13A). Concurrently, we noted a nearly complete loss of neurons, evidenced by a marked reduction in their surface area (Figure 13A).

Plaque externalization was also apparent in co-culture neurons. However, in contrast to monoculture, there was no observable rounding-up of neurons, and their surface area did not exhibit a decrease (Figure 13B, red line). Instead, neurons in co-culture increased their surface area, suggesting cellular growth. Furthermore, even after 40 hours, these neurons still had intact axonal connections with neighbouring neurons (Figure 12H, Figure S28A and M8-2).

Overall, the divergence between monoculture and co-culture became apparent around the time of plaque formation. In monoculture, neurons developed large, continuously growing extracellular plaques rich in nanotubes, Aβ, and membrane components. In contrast, co-culture neurons exhibited a distinct pattern, giving rise to small, rounded plaques with a comparatively lower biological material content. However, the most important distinction is that co-culture neurons remain viable with axons connected to neighbouring cells after 40 hours of incubation with nanotubes.

Given this intriguing contrast, our focus shifted to a detailed exploration of the events surrounding plaque formation. It became evident through repeated observations that all emerging plaques following incubation with TiO_2 nanotubes contained this material (Figure 11 and Figure 12). This prompted us to perform a single-object segmentation of individual TiO_2 aggregates from mono-and co-culture and quantify the densities of the key components we have discussed thus far. Specifically, we quantified the densities of Aβ, membrane, and microglia cytoplasmic signals within approximately 1500 identified objects for each time point, aiming to evaluate the dynamic changes in plaque composition over time. With this analysis, we aim to gain insights into the intricate processes underlying the formation of these plaques, shedding light on the distinctive responses of neurons and the potential influence of microglia in this context.

Obtained results were plotted in the 4-dimensional scatter plot in Figure 13E. Individual plaque diameter was plotted on the y-axis, Aβ density on the x-axis, cytoplasmic microglia signal density on the z-axis, and membrane density was indicated by the colour of spheres according to the colour scale. All values were normalized relative to the maximal parameters observed in monoculture. We revealed that three distinct populations of plaques formed after 39 hours of incubation with TiO_2. We discern them as 1) small plaques with a very high density of Aβ and membrane but no microglial cytoplasmic signal (red ellipse), 2) large plaques with low Aβ and moderate membrane density without microglia signal (yellow ellipse), and 3) small plaques with high microglia cytoplasmic density and low density of membrane and Aβ signals (blue ellipse).

These descriptors resemble the plaque characteristics observed *in vivo*. For example, in AD mice with suppressed microglial phagocytosis, larger plaques were observed compared to mice with normal microglial function [62]. We detected a similar size difference between the large, microglia-devoid (yellow-ellipse) and the smaller, microglia-rich (blue-ellipse) population of plaques. In another study, microglia-devoid AD mice that received microglia transplantation from healthy mice exhibited more compact plaques compared to mice without microglia engraftment [93]. Also, our study offers additional congruence with this research, as we found that plaques in the presence of microglia were not only smaller but displayed a more spherical morphology as well (Figure 12G-K). Another intriguing parallel with the same study can be drawn from a total plaque count that did not vary much between the two groups of mice, which we also noted, as the difference in plaque count between the co-culture and monoculture was less than 30%, with a higher number of plaques observed in the co-culture setting (Figure S29).

Upon further analysis, we found that monoculture plaque sizes after 40 hours exhibited a maximal diameter slightly exceeding 14 µm (Figure S29), corresponding to a surface area of approximately 500 $µm^2$. These surface areas are consistent with plaques observed in human AD patients, as reported by Serrano-Pozo et al. [104]. Interestingly, the maximal surface area in monoculture was again observed to be an order of magnitude larger as in our previous experiment with the monoculture (Figure 11G and Figure S29).

Furthermore, in AD mice with suppressed microglia, neurons exhibited increased axonal atrophy around large plaques compared to mice with functional microglia [93]. While we did not directly analyse axonal atrophy in this experiment, we observed an increase in Aβ and membrane density within plaques and these events were correlated with axonal damage in this work (Figure 8A-B and Figure 12A-B). Moreover, a significant loss of neurons was evident in monoculture conditions, a phenomenon absent in co-culture with microglia (Figure 13A-B). For that reason, we suggest that the Aβ and membrane density within the plaques can be used as proxy for damage occurring on both axons and neurons.

When we examined the temporal dynamics of components within plaques more closely, we learned that the density of Aβ increased already within 6 hours (Movie M13E), making it the first parameter to change in response to exposure to TiO2 nanotubes. Subsequently, there was an increase in membrane density after 24 hours, coinciding with the emergence of plaques characterized by large sizes and moderate membrane densities (yellow-ellipse population in Figure 13). Similarly, in patients that exhibit symptoms of AD, small Aβ -rich plaques are first to occur, acting as seeds for tau, leading to the formation of larger aggregates containing both of these proteins [22], [29], and various other neuronal proteins besides [12], [101], [102]. Therefore, we propose that the initial occurrence of small Aβ -rich plaques stems from neuronal damage, triggering the release of this protein, as discussed

before (Figure 8A-C, Figure 12, Figure S24-S34, Movie MS7-3). It is believed that this also happens in brains of patients with the brain trauma, where increased concentrations of Aβ have been reported, resembling the brains of AD patients [87]. With the progression of neuronal damage, tau may dislocate from damaged axons and accumulate extracellularly, binding to Aβ . This could clarify the prevalence of tau in larger plaques in our previous experiment (Figure 11F). Furthermore, it may explain why axonal demyelination takes place prior to the appearance of Aβ plaques and tau neurofibrillary tangles [105] as axons remain protected by the myelin sheath, acting as a shield and delaying detrimental processes caused by the external factors. Moreover, amyloid disease-associated microglia were observed to ignore Aβ plaques in favour of damaged myelin [106], suggesting that Aβ is likely a consequence of damage, rather than its cause, because it would activate the immune system otherwise.

Physical damage to neuronal plasma membrane causes the release of Aβ, normally contained within membranes [14], [15], which likely leads to the release of other membrane constituents, including phospholipids. Our analysis of per-plaque membrane density distribution supports this notion. Specifically, plaques with high membrane density emerged only in monoculture at later time points (Figure 13G), coinciding with the neuronal loss. This increase resulted in the bimodal distribution of per-plaque membrane density, indicating two distinct plaque populations existed (Figure 13G). The first had the same membrane density distribution as plaques between 3 and 30 hours, where system was still mostly unperturbed. However, the second population formed only after neuronal loss commenced, potentially representing a population of plaques that were involved in damaging processes that led to neuronal demise. Consequently, these plaques became laden with membranes and other components of dead neurons. In contrast, in co-culture, where neuronal loss was minimal, a per-plaque membrane density distribution remained constant through the experiment, and similar to those of earlier plaques in monoculture (Figure 13H and G, respectively), further emphasizing the protective role of microglia and their influence on the plaque composition and neuronal health.

Upon investigating interactions between microglia and neurons, it became evident that the flow of TiO_2 nanotubes was directed from neurons to microglia, likely due to phagocytosis from the laden cells (Figure 13D), consistent with our previous observations (Figure 9F and Figure 10). Furthermore, the analyses of Aβ density within microglia, Aβ plaques and neurons in the co-culture revealed comparable initial mean Aβ densities until 24 hours. At that time, Aβ density within microglia surged compared to the other two compartments (Figure 13F), coinciding with the increased phagocytosis of TiO_2 nanotubes from neurons (Figure 13D). Hence, we hypothesize that surge of TiO_2 and Aβ within microglia indicates the phagocytosis of early plaques that initiated damaging processes of axons and neurons. Similar to Edwards, in his extensive review paper [25], we argue that this phagocytosis of premature plaques from neurons represented a pivotal event that protected them. In the absence of phagocytosis, neurons succumbed to the continual damaged caused by TiO_2 nanotubes within them, leading to their death and deposition of their contents in plaques. This sequence likely culminates in the formation of large structures rich in Aβ, tau, membrane components and many neuronal proteins found in the brains of AD patients [8], [15], [18], [25], [33], [34], [111], [112], [104].

Chapter 5

Conclusions

In the pursuit of shedding light on sporadic AD, our research aimed to address critical gaps in the understanding of disease development, including the lacking causality between environmental factors and AD onset. Here, we propose, for the first time, a mechanism underlying sporadic AD, induced by inhalable hazardous nanomaterial, elucidating the earliest adverse events occurring in first minutes after interaction with particles, leading to late symptoms common to human patients with already progressed AD.

In our wild-type *in vitro* model, comprising neuronal and microglial cell lines, we successfully replicated key AD hallmarks, including axonal atrophy, formation of AD plaques containing Aβ, tau and other neuronal components, culminating in neuronal death. We have demonstrated the crucial role of microglia in safeguarding neurons and preventing evolution of early pathological events into the late disease symptoms. To the best of our knowledge, such comprehensive recreation of AD-related pathology encompassing earliest and latest molecular and cellular events, combined with the protective role of microglia in multiple phases, has not been experimentally demonstrated before.

Our findings suggest that certain insoluble particles, such as TiO_2 nanotubes, interact with neuronal plasma membrane in such a way to establish a connection with the motor protein machinery within the cell. This interaction facilitates their active movement alongside transport fibres, enabling the traversal of an entire neuronal length. Intriguingly, neighbouring neurons demonstrated the ability to transfer these particles onto their axons, transporting them uninterruptedly further away from the initial neuron, thus facilitating their transport over long distances.

Deep penetration of TiO_2 nanotubes within the 3D spheroid suggested the iterative nature of this transport process. Namely, particles had to be actively transferred from margins to the spheroid's interior at almost 100 µm depth. Conservation of long-distance transport in a 3D system supports our hypothesis that some nanoparticles, which can be found in ambient air, can be transported along neuronal axons, representing the basis for long-distance particulate matter relocation from the nose to the brain. Conversely, particles, such as TiO_2 nanocubes, that are rapidly taken up by neurons, or MWCNTs, that are unable to bind to neuronal membrane, are likely to remain close to the point of entry into the body without significant relocation to distant organs.

While our study provides valuable insights into the particulate matter transport mechanisms over neuronal networks, we are aware of its limitations. Firstly, our research was primarily conducted *in vitro*, which may not fully capture the complexities of the olfactory system and the dynamic interactions between nanoparticles and various cell types within a living organism. Therefore, it will be crucial to validate our findings using animal

studies. If our proposed particulate matter transport mechanism holds true, animal inhalation studies should reveal the presence of TiO_2 nanotubes in their brains and absence of nanocubes and MWCNTs.

Secondly, our study focused only on three types of nanoparticles. It is essential to recognize that distinct types of nanoparticles may interact with neurons differently and a broader range of nanoparticles will be necessary to better understand potential mechanisms for the nose-to-brain translocation.

Based on our results, we infer that upon reaching the brain, nanoparticles could induce a cascade of pathological changes commonly observed in AD human patients. Our *in vitro* model revealed the acute axonal atrophy as one of the earliest events, occurring only minutes following the exposure with TiO_2 nanotubes. Interestingly, axon continued to deteriorate hours after the exposure. This persistence implies neuronal inability to contain the threat and prevent a widespread axonal damage that can severely disrupt neuronal communication, possibly culminating in cognitive function impairments and memory loss—two characteristic features of AD [33], [63]. Even when axons evaded acute atrophy, we observed other detrimental effects caused by nanotubes, including mitochondrial impairments, and axonal clogging that hindered or prevented axonal trafficking. Such events collectively compromise neuronal homeostasis, further contributing to the overall neuronal degeneration. In addition, super-resolution microscopy revealed a release of Aβ from delicate dendritic spines damaged by the proximal TiO_2 nanotubes. With sustained damage caused by the continuous interaction with nanoparticles, released Aβ accumulated forming structures resembling AD plaques. Furthermore, these plaques contained tau protein and other cytoplasmic components and their quantity increased sharply after neuronal death. The presence of both Aβ , tau and other neuronal cytoplasmic components within AD plaques, together with the neuronal loss, is one of the most well-known cellular markers of human AD patients [8], [15], [18], [25], [33], [34], [111], [112], [104].

The involvement of microglia emerged as a critical factor in modulation of this pathological cascade. Exposure to TiO_2 nanotubes in the presence of microglia, did not lead to dendritic spines damage in neurons and subsequent release of Aβ. Microglia actively removed hazardous nanomaterial through phagocytosis, thus protecting neurons from their harmful effects, ensuring neuronal survival. Consequently, we observe significantly smaller AD plaques compared to neuronal monoculture. These experiments support our hypothesis that a co-culture of neurons and microglia, non-genetically conditioned towards neurodegeneration, exposed to hazardous environmental nanoparticle can reproduce known hallmarks of neurodegeneration – Aβ plaques, tau deposits in plaques, axonal atrophy, and neuronal death, with microglia at least locally preventing, delaying or diminishing hallmarks of neurodegeneration.

The occurrence of large Aβ -filled plaques after exposure to exogenous TiO_2 nanotubes, and their absence in co-culture, after microglial phagocytosis of nanomaterial, leads us to a significant conclusion: Aβ , commonly implicated in AD etiology, is not a cause of the disease but rather a consequence of ongoing pathological processes, including structural damage and neuronal death. The failure of Aβ -targeting drugs in clinical trials further supports this notion. Damaging processes leading to Aβ release also preceded elevated levels of neuronal cytoplasmic components within the plaques, further implying causation. Therefore, slow but progressive structural damage of neurons might explain the heterogeneous and complex composition of plaques in AD patients. Furthermore, these damaging processes resulted in significant neuronal loss, which can be analogous to

neuronal dying in AD patients that can result in up to 30% reduction of the brain mass later in disease [45].

We suggest that structural damage of neurons combined with the failure of neuronal system to contain it, regardless of its cause, leads to neurodegeneration. While our study cannot singularly attribute AD development to inhalation of hazardous materials, it posits this as a significant risk factor contributing to the disease's onset and progression.

Appendix A – Supplementary Material

1. Translocation of Particles from the Nose to the Brain – Supplement

5.1 S1 Axonal Transport

Supplemental material for Figure 1.

Differentiated SH-SY5Y were exposed to Alexa-647-labelled TiO_2 nanotubes (red), labelled with the 1 μM CMO (green) in the media in which they grew and transferred to the stage-top incubator. Imaging was performed using a 60x magnification objective with a 1.2 numeric aperture lens, pixel size 80 nm. Images were taken in 30-second increments with the specific combinations of lasers and emission provided in Table 4.

TiO_2 nanotubes used in Figure 1 were labelled with Alexa 647. In short, the TiO_2 nanotubes were first functionalised with 3-(2-aminoethylamino) propyltrimethoxysilane (AEAPMS) in the dry toluene. The unbound AEAPMS was removed by centrifugation and repeated washing with toluene and hexane. Functionalised TiO_2 nanotubes were then dried and stored in the powder form.

For fluorescent labelling, the functionalised TiO_2 nanotubes were dispersed in 100 X diluted bicarbonate buffer using a tip sonicator. Freshly dissolved Alexa Fluor 647 NHS ester in anhydrous DMSO was added to the dispersed nanotubes and the mixture was sonicated further. The unbound dye was later removed by multiple centrifugal filtrations: first with a mixture of ethanol and diluted bicarbonate buffer, and later with diluted bicarbonate buffer. The labelled TiO_2 nanotubes were stored in diluted bicarbonate buffer at 4 °C and used within two weeks after labelling. The labelling protocol is described in detail by Kokot et al. (https://doi.org/10.1080/17435390.2021.1973607).

Table 4: Experimental setup and labels used for the tracking of TiO_2 nanotubes in Figure 1.

Label	$\lambda_{EXCITATION}$ *(nm)*	*Laser power (%)*	$\lambda_{EMISSION}$ *(nm)*
CellTracker Orange	561	1	575-625
Alexa 647	647	10	650-700

Tracking of TiO_2 nanocubes:

The exemplary for TiO_2 nanocubes tracking is provided in Figure S1. Experiment was prepared in the same way as with the TiO_2 nanotubes. The difference was that we used a 20X magnification objective with the 0.8 NA lens. Also, TiO_2 nanocubes were not fluorescently labelled. We detected them with the backscattering. Time-lapse images were acquired with the interval of 500 seconds for total of 10 hours. In the image below, we observe motion of TiO_2 nanocubes (blue trail) along the 40 μm length of axons in approximately 1 hour.

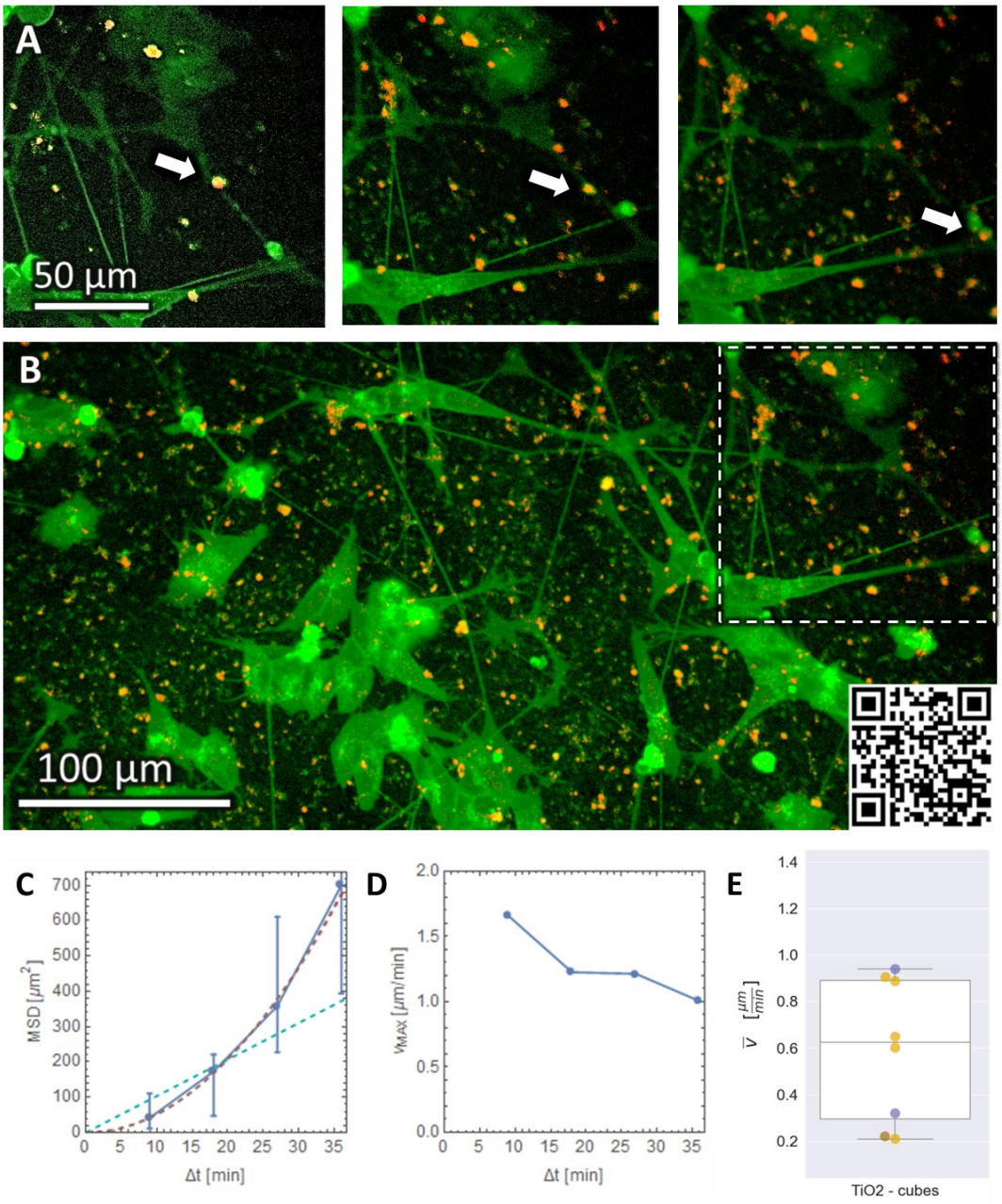

Figure S1: Active transport of TiO2 nanocubes (scattering, red) along axons of neurons labelled with the plasma membrane label (CMO, green). A) A sub-ROI where a smaller aggregate of TiO2 nanocubes moves along the axon, B) the large FOV of TiO2 nanotubes-exposed neurons. Scan the QR code in the lower right corner for the movie of the ROI with transported TiO2 nanotubes, C) a full blue line represents the fitted MSD curve obtained through the analysis of TiO2 nanotube trajectories. Exponential MSD curve fit overlaps almost perfectly with the model of directed motion (dashed red line) and not diffusion (dashed blue line), D) a maximal velocity of moving TiO2 nanocubes (µm min^{-1}) measured at 5-minute time-lag intervals during axonal transport, E) distribution of average velocities (µm min^{-1}) derived from multiple axonal transport experiments (different colours) involving TiO2 nanocubes.

In movies MS111, MS112, MS113, MS114, MS115, we demonstrate other examples of axonal transport of TiO_2 nanocubes

and axonal transport of TiO_2 nanotubes in movies MS116, MS117. All movies were acquired on 2D *in vitro* culture of differentiated SH-SY5Y neurons.

Tracking of MWCNT:

Sample preparation, exposure and imaging was conducted under the same condition as with TiO_2 nanotubes and nanocubes. The only difference between the experiments being the frame rate of acquisition, which is obvious from the timer movies MS118 and MS119. In contrast to TiO_2, we observed no motion of MWCNT particles.

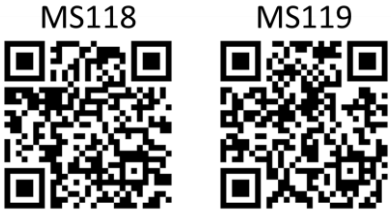

5.2 S2 Cell Hopping

5.3 S3 Transport Across the Neuronal Network

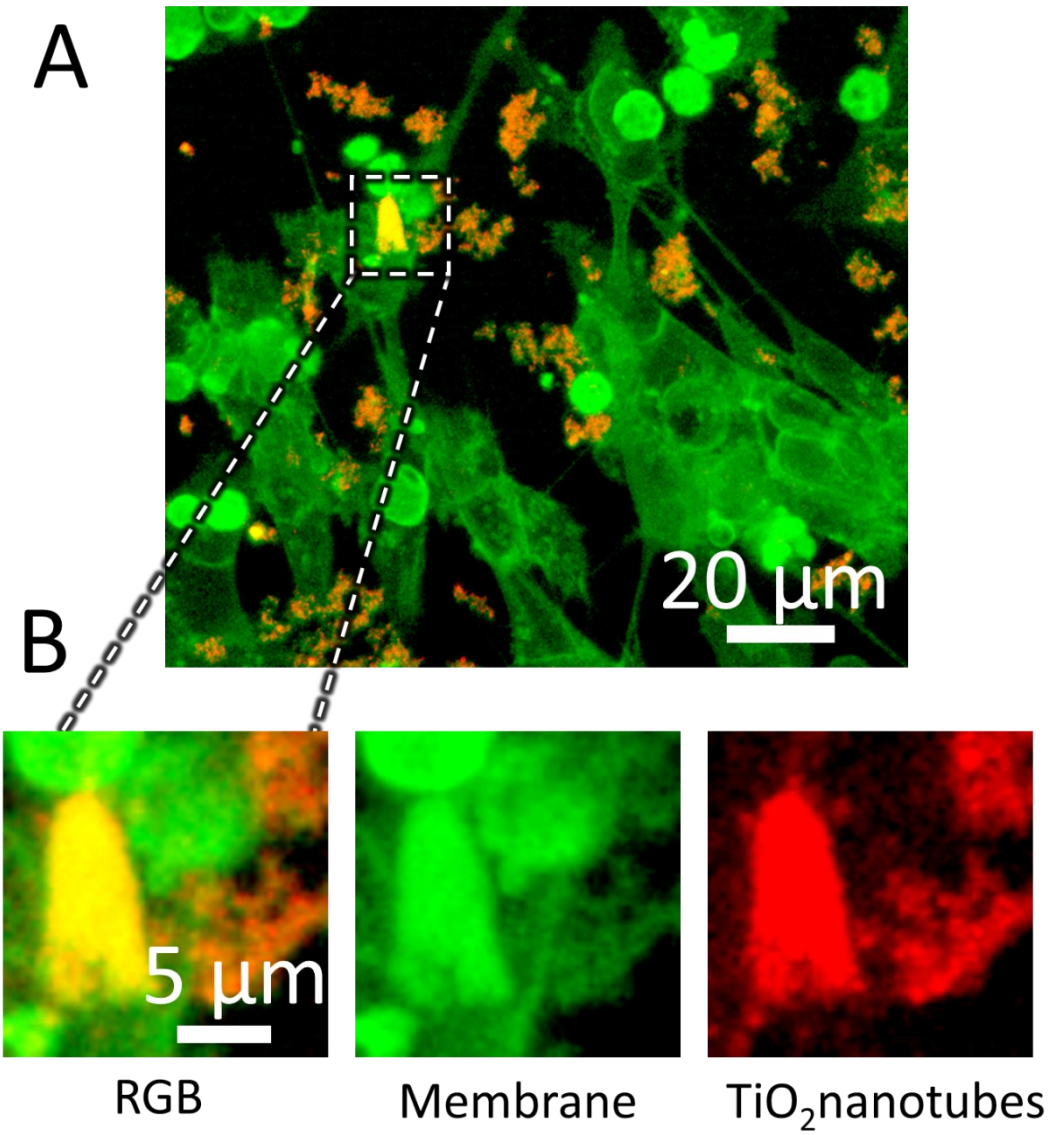

Figure S2: Co-localization of TiO2 nanotubes (scattering, red) and neuronal plasma membrane (CMO, green) already within 30 minutes after exposure. A) Large FOV of 130 x 130 µm2 and B) zoom-in to an example of co-localization of TiO2 aggregate with plasma membrane.

In Movie MS12, several TiO_2 nanotubes are "hopping" from one neuron (lower right) to another (upper right) via its axon.

MS121

This movie was acquired on 2D *in vitro* culture of differentiated SH-SY5Y neurons.

5.4 S4 The Long-Distance Transport in 3D SH-SY5Y Spheroid

Here we provide links and QR codes to AVI movies showing axonal transport at 12 – 75 μm depths of differentiated SH-SY5Y spheroid.

In Movie MS131, we provide a link to the video of experiment presented in Figure 4E-G. We have tracked a large TiO_2 nanotube aggregate 40 μm within the neuronal spheroid for ≈ 3 minutes. Within that time period, TiO_2 aggregate covered a distance of 6 μm, thereby conserving the same transport speed 0.5 μm min^{-1}, as in 2D *in vitro* system. In Movie MS132, we tracked another TiO_2 aggregate that covered a distance of 4 μm in ≈ 3 minutes, moving with the average speed of 0.45 μm min^{-1}. The last time point from this time-lapse with the trajectory marked blue can be seen in Figure S3C.

MS131 MS132

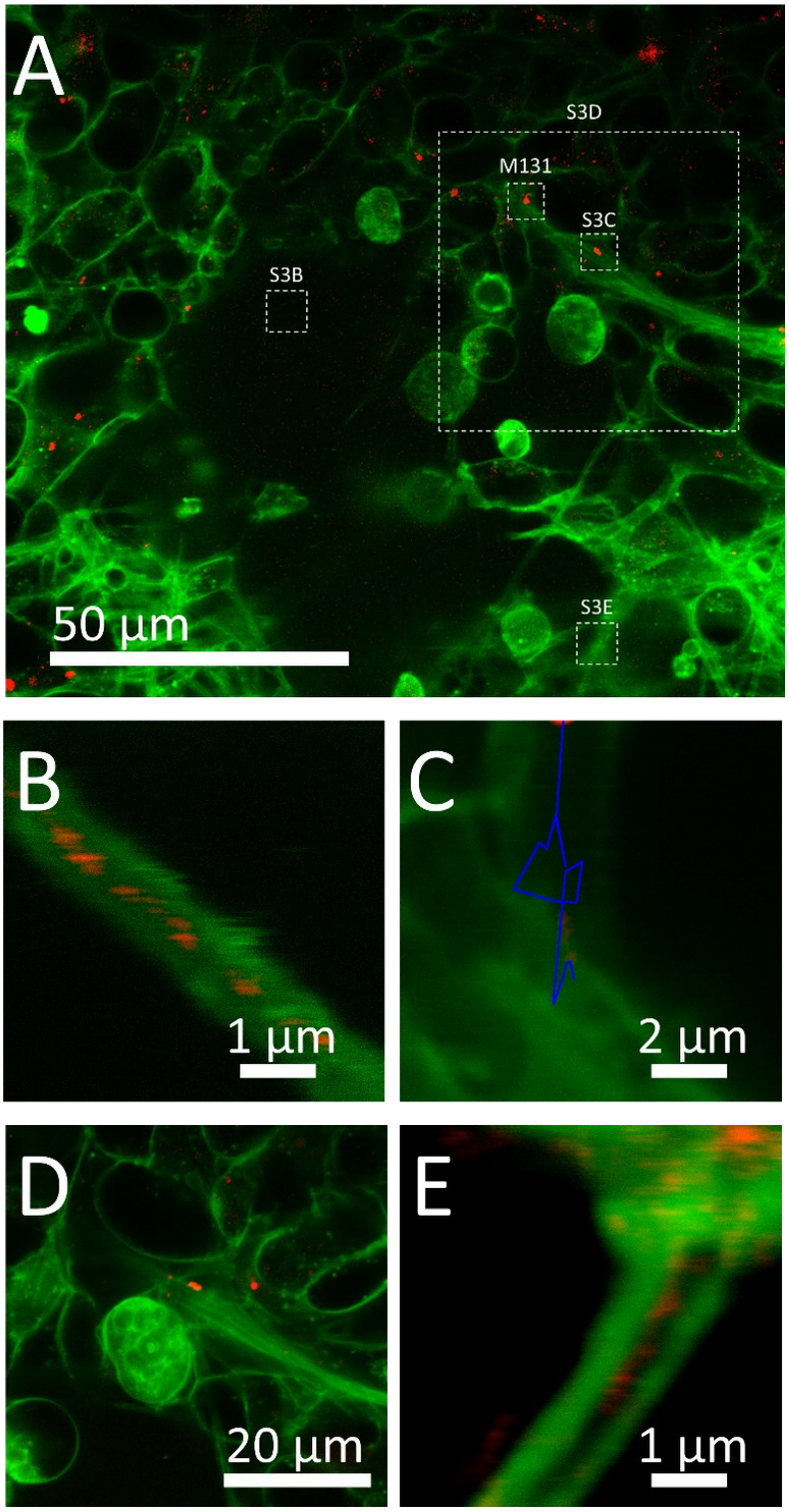

Figure S3: A section of differentiated CellMask Deep Red stained SH-SY5Y (green) spheroid at ≈ 40 µm depth exposed to TiO2 nanotubes (red) for 72 hours. A) An overview of the selected ROIs that were examined in greater detail for B) the presence of nanotubes (red) along axons of neurons (green) marked with the S3B white square, C) a blue-coloured trajectory of transported TiO2 nanotube aggregate during 5-minute-long time-lapse within

the region marked with the S3C white square, D) nanotubes localized along axonal bundles within the spheroid (S3D), and E) nanotubes localized between two individual axons (S3E).

2. Early Events in Alzheimer's Disease

5.5 S5 Axonal Atrophy

Supplement for Figure 5 of the main paper.

Here we provide links and QR codes to AVI movies showing axonal atrophy on differentiated SH-SY5Y. On all movies, neurons were labelled with the plasma membrane fluorescent label CMO (green) and were exposed to 10:1 surface dose of Alexa647-labelled TiO2 nanotubes.

Please press CTRL+click on links below to access movies:

MS151, MS152, MS153,

or scan the provided QR codes:

MS151 MS152 MS153

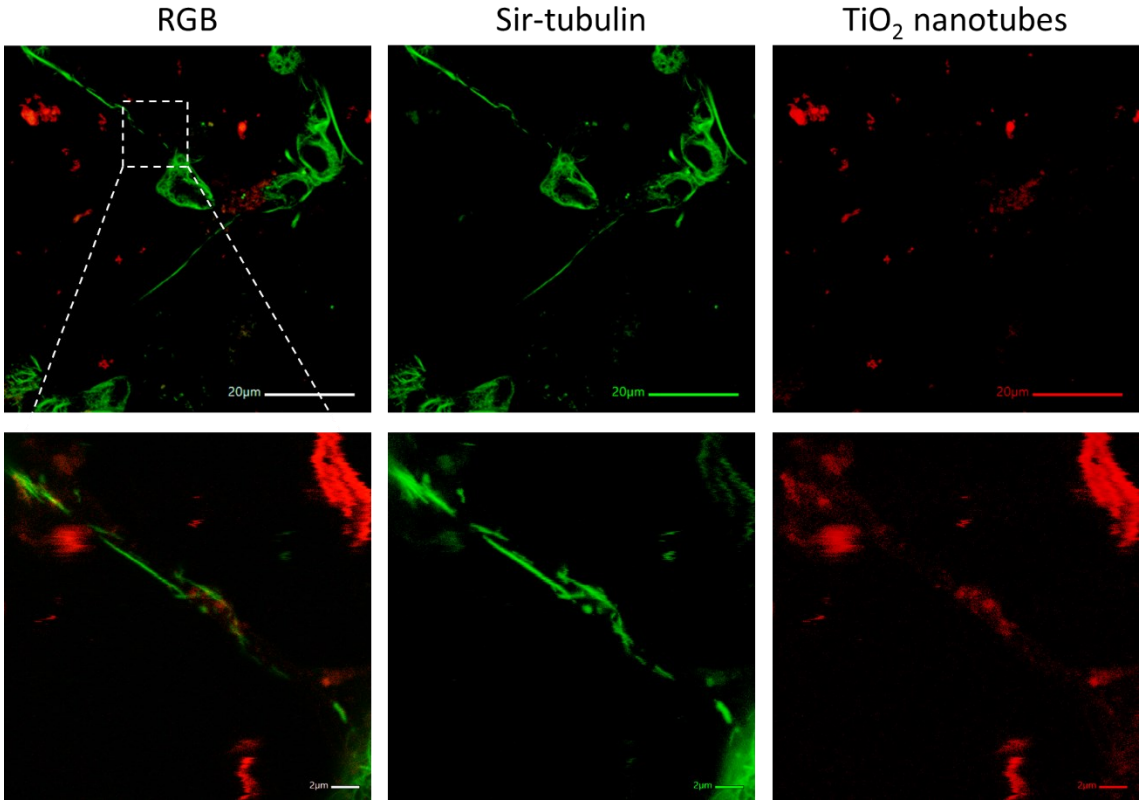

Figure S4: Axonal tubulin (green) breaks at the site of contact with Alexa647-labelled TiO2 nanotubes (red).

5.6 S6 Mitochondrial Dysfunction and Transport Impairment

Experiment presented in the main text was imaged with the following microscope setup:

Laser (nm)	*Laser power (%)*	*Pixel size (nm)*	*Time step (s)*	*Pinhole @ 650nm (μm)*
640	0.3	100	12	40
561	10			
488	20			

In time-lapse movies MS161, MS162, we present mitochondria with hindered transport through axons that were clogged, or otherwise affected, by TiO2 nanotubes. In MS161, there is a TiO2 aggregate (red) on the connection of axon with the upper neuron soma (green), blocking the transition of mitochondria (grey) from axon. Also, note the pathological axonal swelling on that spot. In MS162, mitochondria are unable to continue motion directed upward along the y-axis.

Laser (nm)	*Laser power (%)*	*Pixel size (nm)*	*Time step (s)*	*Pinhole @ 650nm (μm)*
640	0.3	100	12	40
561	10			
488	20			

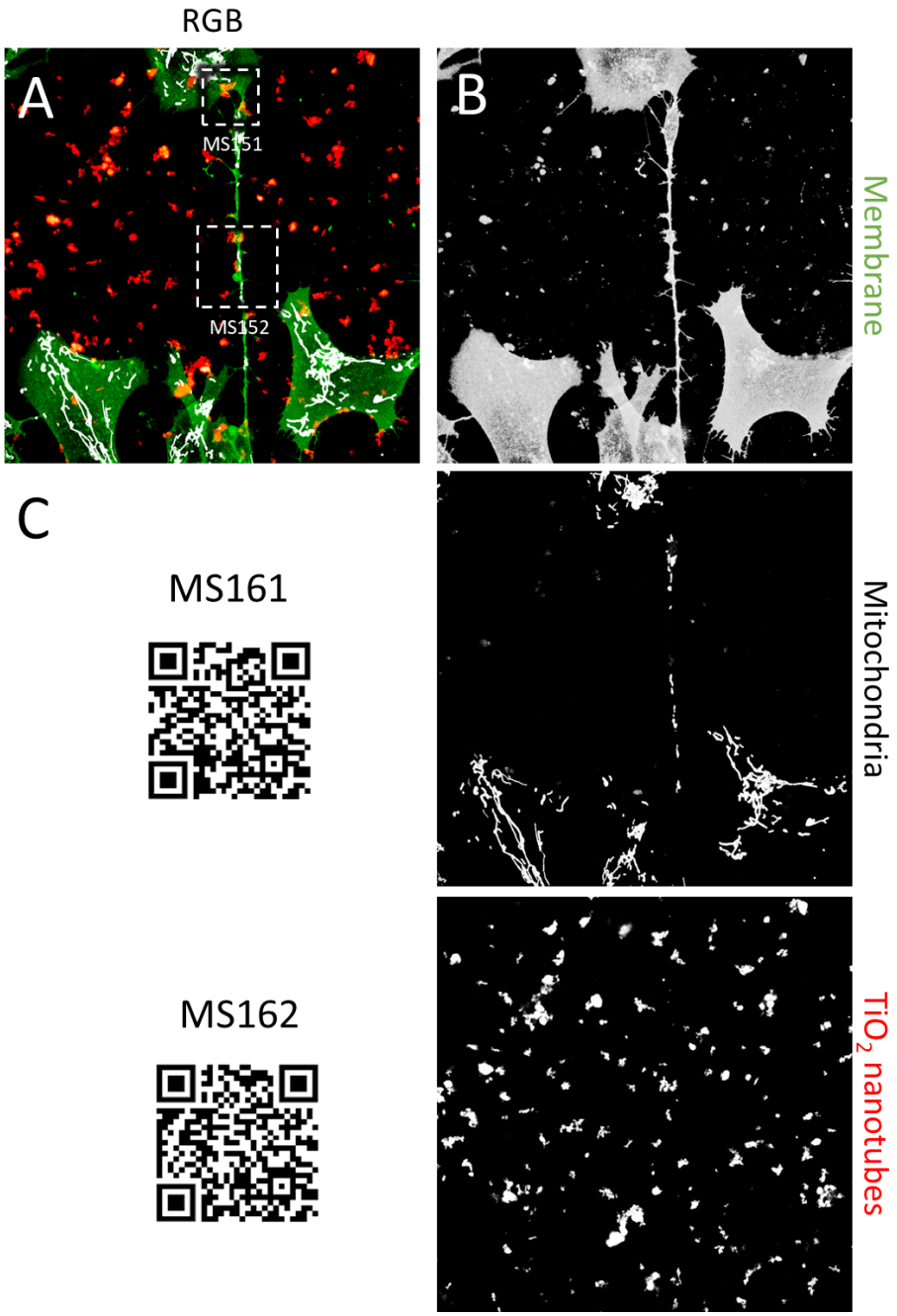

Figure S5: Blocked transport of mitochondria labelled with the MitoTracker Green (grey) within 1 hour after exposure to Alexa 647-labelled TiO2 nanotubes (red). Neurons were

labelled with the CellMask Orange (green). Because the same labels were used in all experiments regarding the mitochondria, we showed individual channels only in this image.

In time-lapse movie MS163, MS164, we show impaired mitochondrial transport in axons affected by TiO_2 nanotubes. In MS163, mitochondrion (grey) that moves from left to right remains stuck in the large TiO_2 aggregate at the middle of the axon. In MS164, a group of mitochondria moving from the lower neuron to the upper one cannot pass due to the TiO_2 aggregate that blocks the way between two cells. TiO_2 aggregates that block the way are marked with arrows in Figure S5.

Laser (nm)	*Laser power (%)*	*Pixel size (nm)*	*Time step (s)*	*Pinhole @ 650nm (µm)*
640	0.3	200	600	40
561	10			
488	30			

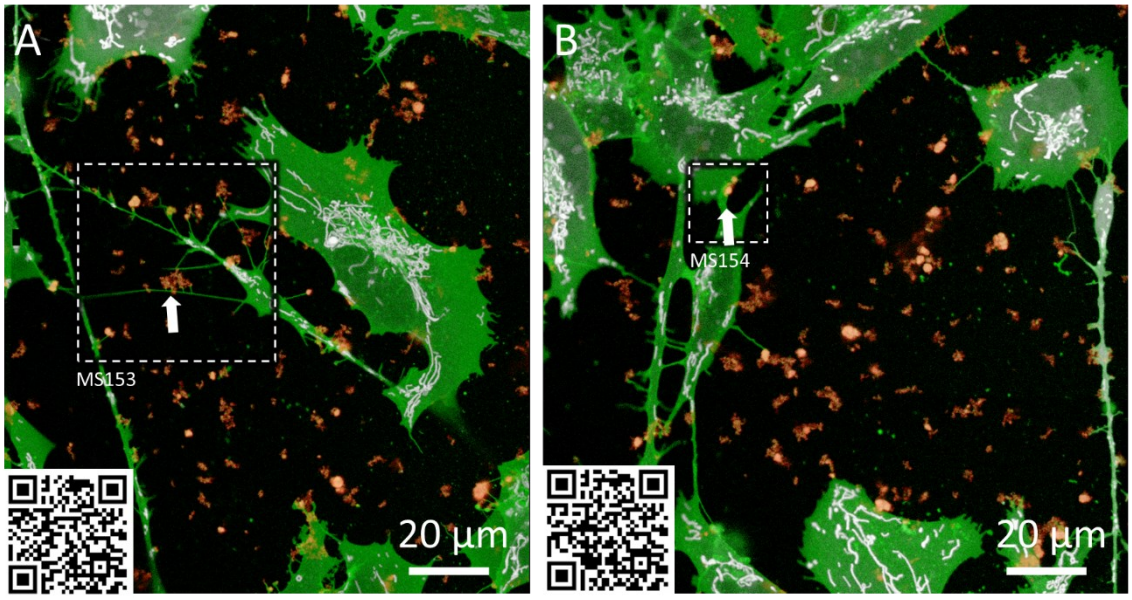

Figure S6: Blocked transport of mitochondria labelled with the MitoTracker Green 4 hours after exposure to Alexa 647-labelled TiO2 nanotubes. Neurons were labelled with the CellMask Orange.

Transport on mitochondria along axons remains impaired also 1 day after exposure to TiO_2 nanotubes. In MS165, there are mitochondria travelling to the left and right end of the axonal section. However, they cannot pass further from the area clogged by the TiO_2 aggregates.

Laser (nm)	*Laser power (%)*	*Pixel size (nm)*	*Time step (s)*	*Pinhole @ 650nm (µm)*
640	0.16	100	720	40
561	10			
488	20			

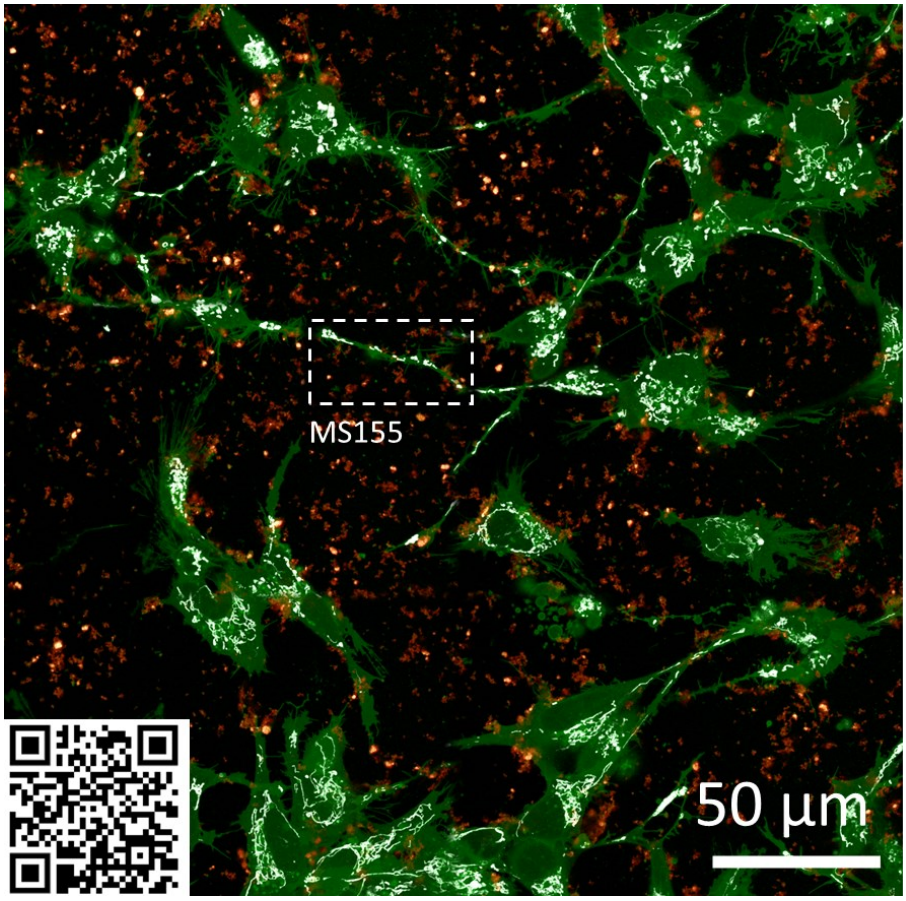

Figure S7: Blocked transport of mitochondria labelled with the MitoTracker Green after 1 day of exposure to Alexa 647-labelled TiO2 nanotubes. Neurons were labelled with the CellMask Orange.

We observed impairments in mitochondria transport already after 30 minutes after exposure to TiO_2 nanotubes. In MS166, we see that the first two mitochondria transported manage to go by the TiO_2 aggregate (white arrow in Figure S8) but the transition was not smooth. However, other mitochondria did not manage to pass or move by TiO_2. We see that the third mitochondria trying to pass the aggregate struggles from 480 s, and does not pass further. Therefore, while the transport is completely blocked in some axons, in others it is only impaired and slowed down.

Laser (nm)	*Laser power (%)*	*Pixel size (nm)*	*Time step (s)*	*Pinhole @ 650nm (µm)*

640	0.36	300	20	40
561	10			
488	30			

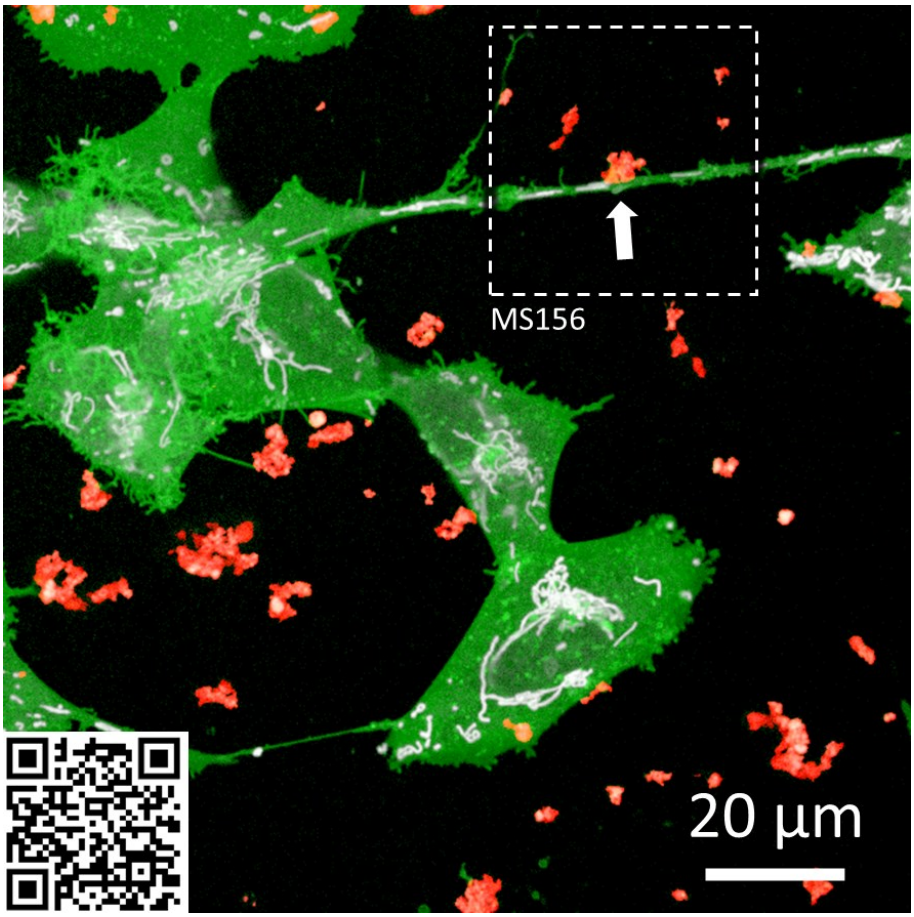

Figure S8: Blocked transport of mitochondria labelled with the MitoTracker Green after 30 minutes of exposure to Alexa 647-labelled TiO2 nanotubes. Neurons were labelled with the CellMask Orange.

In axons without TiO2, mitochondrial transport is not blocked and is normal (MS167).

5.7 S7 Arborisation Does Not Rescue Lost Axons

In Movie M71, we show a representative ROI with neurons branching their dendritic spines in the process of arborisation as a response to exposure to TiO2 nanotubes. Individual images (time point 0, 1, 8, and 28 hours) from this time lapse are shown in Figure S9.

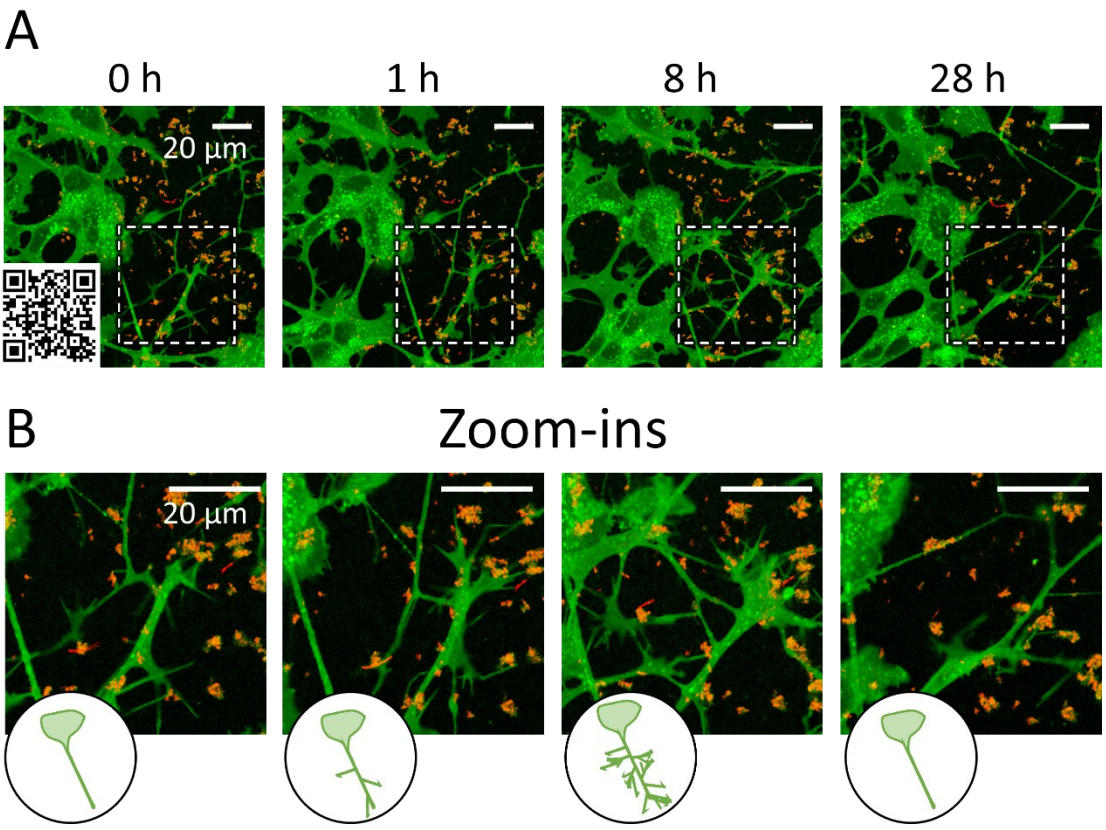

Figure S9: A transient arborisation after exposure to TiO2 nanotubes. A) Representative images of CMDR-labelled neurons (green) at time points 0, 1, 8, and 28 hours. Time point 0 h was imaged within few minutes when we transferred exposed cells from the laminar to the microscopy stage. Neurons were branching their dendritic spines from the main axonal shaft after exposure to TiO2 nanotubes. To see a movie of the whole time-lapse, please scan the QR code provided in the lower left corner of the first image. B) For easier representation, we selected areas of axons that were showing arborisation (highlighted with white dashed squares in A).

In Movies M72a, we demonstrate another instance of axonal arborisation on neurons exposed to TiO_2 nanotubes. A 63 x 63 μm^2 zoom-in of the same movie (M72b), focuses on the region where the change was largest. Neurons have exhibited most intensive arborisation within first 6 hours. Afterwards, branching drops, until it ends up in almost smooth axons.

Figure S10: QR codes with links to movies M72a and M72b.

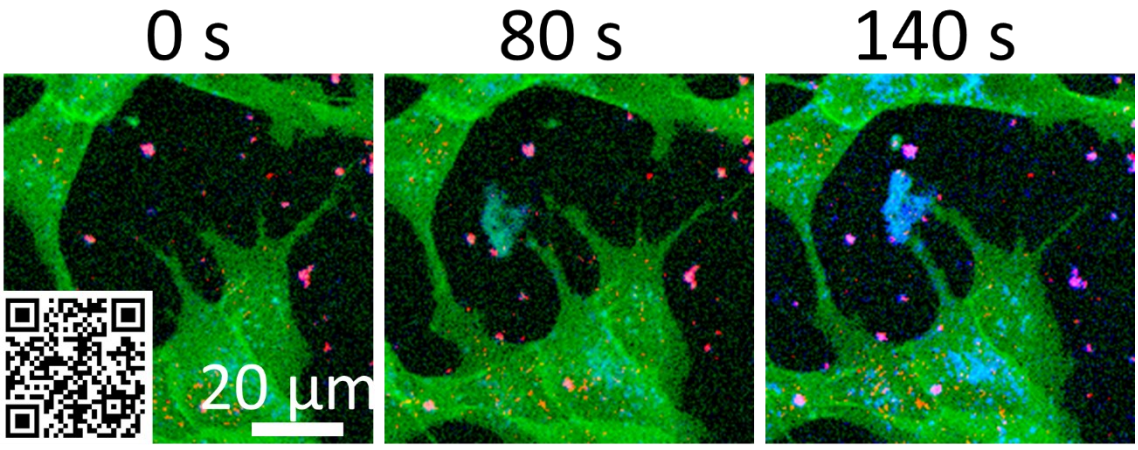

Figure S11: Release of Aβ from dendrites of neurons after exposure to TiO2 nanotubes. Aβ was labelled with the Alexa-647-labelled primary anti- Aβ antibodies (blue), neurons with the plasma membrane CMO (green), and nanotubes were detected with backscattering.

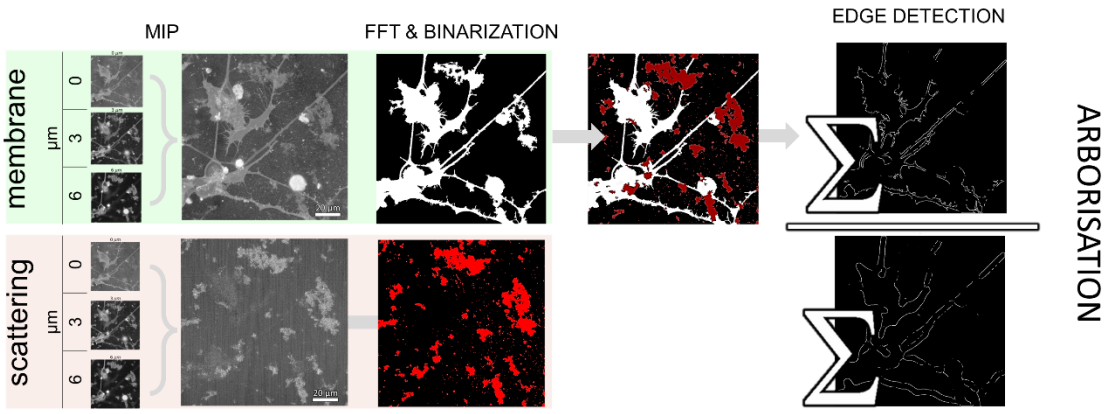

Figure S12: The algorithm for calculation of arborisation of neuronal axons presented in Figure 8. Arborisation was quantified from the plasma membrane label signal. In the first step, we generate a maximum intensity projection (MIP) along the z axis of a 3D stack for

each time point to ensure that all axons and dendrites are included in one image. Such image is thresholded and binarized. With the Canny edge detector filter we find the edges of the mask. Briefly, the peak of the derivative of a curve fitting the gradient of grey values reveals the location of the edge pixel. Iteration of the process yields edges of all objects on the image. Pixels with peak derivative value that are not connected to the edge are discarded to increase the accuracy and the thinness of detected edges. Such algorithm yields a pixel-precise edge mask that is true to the edge of neurons on an input image. We also generate another "imprecise" edge mask by applying the same algorithm on the Gaussian blurred input image to obtain the neuronal edges that lack fine dendritic spines. The magnitude of arborisation is determined as the ratio of edge length of both masks.

5.8 S8 Microglial Phagocytosis of TiO_2 Nanotubes Protects Neurons

Figure 9D – Phagocytosis

Binary masks of neurons and microglia were generated based on the differential fluorescent labelling – each cell line had its own label. Integral of TiO_2 scattering within each mask, normalized to its surface area, is a measure of the amount of material in that respective cell type. This was performed for each time point of a time lapse series. Phagocyted material is plotted as a fraction of nanomaterial in neurons and microglia.

All micrographs acquired for the analysis, results of which were plotted in Figure 10, are shown below.

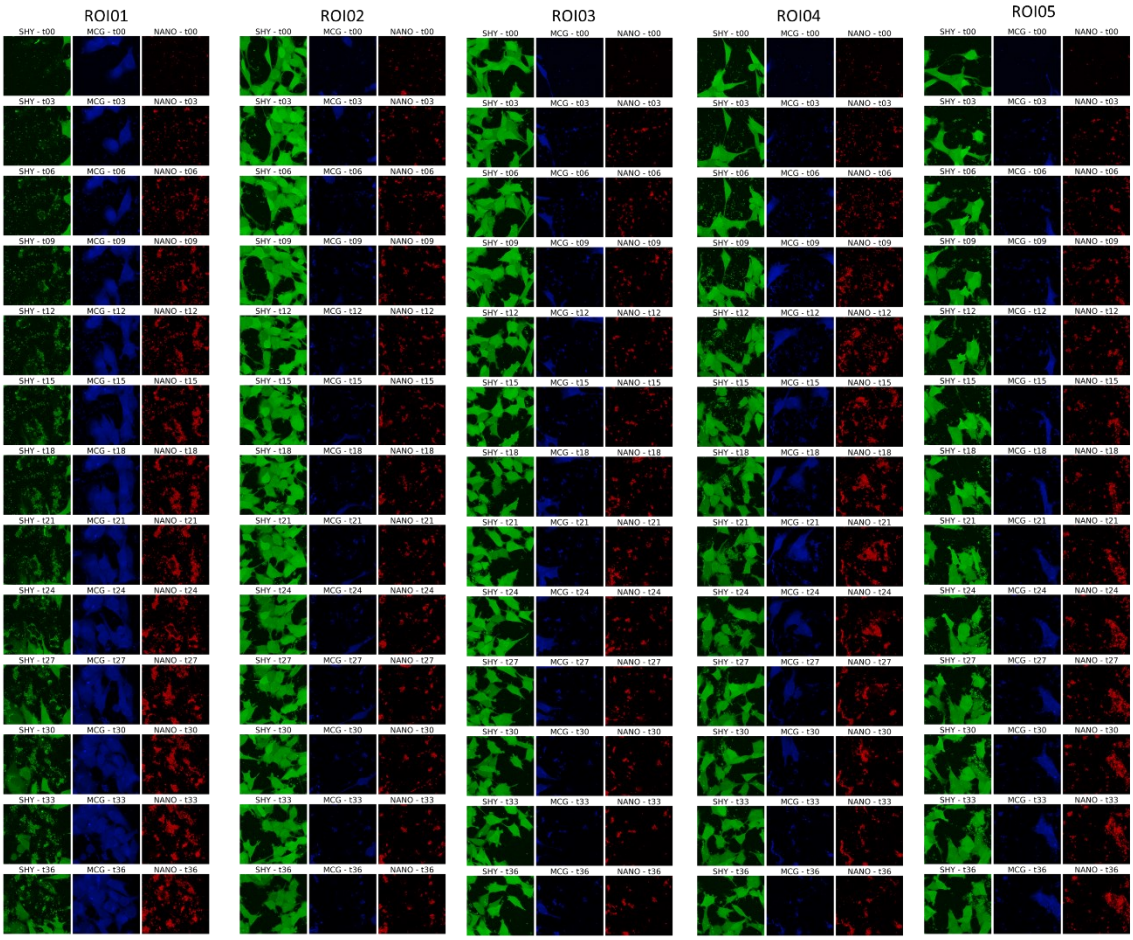

Figure S13: Images (133 x 133 μm^2) from ROIs 1-5 acquired and analysed in Figure 10 of the main text are decomposed in separate channels. Neurons are represented in green (cytoplasm label CellTracker Green), microglia in blue (cytoplasm label CytoTracker Orange), and TiO_2 nanotubes in red (backscattering) colour.

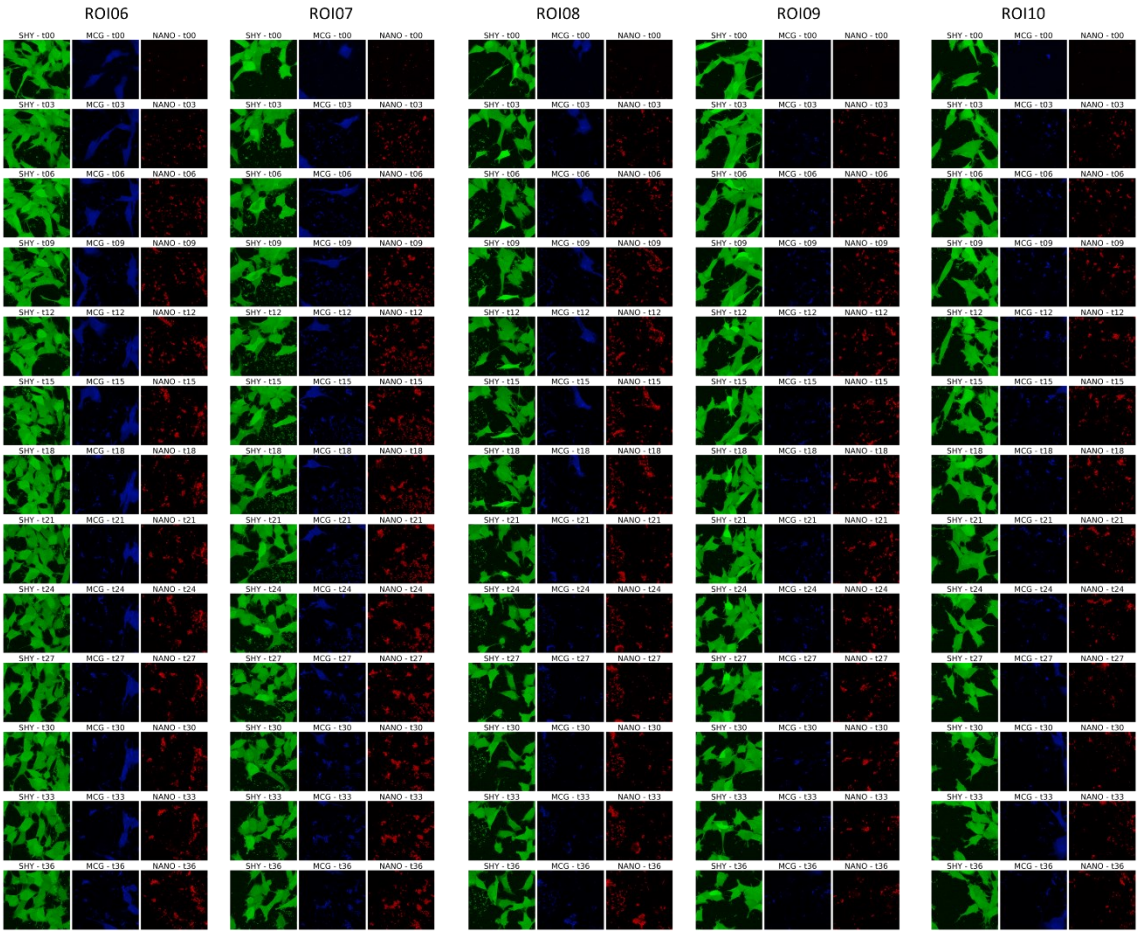

Figure S14: Images (133 x 133 μm^2) from ROIs 6-10 acquired and analysed in Figure 10 of the main text are decomposed in separate channels. Neurons are represented in green (cytoplasm label CellTracker Green), microglia in blue (cytoplasm label CytoTracker Orange), and TiO_2 nanotubes in red (backscattering) colour.

Supplemental material for the analysis plotted in Figure 10.

Samples exposed to TiO_2 were transferred to the stage top incubator and imaged for 36 hours with 3 hours increment. For each mono- and co-culture, 10 ROIs were selected, the size of each was 133x133 μm^2, and 3 z-slices were acquired at 0.3 and 6 μm height. We used the 60x magnification objective with 1.2 numeric aperture lens. The excitation/emission combinations of lasers and detectors used are laid out in Table 5 below.

The surface dose of nanoparticles added to the cells was 10:1. Within each ROI, we performed analysis involving generation of binary masks of neurons, microglia and nanomaterial. This enabled tracking of changes in neuronal and microglial surface areas, and the exchange of material between these compartments over time.

Table 5: Experimental setup for Figure 10.

Label	$\lambda_{EXCITATION}$ *(nm)*	*Laser power (%)*	$\lambda_{EMISSION}$ *(nm)*
CMDR	640	1	650-700
CMO	561	10	575-625
anti-β-Amyloid Ab	488	10	650-700
Backscattering	488	1.3	488

Pixel size was 200 nm, pinhole 1.01 AU @650 nm, and pixel dwell time 3 μs with 1 line accumulation.

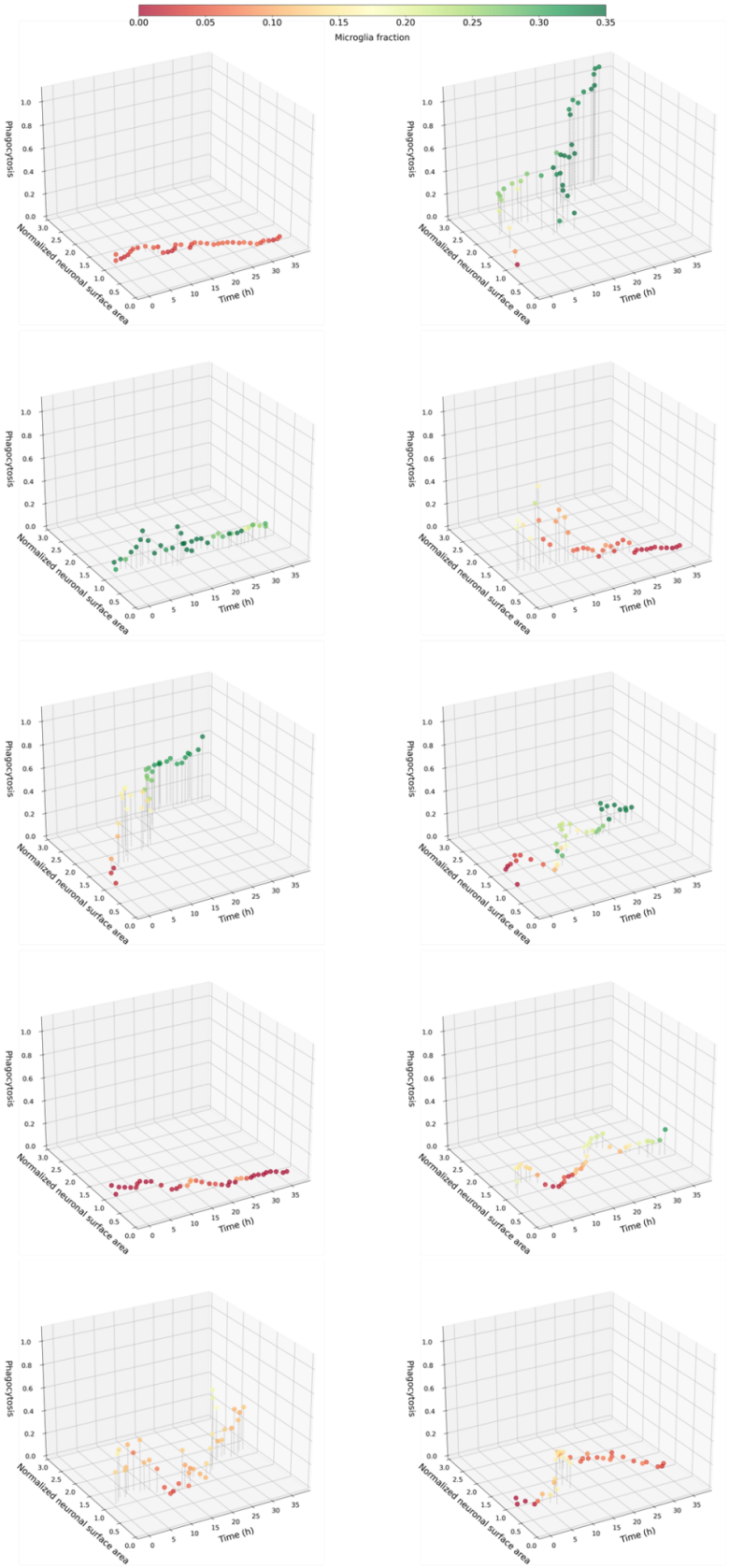

Figure S15: Results of individual ROI analysis of the data plotted in Figure 10 of the main text.

3. Recapitulating Late-Stage Alzheimer's Disease Characteristics *In Vitro*

5.9 S9 Aβ and Tau Containing Plaques

Supplement for Figure 11 of the main text.

SH-SY5Y were differentiated as described before. To visualize them (green), we used cytosolic CTG. This fluorophore emits fluorescence exclusively within the cells. Mouse monoclonal antibody against amino acids 1-40 of human amyloid β (Aβ) was used for detection of APP and Aβ (blue). White fluorescence signal was obtained using the Tau-5 mouse monoclonal antibody, against total tau protein. Both antibodies were added in 2 μg mL^{-1} concentration before imaging.

Imaging was performed using a 20x magnification objective with a 0.8 numeric aperture lens, pixel size 250 nm, and the pixel dwell time 10 μs. Specific combinations of lasers and emission filters utilized during the imaging process are provided in Table 6. A total of 15 regions of interest (ROIs), each measuring 400 x 400 μm, were scanned, resulting in the analysis of over 1000 neurons and more than 6000 plaques.

Table 6: Experimental setup and labels used for the analysis of extracellular plaque content in Figure 11.

Label	$\lambda_{EXCITATION}$ *(nm)*	*Laser power (%)*	$\lambda_{EMISSION}$ *(nm)*
anti-TAU Ab	640	10	650-700
anti-β-Amyloid Ab	488	10	650-700
CellTracker Green	488	1	505-550
Backscattering	488	0.3	488

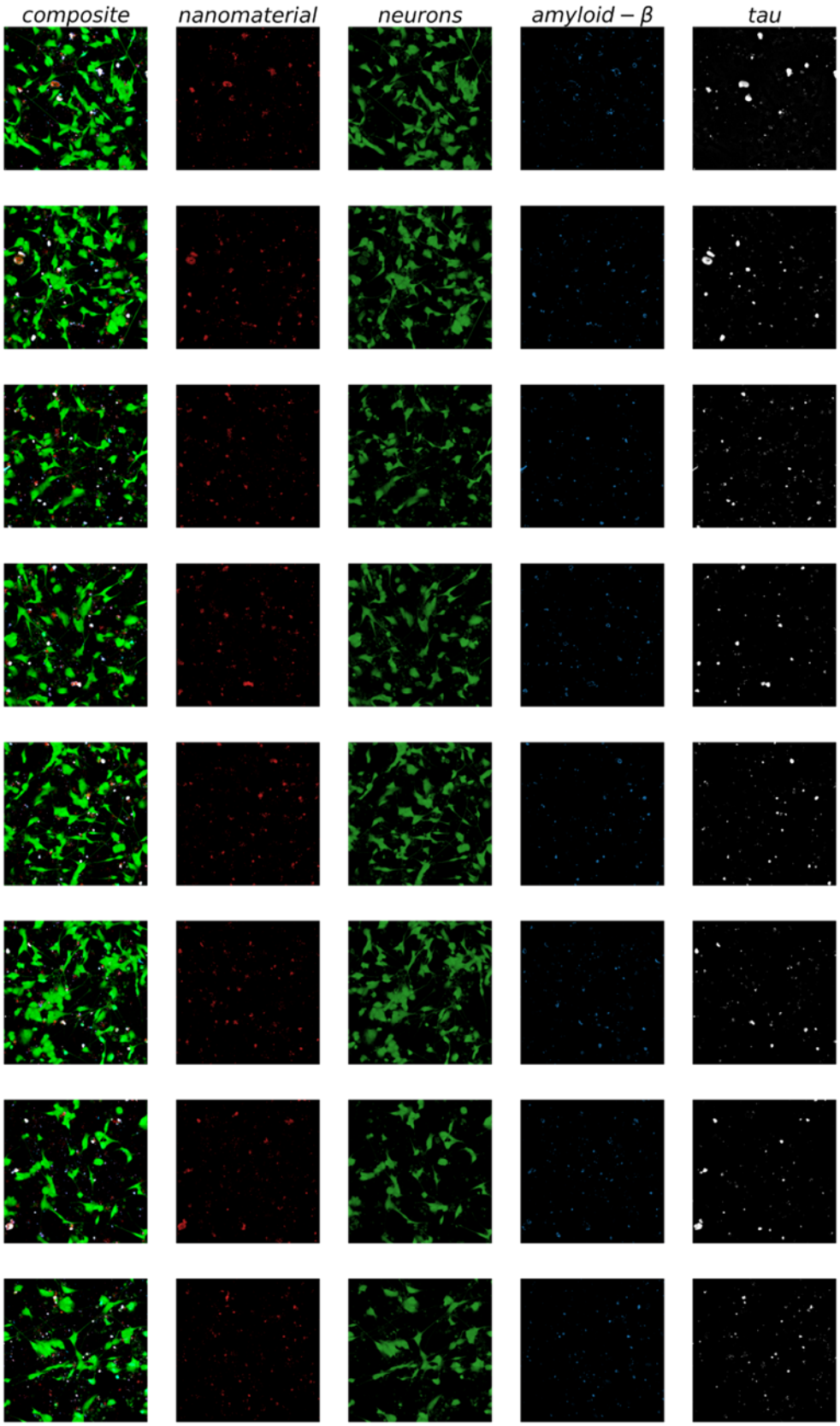

Figure S16: ROIs 1-8 analysed for the composition of TiO2-triggered Aβ plaques in Figure 11. The first column shows the RGB image, while the subsequent columns display decomposed channels representing different components. Specifically, the second column

represents the nanomaterial scattering signal (red), the third column represents the cytoplasmic CellTracker Green label (green), the fourth column represents the anti- Aβ antibody signal (blue), and the fifth column represents the anti-TAU antibody signal (gray).

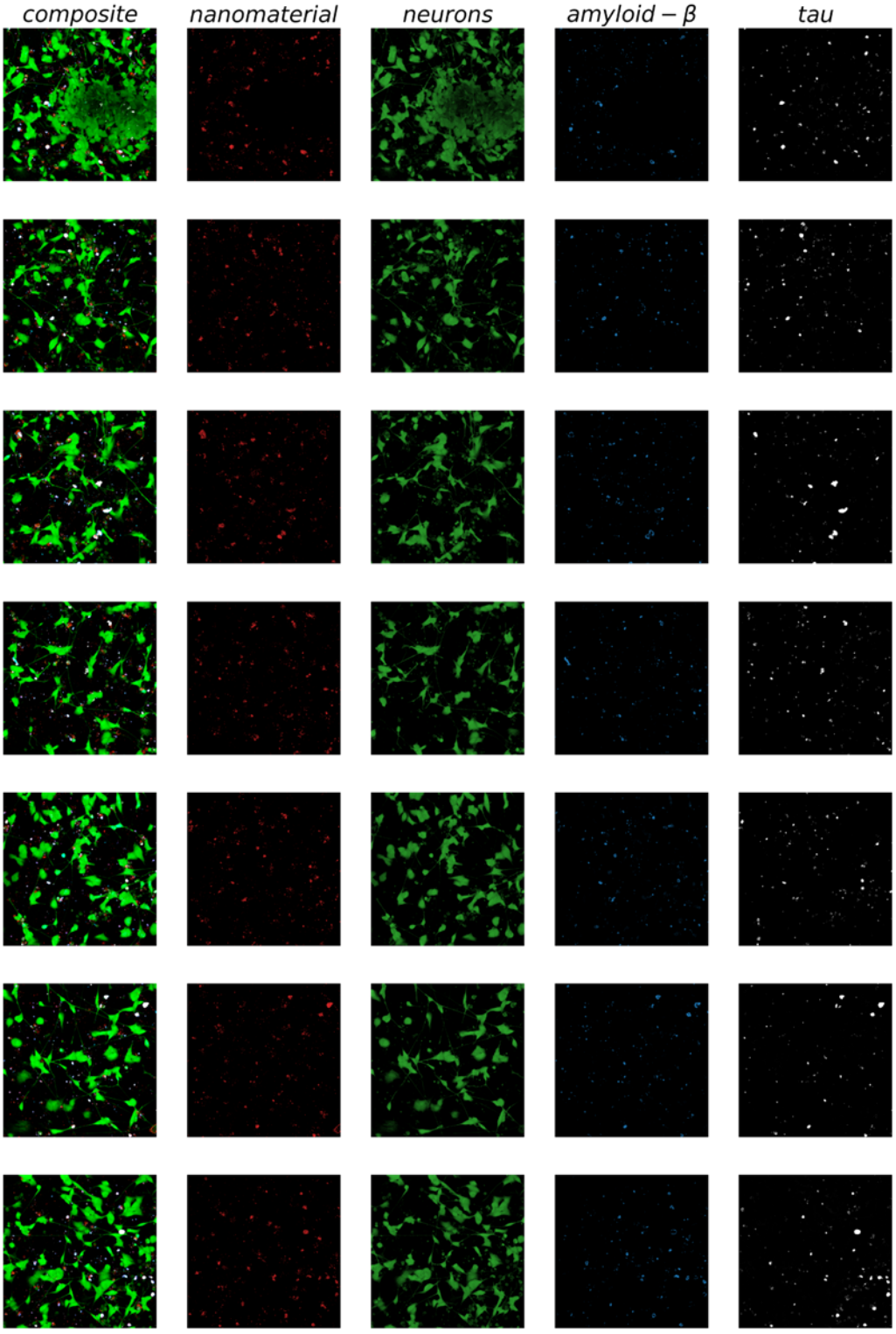

Figure S17: ROIs 9-15 analysed for the composition of TiO2-triggered Aβ plaques in Figure 11. The first column shows the RGB image, while the subsequent columns display decomposed channels representing different components. Specifically, the second column represents the nanomaterial scattering signal (red), the third column represents the cytoplasmic CellTracker Green label (green), the fourth column represents the anti- Aβ

antibody signal (blue), and the fifth column represents the anti-TAU antibody signal (gray).

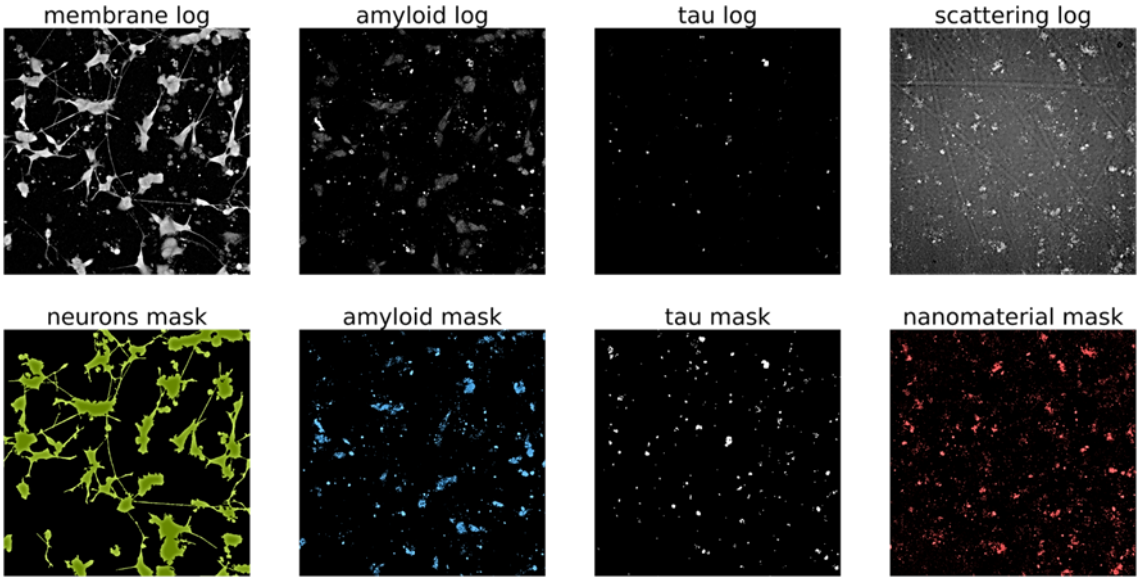

Figure S18: An example of image binarization performed on a single ROI in Figure 11. First, a Fast Fourier Transform (FFT) was applied to all log-transformed images. For the neuron mask, frequencies 2-1500 were kept. For Aβ, frequencies 1-50 were kept. For tau, frequencies 1-50 were kept. For the nanomaterial, frequencies 1-100 were kept. Afterward, reverse FFT images were thresholded to remove any remaining noise.

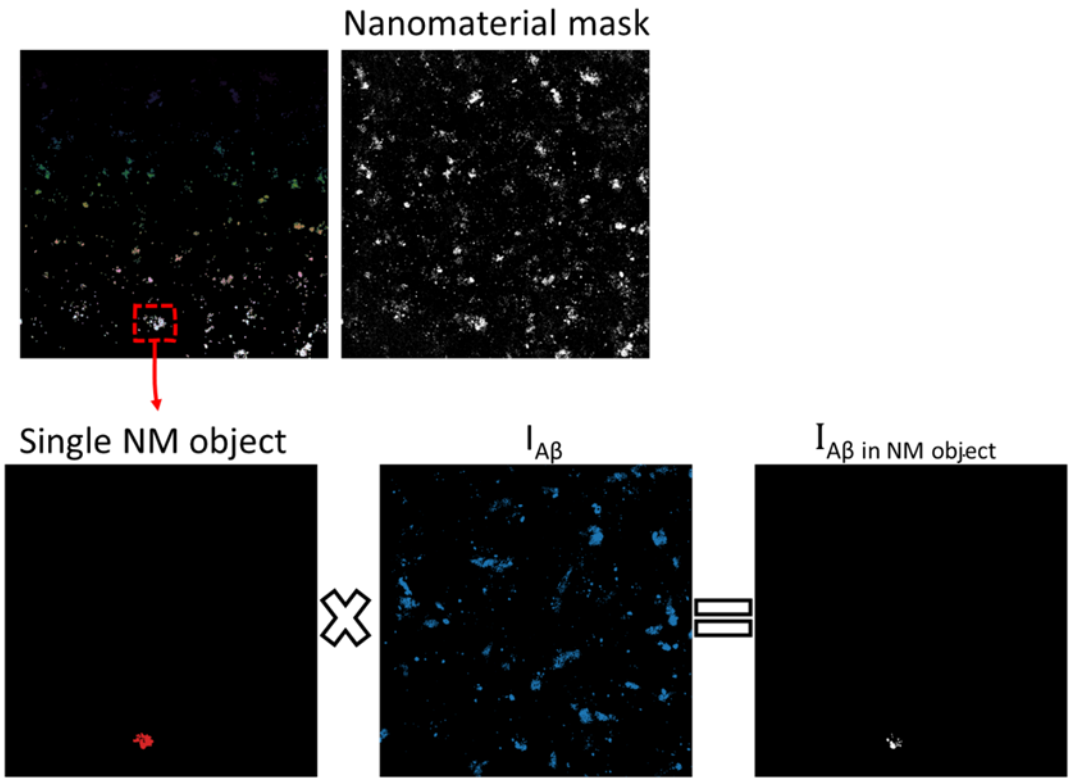

$$d_{Aβ} = \frac{\Sigma I_{Aβ\ in\ NM\ object}}{S_{NM\ object}}$$

Figure S19: Example algorithm for calculating densities of plaque components. The calculation of the Aβ density begins with the generation of a binary mask of the nanomaterial using the FFT method, as explained before. Once the mask is obtained, unique IDs are assigned to each nanomaterial object, allowing for individual analysis. Next, a loop is conducted, processing each object individually. The nanomaterial object is multiplied with the input Aβ micrograph ($I_{Aβ}$), resulting in an image displaying Aβ fluorescence exclusively within that specific nanomaterial object ($I_{Aβ}$ in NM object). The quotient of the sum of Aβ intensity within the object and the object's surface area provides the density of Aβ within that object ($d_{Aβ}$). The same algorithm is applied to the cytoplasmic and TAU signals.

5.10 S10 Microglia Mitigate Formation of Aβ Plaques

The samples were exposed to TiO_2, transferred to the stage top incubator and imaged for 40 hours with 3 hours increment. For each mono- and co-culture, 15 ROIs were selected, the size of each was 133x133 µm, and 3 z-slices were acquired at 0.3 and 6 µm height.

Images were acquired with the 60x magnification objective and 1.2 numeric aperture lens. The excitation/emission combinations of lasers and detectors used are laid out in Table 7.

Table 7: Experimental setup for images in Figure 13.

Label	$\lambda_{EXCITATION}$ *(nm)*	*Laser power (%)*	$\lambda_{EMISSION}$ *(nm)*
CMDR	640	1	650-700
CMO	561	10	575-625
anti-β-Amyloid Ab	488	10	650-700
Backscattering	488	1.3	488

Pixel size was 250 nm, pinhole 1.01 AU @650 nm, and pixel dwell time 4 µs with 1 line accumulation. Images presented in Figure 13 are maximum intensity projections.

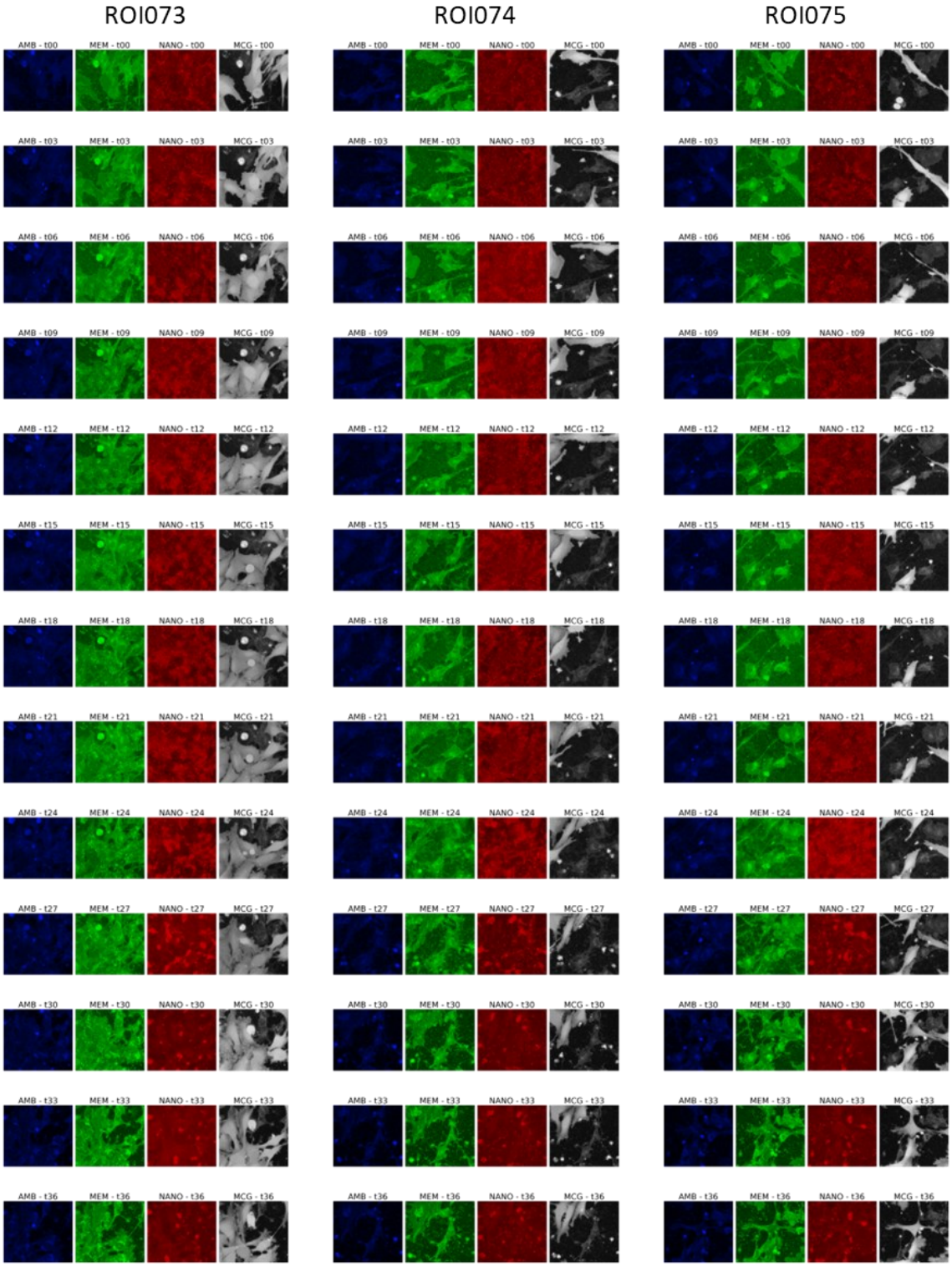

Figure S20: Images (133 x 133 μm2) of neurons and microglia co-culture from ROIs 73-75 presented in Figure 12 and analysed in Figure 13 of the main text are decomposed in separate channels. Neurons are represented in green (membrane label CellMask Orange), microglia in gray (cytoplasm label CytoTracker Green), TiO2 nanotubes in red (backscattering), and Aβ (primary antibody labelled with fluorescent Alexa-647) in blue colour.

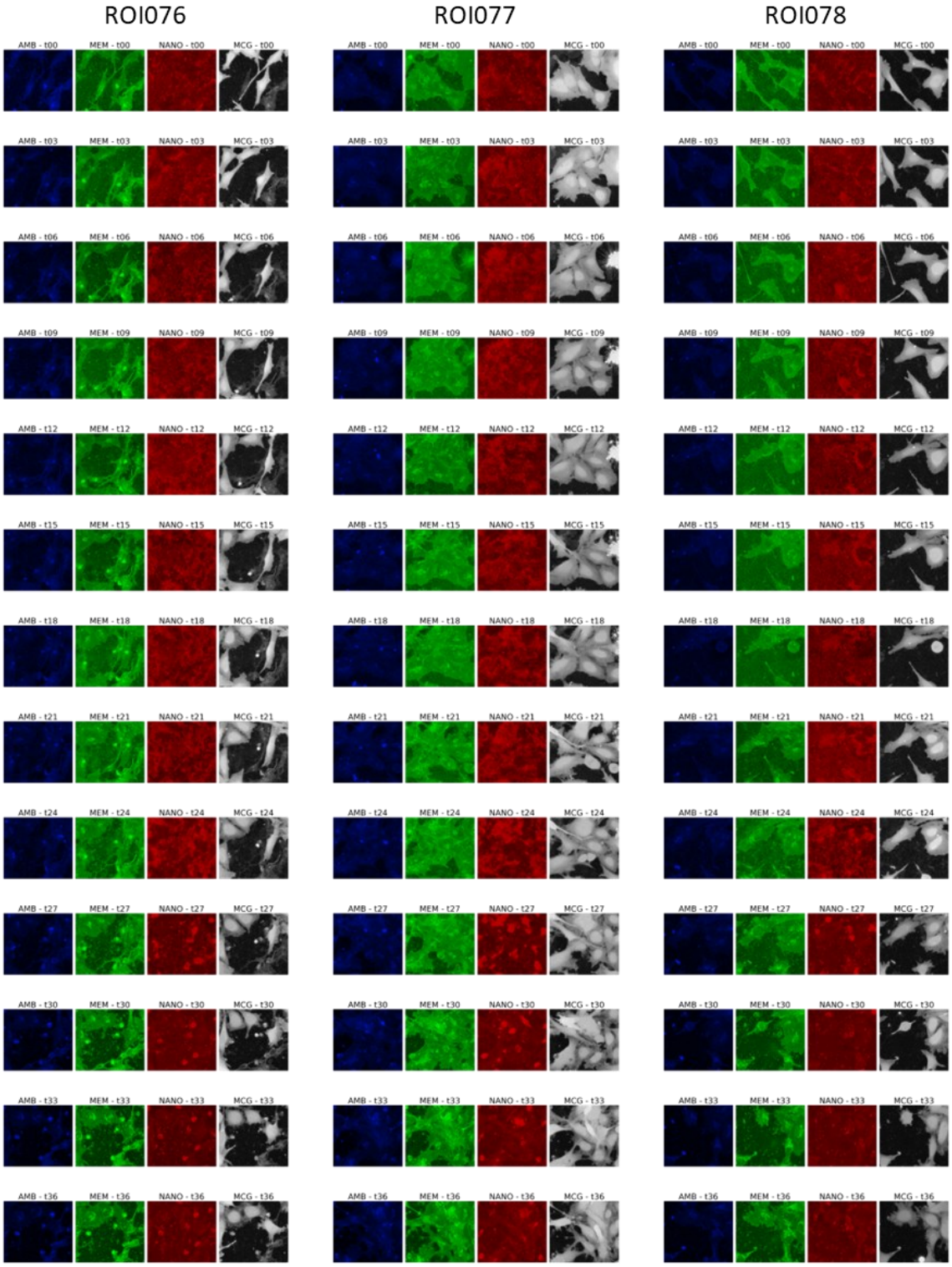

Figure S21: Images (133 x 133 μm2) of neurons and microglia co-culture from ROIs 77-78 presented in Figure 12 and analysed in Figure 13 of the main text are decomposed in separate channels. Neurons are represented in green (membrane label CellMask Orange), microglia in gray (cytoplasm label CytoTracker Green), TiO2 nanotubes in red (backscattering), and Aβ (primary antibody labelled with fluorescent Alexa-647) in blue colour.

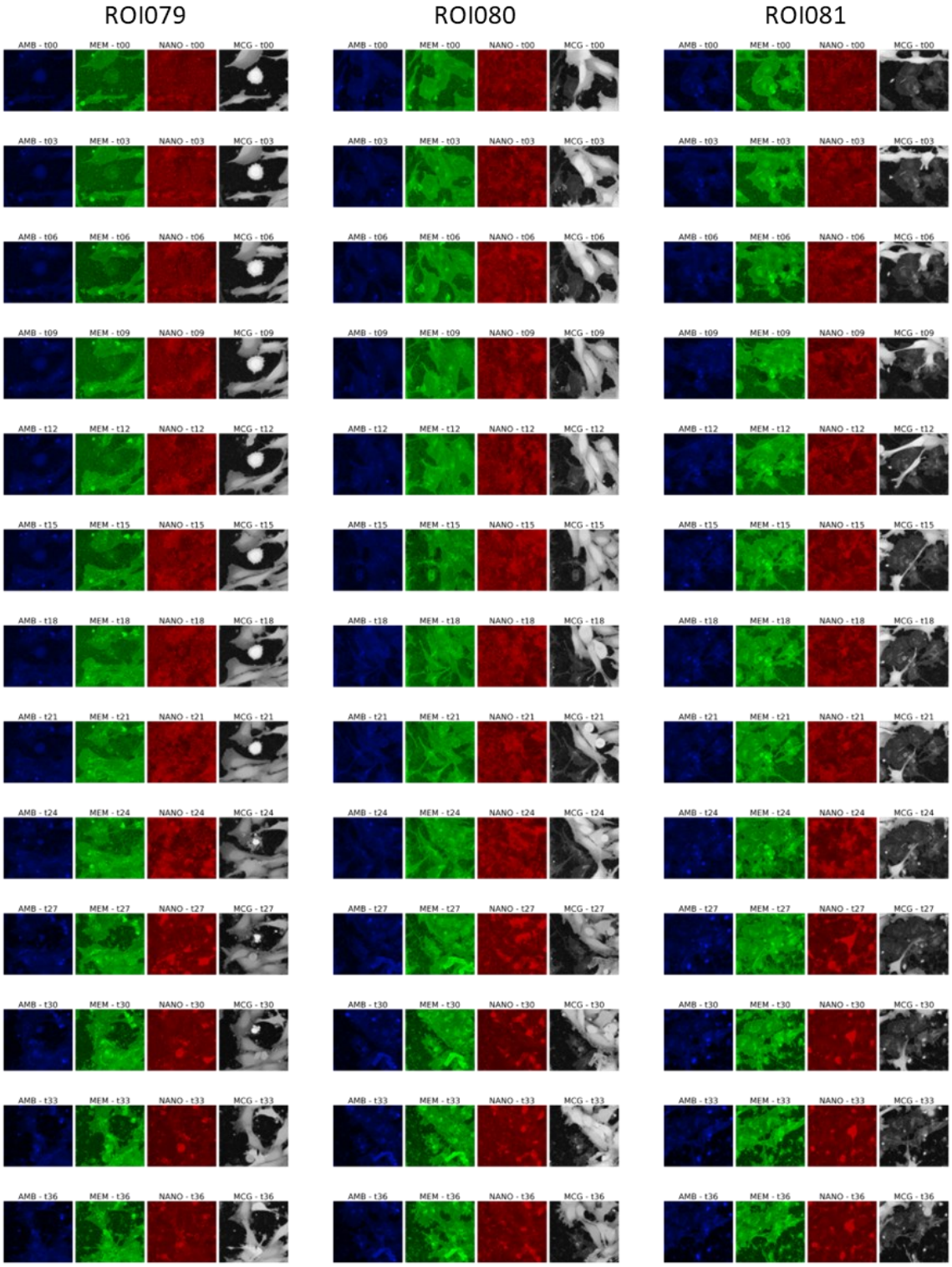

Figure S22: Images (133 x 133 μm2) of neurons and microglia co-culture from ROIs 79-81 presented in Figure 12 and analysed in Figure 13 of the main text are decomposed in separate channels. Neurons are represented in green (membrane label CellMask Orange), microglia in gray (cytoplasm label CytoTracker Green), TiO2 nanotubes in red (backscattering), and Aβ (primary antibody labelled with fluorescent Alexa-647) in blue colour.

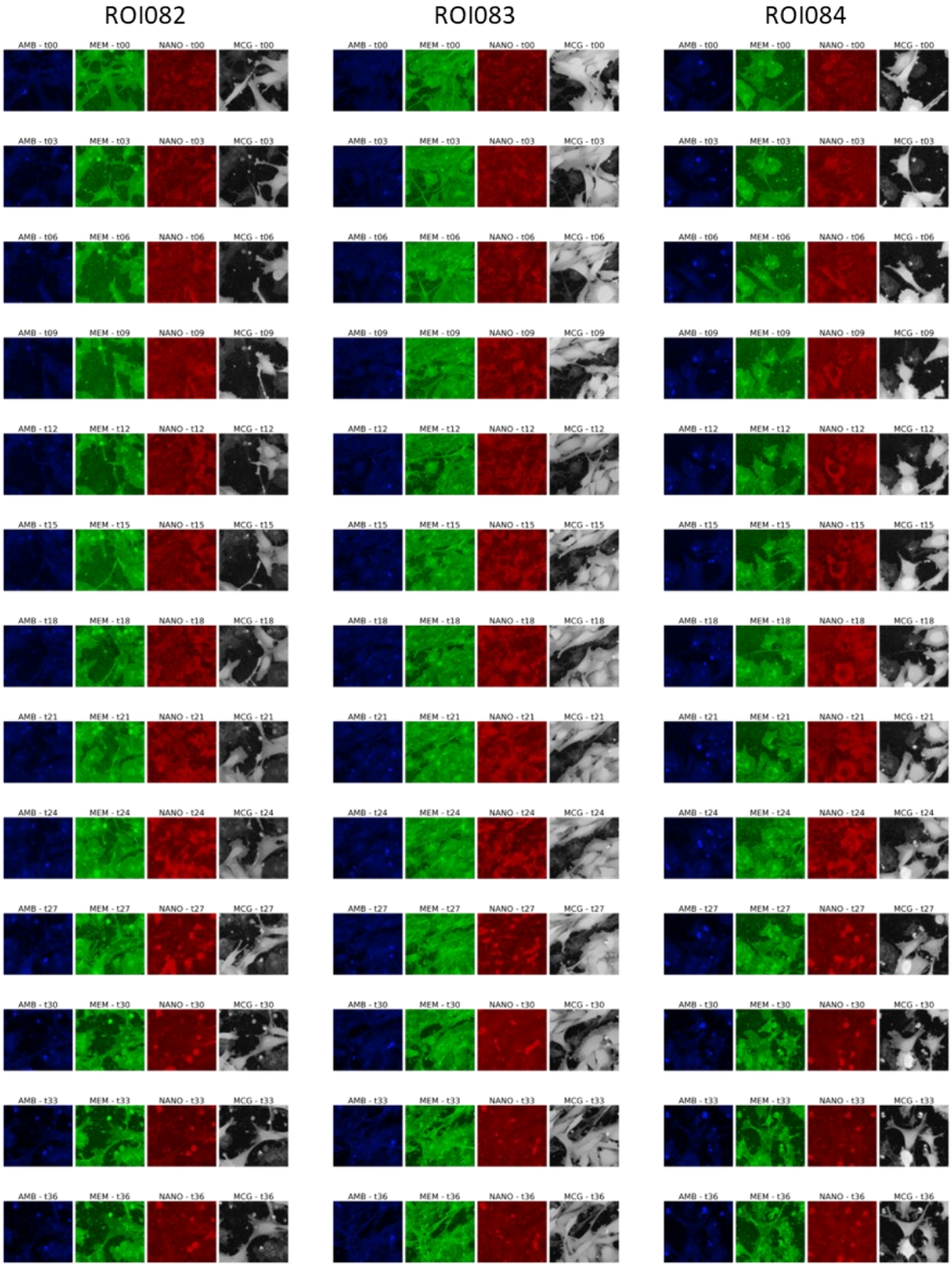

Figure S23: Images (133 x 133 μm2) of neurons and microglia co-culture from ROIs 82-84 presented in Figure 12 and analysed in Figure 13 of the main text are decomposed in separate channels. Neurons are represented in green (membrane label CellMask Orange), microglia in gray (cytoplasm label CytoTracker Green), TiO2 nanotubes in red (backscattering), and Aβ (primary antibody labelled with fluorescent Alexa-647) in blue colour.

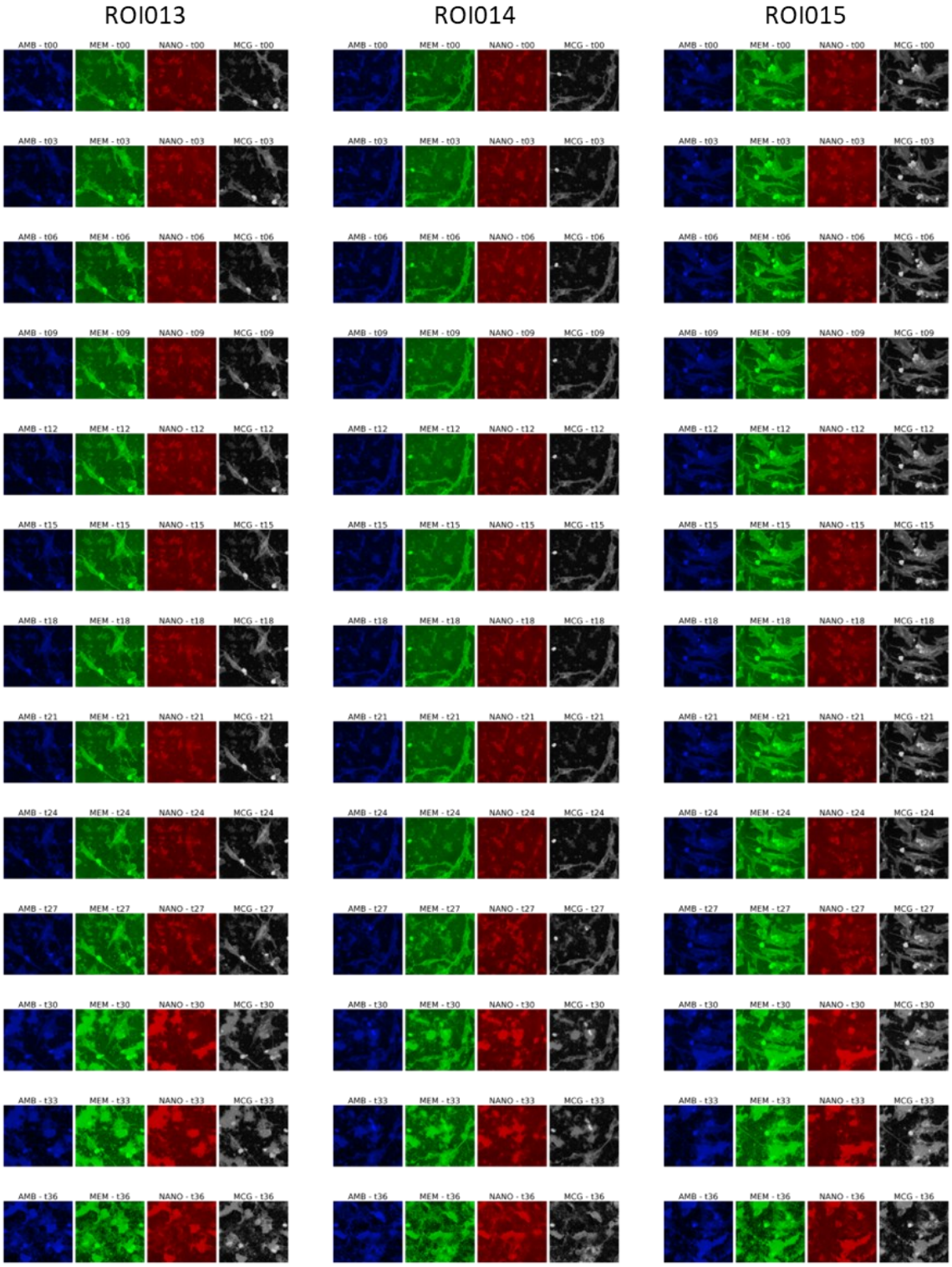

Figure S24: Images (133 x 133 μm2) of neurons monoculture from ROIs 13-15 presented in Figure 12 and analysed in Figure 13 of the main text are decomposed in separate channels. Neurons are represented in green (membrane label CellMask Orange), TiO2 nanotubes in red (backscattering), and Aβ (primary antibody labelled with fluorescent Alexa-647) in blue colour.

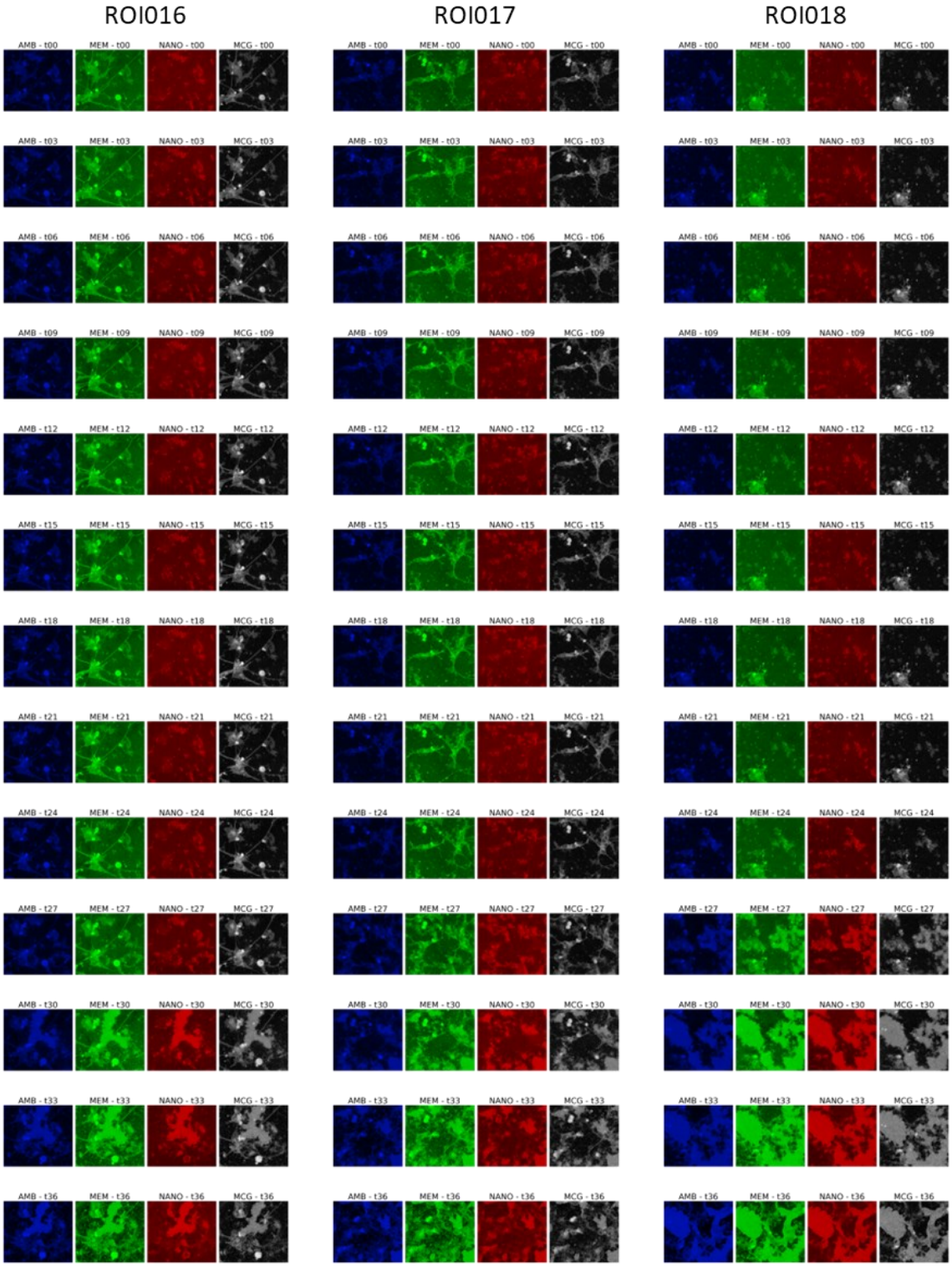

Figure S25: Images (133 x 133 μm2) of neurons monoculture from ROIs 16-18 presented in Figure 12 and analysed in Figure 13 of the main text are decomposed in separate channels. Neurons are represented in green (membrane label CellMask Orange), TiO2 nanotubes in red (backscattering), and Aβ (primary antibody labelled with fluorescent Alexa-647) in blue colour.

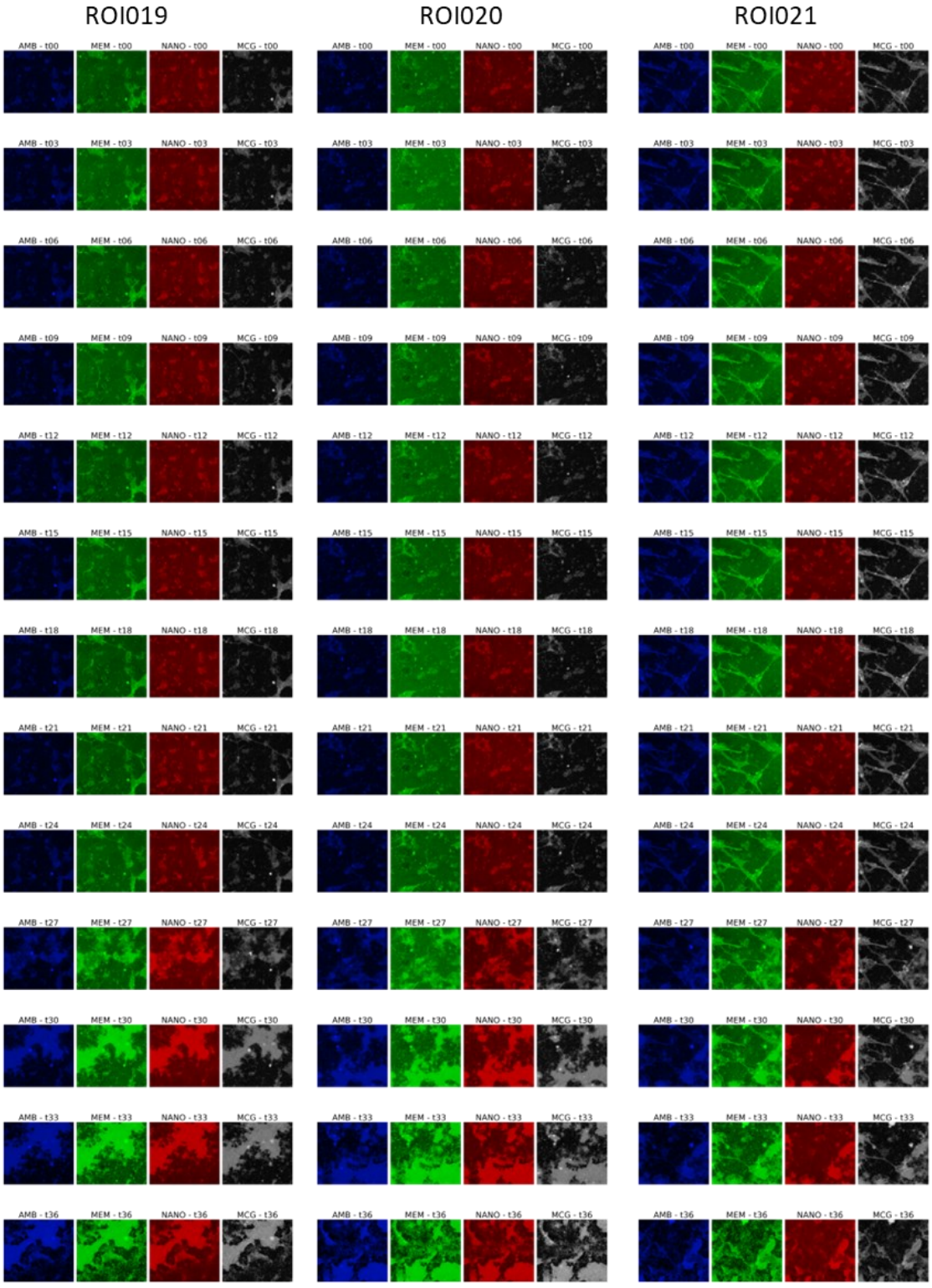

Figure S26: Images (133 x 133 μm2) of neurons monoculture from ROIs 19-21 presented in Figure 12 and analysed in Figure 13 of the main text are decomposed in separate channels. Neurons are represented in green (membrane label CellMask Orange), TiO2 nanotubes in red (backscattering), and Aβ (primary antibody labelled with fluorescent Alexa-647) in blue colour.

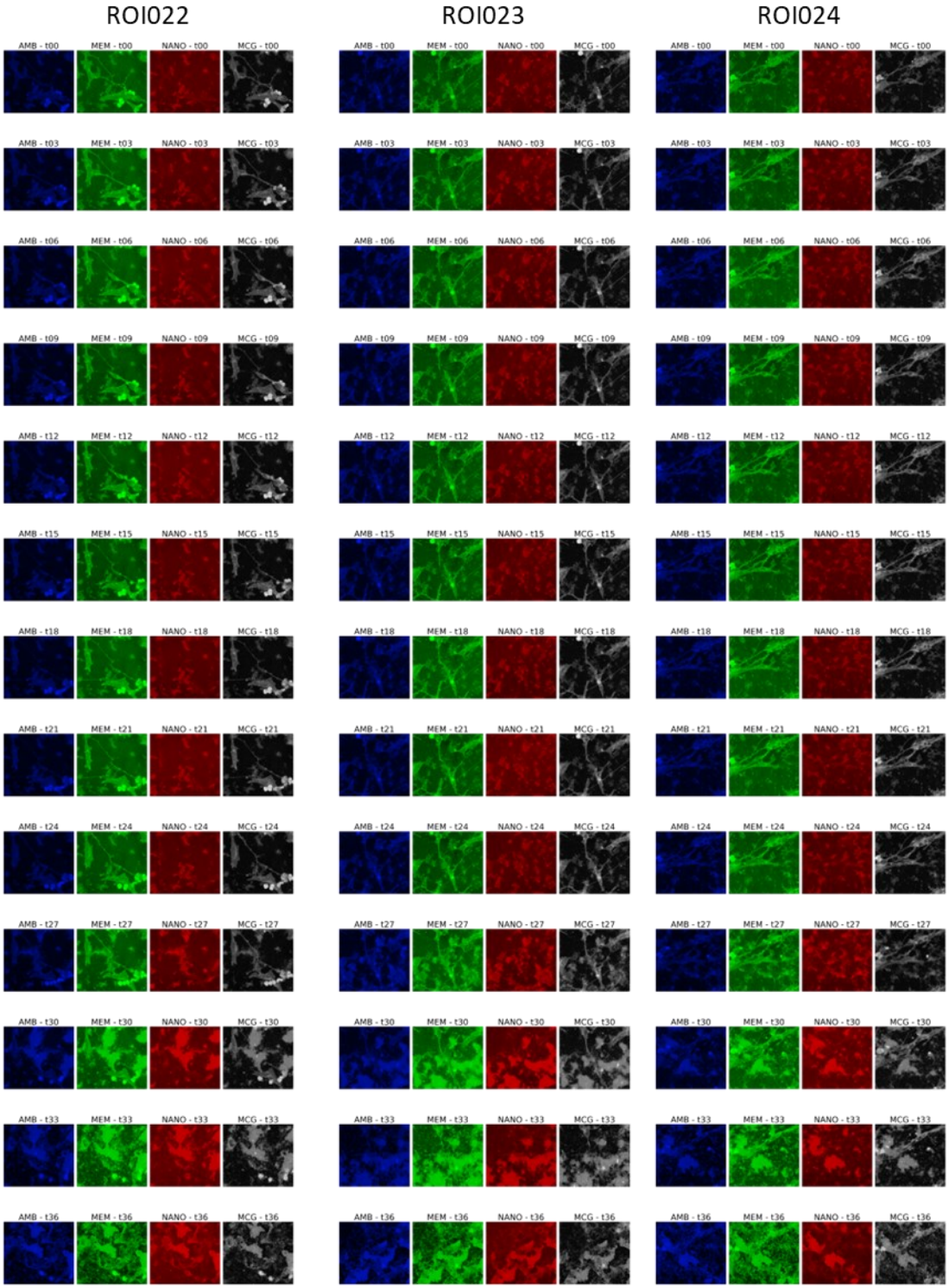

Figure S27: Images (133 x 133 μm2) of neurons monoculture from ROIs 22-24 presented in Figure 12 and analysed in Figure 13 of the main text are decomposed in separate channels. Neurons are represented in green (membrane label CellMask Orange), TiO2 nanotubes in red (backscattering), and Aβ (primary antibody labelled with fluorescent Alexa-647) in blue colour.

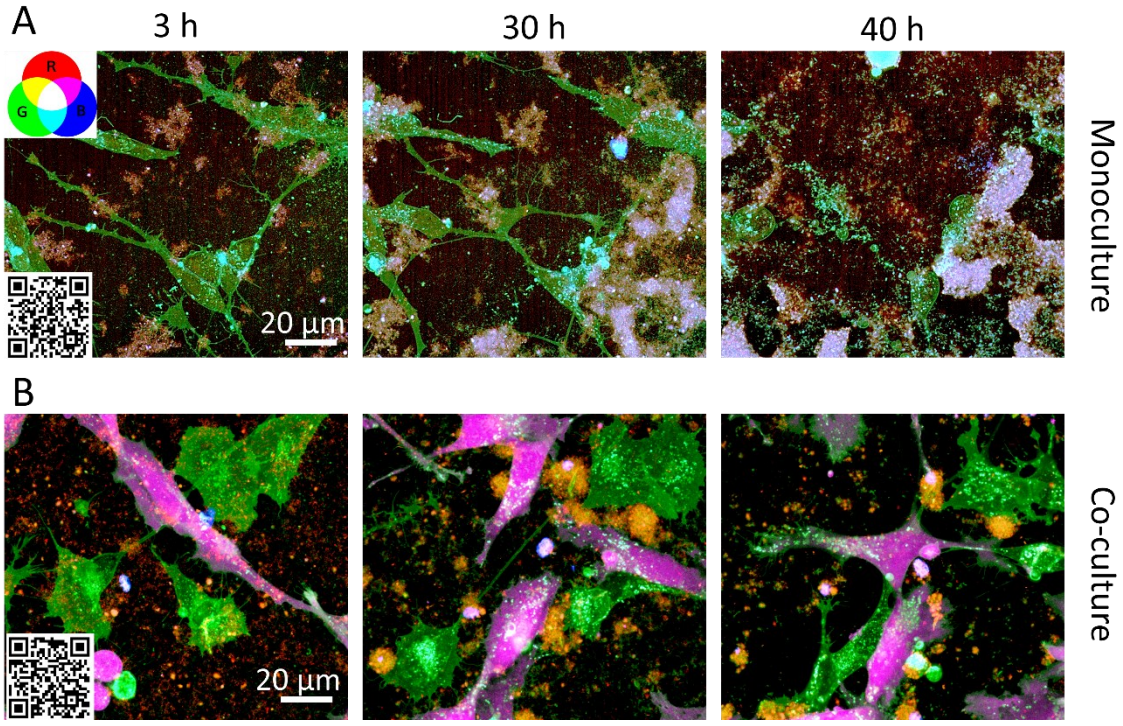

Figure S28: **Neurons in monoculture form large Aβ plaques, lose axons and die after the exposure to TiO2 nanotubes. In co-culture these outcomes are omitted**. Neurons were labelled with the plasma membrane label CMO (green), microglia with cytoplasmic CTG (magenta), Aβ (blue) with the Alexa-647 labelled primary antibody and nanotubes (red) were visualized via scattering detection. Aβ plaques are characterized by the co-localization of blue, red and green colour resulting in white-coloured objects, according to the mixing palette provided in the right upper corner of the 3h-image.

A) To view the whole video sequence of Aβ plaque formation in monoculture, please scan the QR code provided in the lower left corner. Screenshots at 3, 30 and 40 hours of a 40 hour-long time lapse of monoculture of neurons exposed to TiO_2 nanotubes. After 40 hours almost all neurons are dead. Those that remained have no axons. B) Scan the provided QR code to see the video of Aβ plaque formation in co-culture. In the presence of microglia, Aβ plaques are much smaller, more compact and neurons survive the exposure to TiO_2 nanotubes after 40 hours.

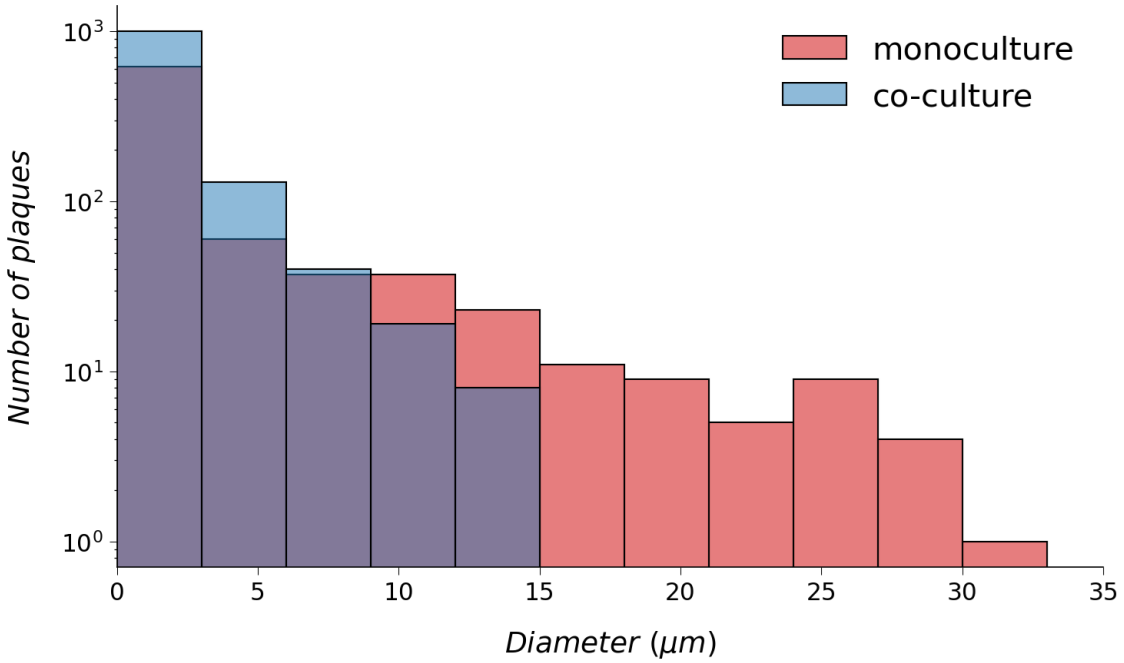

Figure S29: **Comparison of Aβ plaque sizes in monoculture of neurons (red) and co-culture of neurons and microglia (blue) following 40 hours of incubation with TiO2 nanotubes**. A total of 822 plaques were identified in the monoculture, while 1195 plaques were observed in the co-culture.

References

[1] P. Umek, R. C. Korošec, B. Jančar, R. Dominko, D. Arčon. The Influence of the Reaction Temperature on the Morphology of Sodium Titanate 1D Nanostructures and Their Thermal Stability. *J. Nanosci. Nanotechnol.*, 7, 10,3502–3508, 10, 2007, doi: 10.1166/jnn.2007.838.

[2] What Is Dementia?. Alzheimer's Disease and Dementia. DOI: 2022, 8, 17. https://alz.org/alzheimers-dementia/what-is-dementia

[3] What Is Dementia? CDC, 2022, 8, 17. https://www.cdc.gov/aging/dementia/index.html

[4] L. Drew. An age-old story of dementia. *Nature*, 559, 7715,S2–S3, 7, 2018, doi: 10.1038/d41586-018-05718-5.

[5] M. Vijayan, P. H. Reddy. Stroke, Vascular Dementia, and Alzheimer's Disease: Molecular Links. *J. Alzheimers Dis. JAD*, 54, 2,427–443, 9, 2016, doi: 10.3233/JAD-160527.

[6] J. Cummings. Alzheimer's disease drug development pipeline: 2022. *Alzheimers Dement. Transl. Res. Clin. Interv.*, 8, 1,e12295, 2022, doi: 10.1002/trc2.12295.

[7] G. Livingston. Dementia prevention, intervention, and care: 2020 report of the Lancet Commission. *The Lancet*, 396, 10248,413–446, 8, 2020, doi: 10.1016/S0140-6736(20)30367-6.

[8] W. J. P. Henneman. Hippocampal atrophy rates in Alzheimer disease: Added value over whole brain volume measures. *Neurology*, 72, 11,999–1007, 3, 2009, doi: 10.1212/01.wnl.0000344568.09360.31.

[9] M. L. Haaksma. Survival time tool to guide care planning in people with dementia. *Neurology*, 94, 5,e538–e548, 2, 2020, doi: 10.1212/WNL.0000000000008745.

[10] A. D. International, M. University. World Alzheimer Report 2021: Journey through the diagnosis of dementia. 9, 2021, DOI: 2022, 8, 17. https://www.alzint.org/resource/world-alzheimer-report-2021/

[11] B. Eftekharzadeh, B. T. Hyman, S. Wegmann. Structural studies on the mechanism of protein aggregation in age related neurodegenerative diseases. *Mech. Ageing Dev.*, 156,1–13, 6, 2016, doi: 10.1016/j.mad.2016.03.001.

[12] Liao, L. et al. Proteomic Characterization of Postmortem Amyloid Plaques Isolated by Laser Capture Microdissection. Journal of Biological Chemistry 279, 37061–37068 (2004).

[13] Amyloid precursor protein promotes post-developmental neurite arborization in the Drosophila brain. *EMBO J.*, 24, 16,2944–2955, 8, 2005, doi: 10.1038/sj.emboj.7600757.

[14] M. Gralle, S. T. Ferreira. Structure and functions of the human amyloid precursor protein: The whole is more than the sum of its parts. *Prog. Neurobiol.*, 82, 1,11–32, 5, 2007, doi: 10.1016/j.pneurobio.2007.02.001.

[15] J. Kang. The precursor of Alzheimer's disease amyloid A4 protein resembles a cell-surface receptor. *Nature*, 325, 6106, Art. 6106, 2, 1987, doi: 10.1038/325733a0.

[16] J. A. Hardy, G. A. Higgins. Alzheimer's disease: the amyloid cascade hypothesis. *Science*, 256, 5054,184–185, 4, 1992, doi: 10.1126/science.1566067.

[17] T. L. Spires. Dendritic spine abnormalities in amyloid precursor protein transgenic mice demonstrated by gene transfer and intravital multiphoton microscopy. *J. Neurosci.*, 25, 31,7278–7287, 2005, doi: 10.1523/JNEUROSCI.1879-05.2005.

[18] M. ten Kate. Gray matter network disruptions and regional amyloid beta in cognitively normal adults. *Front. Aging Neurosci.*, 10, FEB, 2018, doi: 10.3389/fnagi.2018.00067.

[19] M. Colom-Cadena. The clinical promise of biomarkers of synapse damage or loss in Alzheimer's disease. *Alzheimers Res. Ther.*, 12, 1,21, 3, 2020, doi: 10.1186/s13195-020-00588-4.

[20] M. M. Lipinski. Genome-wide analysis reveals mechanisms modulating autophagy in normal brain aging and in Alzheimer's disease. *Proc. Natl. Acad. Sci.*, 107, 32,14164–14169, 8, 2010, doi: 10.1073/pnas.1009485107.

[21] M. P. Lambert. Diffusible, nonfibrillar ligands derived from Aβ1–42 are potent central nervous system neurotoxins. *Proc. Natl. Acad. Sci. U. S. A.*, 95, 11,6448–6453, 5, 1998.

[22] F. A. Edwards. A Unifying Hypothesis for Alzheimer's Disease: From Plaques to Neurodegeneration. *Trends Neurosci.*, 42, 5,310–322, 5, 2019, doi: 10.1016/j.tins.2019.03.003.

[23] A. Khan, A. Corbett, C. Ballard. Emerging amyloid and tau targeting treatments for Alzheimer's disease. *Expert Rev. Neurother.*, 17, 7,697–711, 7, 2017, doi: 10.1080/14737175.2017.1326819.

[24] S. Hong. Complement and microglia mediate early synapse loss in Alzheimer mouse models. *Science*, 352, 6286,712–716, 5, 2016, doi: 10.1126/science.aad8373.

[25] B. Do Van. Ferroptosis, a newly characterized form of cell death in Parkinson's disease that is regulated by PKC. *Neurobiol. Dis.*, 94,169–178, 10, 2016, doi: 10.1016/j.nbd.2016.05.011.

[26] Seek - Against the grain. DOI: 2022, 9, 8. https://seek.rockefeller.edu/against-the-grain/

[27] D. Iacono. Neuronal Hypertrophy in Asymptomatic Alzheimer Disease. *J. Neuropathol. Exp. Neurol.*, 67, 6,578–589, 6, 2008, doi: 10.1097/NEN.0b013e3181772794.

[28] R. Ricciarelli, E. Fedele. The Amyloid Cascade Hypothesis in Alzheimer's Disease: It's Time to Change Our Mind. *Curr. Neuropharmacol.*, 15, 6,926–935, 8, 2017, doi: 10.2174/1570159X15666170116143743.

[29] E. E. Congdon, E. M. Sigurdsson. Tau-targeting therapies for Alzheimer disease. *Nat. Rev. Neurol.*, 14, 7,399–415, 7, 2018, doi: 10.1038/s41582-018-0013-z.

[30] O. V. Forlenza, V. J. R. De-Paula, B. S. O. Diniz. Neuroprotective Effects of Lithium: Implications for the Treatment of Alzheimer's Disease and Related Neurodegenerative Disorders. *ACS Chem. Neurosci.*, 5, 6,443–450, 4, 2014, doi: 10.1021/cn5000309.

[31] R. T. Makola, V. G. Mbazima, M. P. Mokgotho, V. S. Gallicchio, T. M. Matsebatlela. The Effect of Lithium on Inflammation-Associated Genes in Lipopolysaccharide-Activated Raw 264.7 Macrophages. *Int. J. Inflamm.*, 2020,8340195, 7, 2020, doi: 10.1155/2020/8340195.

[32] L. M. Callahan, W. A. Vaules, P. D. Coleman. Quantitative decrease in synaptophysin message expression and increase in cathepsin D message expression in Alzheimer disease neurons containing neurofibrillary tangles. *J. Neuropathol. Exp. Neurol.*, 58, 3,275–287, 3, 1999, doi: 10.1097/00005072-199903000-00007.

[33] E.-M. Mandelkow, K. Stamer, R. Vogel, E. Thies, E. Mandelkow. Clogging of axons by tau, inhibition of axonal traffic and starvation of synapses. *Neurobiol. Aging*, 24, 8,1079–1085, 12, 2003, doi: 10.1016/j.neurobiolaging.2003.04.007.

[34] G. Price, C. Udeh-Momoh, M. Kivipelto, L. T. Middleton. Editorial: Dementia Prevention: A Global Challenge in Urgent Need of Solutions. *J. Prev. Alzheimers Dis.*, 9, 1,1–2, 2022, doi: 10.14283/jpad.2022.10.

[35] R. M. Anderson, C. Hadjichrysanthou, S. Evans, M. M. Wong. Why do so many clinical trials of therapies for Alzheimer's disease fail?. *Lancet Lond. Engl.*, 390, 10110,2327–2329, 11, 2017, doi: 10.1016/S0140-6736(17)32399-1.

[36] L. Rolfes. Failed, Interrupted, or Inconclusive Trials on Immunomodulatory Treatment Strategies in Multiple Sclerosis: Update 2015–2020. *BioDrugs*, 34, 5,587–610, 10, 2020, doi: 10.1007/s40259-020-00435-w.

[37] J. L. Cummings, T. Morstorf, K. Zhong. Alzheimer's disease drug-development pipeline: few candidates, frequent failures. *Alzheimers Res. Ther.*, 6, 4,37, 7, 2014, doi: 10.1186/alzrt269.

[38] V. K. Gribkoff, L. K. Kaczmarek. The need for new approaches in CNS drug discovery: Why drugs have failed, and what can be done to improve outcomes. *Neuropharmacology*, 120,11–19, 7, 2017, doi: 10.1016/j.neuropharm.2016.03.021.

[39] A. Slanzi, G. Iannoto, B. Rossi, E. Zenaro, G. Constantin. *In vitro* Models of Neurodegenerative Diseases. *Front. Cell Dev. Biol.* 2022, 8, 17. https://www.frontiersin.org/articles/10.3389/fcell.2020.00328

[40] K. Blennow, M. J. de Leon, H. Zetterberg. Alzheimer's disease. *The Lancet*, 368, 9533,387–403, 7, 2006, doi: 10.1016/S0140-6736(06)69113-7.

[41] N. Fox, S. Love. Cognitive decline, dementia and air pollution: A report by the Committee on the Medical Effects of Air Pollutants. 291.

[42] J. Wang. Potential neurological lesion after nasal instillation of TiO(2) nanoparticles in the anatase and rutile crystal phases. *Toxicol. Lett.*, 183, 1–3,72–80, 12, 2008, doi: 10.1016/j.toxlet.2008.10.001.

[43] C. P. Ferri. Global prevalence of dementia: a Delphi consensus study. *Lancet*, 366, 9503,2112–2117, 12, 2005, doi: 10.1016/S0140-6736(05)67889-0.

[44] P. M. Mannucci, M. Franchini. Health Effects of Ambient Air Pollution in Developing Countries. *Int. J. Environ. Res. Public. Health*, 14, 9,1048, 9, 2017, doi: 10.3390/ijerph14091048.

[45] E. Underwood. The polluted brain. *Science*, 355, 6323,342–345, 1, 2017, doi: 10.1126/science.355.6323.342.

[46] L. Calderón-Garcidueñas. Hallmarks of Alzheimer disease are evolving relentlessly in Metropolitan Mexico City infants, children and young adults. APOE4 carriers have higher suicide risk and higher odds of reaching NFT stage V at ≤40 years of age. *Environ. Res.*, 164,475–487, 7, 2018, doi: 10.1016/j.envres.2018.03.023.

[47] G. Plascencia-Villa. High-resolution analytical imaging and electron holography of magnetite particles in amyloid cores of Alzheimer's disease. *Sci. Rep.*, 6, 1, Art. 1, 4, 2016, doi: 10.1038/srep24873.

[48] M. Lippmann, D. B. Yeates, R. E. Albert. Deposition, retention, and clearance of inhaled particles.. *Br. J. Ind. Med.*, 37, 4,337–362, 11, 1980.

[49] H. Kokot. Prediction of Chronic Inflammation for Inhaled Particles: the Impact of Material Cycling and Quarantining in the Lung Epithelium. *Adv. Mater.*, 32, 47,2003913, 2020, doi: 10.1002/adma.202003913.

[50] I. Urbančič. Nanoparticles Can Wrap Epithelial Cell Membranes and Relocate Them Across the Epithelial Cell Layer. *Nano Lett.*, 18, 8,5294–5305, 8, 2018, doi: 10.1021/acs.nanolett.8b02291.

[51] K. Borgmann-Winter. Translational potential of olfactory mucosa for the study of neuropsychiatric illness. *Transl. Psychiatry*, 5, 3, Art. 3, 3, 2015, doi: 10.1038/tp.2014.141.

[52] D. Lee, T. Minko. Nanotherapeutics for Nose-to-Brain Drug Delivery: An Approach to Bypass the Blood Brain Barrier. *Pharmaceutics*, 13, 12,2049, 11, 2021, doi: 10.3390/pharmaceutics13122049.

[53] L. Guillaud, S. E. El-Agamy, M. Otsuki, M. Terenzio. Anterograde Axonal Transport in Neuronal Homeostasis and Disease. *Front. Mol. Neurosci.* 2022, 9, 8. https://www.frontiersin.org/articles/10.3389/fnmol.2020.556175

[54] Z. J. Koles, K. D. McLeod, R. S. Smith. A study of the motion of organelles which undergo retrograde and anterograde rapid axonal transport in Xenopus. *J. Physiol.*, 328, 1,469–484, 1982, doi: 10.1113/jphysiol.1982.sp014278.

[55] C. Burckhardt, U. Greber. Virus Movements on the Plasma Membrane Support Infection and Transmission between Cells. *PLoS Pathog.*, 5,e1000621, 11, 2009, doi: 10.1371/journal.ppat.1000621.

[56] M. J. Lehmann, N. M. Sherer, C. B. Marks, M. Pypaert, W. Mothes. Actin- and myosin-driven movement of viruses along filopodia precedes their entry into cells. *J. Cell Biol.*, 170, 2,317–325, 7, 2005, doi: 10.1083/jcb.200503059.

[57] L. Rahman. Multi-walled carbon nanotube-induced genotoxic, inflammatory and pro-fibrotic responses in mice: Investigating the mechanisms of pulmonary carcinogenesis. *Mutat. Res. Toxicol. Environ. Mutagen.*, 823,28–44, 11, 2017, doi: 10.1016/j.mrgentox.2017.08.005.

[58] R. S. Wils, N. R. Jacobsen, U. Vogel, M. Roursgaard, A. Jensen, P. Møller. Pleural inflammatory response, mesothelin content and DNA damage in mice at one-year

after intra-pleural carbon nanotube administration. *Toxicology*, 499,153662, 11, 2023, doi: 10.1016/j.tox.2023.153662.

[59] M. S. P. Boyles. Multi-walled carbon nanotube induced frustrated phagocytosis, cytotoxicity and pro-inflammatory conditions in macrophages are length dependent and greater than that of asbestos. *Toxicol. In Vitro*, 29, 7,1513–1528, 10, 2015, doi: 10.1016/j.tiv.2015.06.012.

[60] G. S. Jeong. Networked neural spheroid by neuro-bundle mimicking nervous system created by topology effect. *Mol. Brain*, 8, 1,17, 3, 2015, doi: 10.1186/s13041-015-0109-y.

[61] P. J. Cheng-Hathaway. The Trem2 R47H variant confers loss-of-function-like phenotypes in Alzheimer's disease. *Mol. Neurodegener.*, 13,29, 6, 2018, doi: 10.1186/s13024-018-0262-8.

[62] C. Y. D. Lee. Elevated TREM2 Gene Dosage Reprograms Microglia Responsivity and Ameliorates Pathological Phenotypes in Alzheimer's Disease Models. *Neuron*, 97, 5,1032-1048.e5, 3, 2018, doi: 10.1016/j.neuron.2018.02.002.

[63] R. Krauss, T. Bosanac, R. Devraj, T. Engber, R. O. Hughes. Axons Matter: The Promise of Treating Neurodegenerative Disorders by Targeting SARM1-Mediated Axonal Degeneration. *Trends Pharmacol. Sci.*, 41, 4,281–293, 4, 2020, doi: 10.1016/j.tips.2020.01.006.

[64] M. Fricker, A. M. Tolkovsky, V. Borutaite, M. Coleman, G. C. Brown. Neuronal Cell Death. *Physiol. Rev.*, 98, 2, Art. 2, 4, 2018, doi: 10.1152/physrev.00011.2017.

[65] B. Wang, M. Huang, D. Shang, X. Yan, B. Zhao, X. Zhang. Mitochondrial Behavior in Axon Degeneration and Regeneration. *Front. Aging Neurosci.*, 13,650038, 3, 2021, doi: 10.3389/fnagi.2021.650038.

[66] Q. Cai, P. Tammineni. Mitochondrial Aspects of Synaptic Dysfunction in Alzheimer's Disease. *J. Alzheimers Dis. JAD*, 57, 4,1087–1103, 2017, doi: 10.3233/JAD-160726.

[67] V. E. Johnson, W. Stewart, D. H. Smith. Axonal pathology in traumatic brain injury. *Exp. Neurol.*, 246,35–43, 8, 2013, doi: 10.1016/j.expneurol.2012.01.013.

[68] B. Wang, M. Huang, D. Shang, X. Yan, B. Zhao, X. Zhang. Mitochondrial Behavior in Axon Degeneration and Regeneration. *Front. Aging Neurosci.*, 13,650038, 3, 2021, doi: 10.3389/fnagi.2021.650038.

[69] X. Shen, P. Sun, H. Zhang, H. Yang. Mitochondrial quality control in the brain: The physiological and pathological roles. *Front. Neurosci.* 2023, 5, 22. https://www.frontiersin.org/articles/10.3389/fnins.2022.1075141

[70] W. Wang, F. Zhao, X. Ma, G. Perry, X. Zhu. Mitochondria dysfunction in the pathogenesis of Alzheimer's disease: recent advances. *Mol. Neurodegener.*, 15, 1,30, 5, 2020, doi: 10.1186/s13024-020-00376-6.

[71] K. Itoh, K. Nakamura, M. Iijima, H. Sesaki. Mitochondrial Dynamics in Neurodegeneration. *Trends Cell Biol.*, 23, 2,64–71, 2, 2013, doi: 10.1016/j.tcb.2012.10.006.

[72] Y. Jin. Regrowth of Serotonin Axons in the Adult Mouse Brain Following Injury. *Neuron*, 91, 4,748–762, 8, 2016, doi: 10.1016/j.neuron.2016.07.024.

[73] H. Fu, Y. Zhao, D. Hu, S. Wang, T. Yu, L. Zhang. Depletion of microglia exacerbates injury and impairs function recovery after spinal cord injury in mice. *Cell Death Dis.*, 11, 7, Art. 7, 7, 2020, doi: 10.1038/s41419-020-2733-4.

[74] Amyloid precursor protein promotes post-developmental neurite arborization in the Drosophila brain. *EMBO J.*, 24, 16, Art. 16, 8, 2005, doi: 10.1038/sj.emboj.7600757.

[75] F. C. Alsina. Lrig1 is a cell-intrinsic modulator of hippocampal dendrite complexity and BDNF signaling. *EMBO Rep.*, 17, 4,601–616, 4, 2016, doi: 10.15252/embr.201541218.

[76] A few strong connections: optimizing information retention in neuronal avalanches | BMC Neuroscience. 2023, 8, 5. https://bmcneurosci.biomedcentral.com/articles/10.1186/1471-2202-11-3

[77] R. F. McCann, D. A. Ross. A Fragile Balance: Dendritic Spines, Learning, and Memory. *Biol. Psychiatry*, 82, 2,e11–e13, 7, 2017, doi: 10.1016/j.biopsych.2017.05.020.

[78] H. Hering, M. Sheng. Dentritic spines : structure, dynamics and regulation. *Nat. Rev. Neurosci.*, 2, 12, Art. 12, 12, 2001, doi: 10.1038/35104061.

[79] J. Noguchi. Bidirectional *in vivo*structural dendritic spine plasticity revealed by two-photon glutamate uncaging in the mouse neocortex. *Sci. Rep.*, 9, 1, Art. 1, 9, 2019, doi: 10.1038/s41598-019-50445-0.

[80] S.-J. R. Lee, Y. Escobedo-Lozoya, E. M. Szatmari, R. Yasuda. Activation of CaMKII in single dendritic spines during long-term potentiation. *Nature*, 458, 7236, Art. 7236, 3, 2009, doi: 10.1038/nature07842.

[81] M. Matsuzaki, N. Honkura, G. C. R. Ellis-Davies, H. Kasai. Structural basis of long-term potentiation in single dendritic spines. *Nature*, 429, 6993, Art. 6993, 6, 2004, doi: 10.1038/nature02617.

[82] T. Hayama. GABA promotes the competitive selection of dendritic spines by controlling local Ca2+ signaling. *Nat. Neurosci.*, 16, 10, Art. 10, 10, 2013, doi: 10.1038/nn.3496.

[83] J. Noguchi. State-dependent diffusion of actin-depolymerizing factor/cofilin underlies the enlargement and shrinkage of dendritic spines. *Sci. Rep.*, 6, 1, Art. 1, 9, 2016, doi: 10.1038/srep32897.

[84] Quantification of spread of cerebellar long-term depression with chemical two-photon uncaging of glutamate. PNAS, 2023, 8, 5. https://www.pnas.org/doi/10.1073/pnas.130414597

[85] Review Series: Developmental regulation of axon branching in the vertebrate nervous system. PMC, 2023, 5, 22. https://www.ncbi.nlm.nih.gov/pmc/articles/PMC3005597/

[86] B. W. Bernstein, J. R. Bamburg. ADF/cofilin: a functional node in cell biology. *Trends Cell Biol.*, 20, 4,187–195, 4, 2010, doi: 10.1016/j.tcb.2010.01.001.

[87] P. P. Tsitsopoulos, N. Marklund. Amyloid-β Peptides and Tau Protein as Biomarkers in Cerebrospinal and Interstitial Fluid Following Traumatic Brain Injury: A Review of Experimental and Clinical Studies. *Front. Neurol.*, 0, 2013, doi: 10.3389/fneur.2013.00079.

[88] G. Scott. Amyloid pathology and axonal injury after brain trauma. *Neurology*, 86, 9,821–828, 3, 2016, doi: 10.1212/WNL.0000000000002413.

[89] R. S. Duman, G. K. Aghajanian. Synaptic Dysfunction in Depression: Potential Therapeutic Targets. *Science*, 338, 6103,68–72, 10, 2012, doi: 10.1126/science.1222939.

[90] M. M. Dorostkar, C. Zou, L. Blazquez-Llorca, J. Herms. Analyzing dendritic spine pathology in Alzheimer's disease: problems and opportunities. *Acta Neuropathol. (Berl.)*, 130, 1,1–19, 2015, doi: 10.1007/s00401-015-1449-5.

[91] S. T. DeKosky, S. W. Scheff. Synapse loss in frontal cortex biopsies in Alzheimer's disease: correlation with cognitive severity. *Ann. Neurol.*, 27, 5,457–464, 5, 1990, doi: 10.1002/ana.410270502.

[92] R. D. Terry. Physical basis of cognitive alterations in Alzheimer's disease: synapse loss is the major correlate of cognitive impairment. *Ann. Neurol.*, 30, 4,572–580, 10, 1991, doi: 10.1002/ana.410300410.

[93] S. K. Shabestari. Absence of microglia promotes diverse pathologies and early lethality in Alzheimer's disease mice. *Cell Rep.*, 39, 11, 6, 2022, doi: 10.1016/j.celrep.2022.110961.

[94] M. Cortes-Canteli, L. Mattei, A. T. Richards, E. H. Norris, S. Strickland. Fibrin deposited in the Alzheimer's disease brain promotes neuronal degeneration. *Neurobiol. Aging*, 36, 2,608–617, 2, 2015, doi: 10.1016/j.neurobiolaging.2014.10.030.

[95] M. Merlini. Fibrinogen Induces Microglia-Mediated Spine Elimination and Cognitive Impairment in an Alzheimer's Disease Model. *Neuron*, 101, 6,1099-1108.e6, 3, 2019, doi: 10.1016/j.neuron.2019.01.014.

[96] E. Beem, M. S. Segal. Evaluation Of Stability And Sensitivity Of Cell Fluorescent Labels When Used for Cell Migration. *J. Fluoresc.*, 23, 5,975–987, 9, 2013, doi: 10.1007/s10895-013-1224-8.

[97] Z. He. Amyloid-β plaques enhance Alzheimer's brain tau-seeded pathologies by facilitating neuritic plaque tau aggregation. *Nat. Med.*, 24, 1, Art. 1, 1, 2018, doi: 10.1038/nm.4443.

[98] L. C. Walker. Aβ plaques. *Free Neuropathol.*, 1,31–31, 10, 2020, doi: 10.17879/freeneuropathology-2020-3025.

[99] A. Pensalfini. Intracellular amyloid and the neuronal origin of Alzheimer neuritic plaques. *Neurobiol. Dis.*, 0,53–61, 11, 2014, doi: 10.1016/j.nbd.2014.07.011.

[100] J.-H. Lee. Faulty autolysosome acidification in Alzheimer's disease mouse models induces autophagic build-up of Aβ in neurons, yielding senile plaques. *Nat. Neurosci.*, 25, 6, Art. 6, 6, 2022, doi: 10.1038/s41593-022-01084-8.

[101] B. Bai. Proteomic landscape of Alzheimer's Disease: novel insights into pathogenesis and biomarker discovery. *Mol. Neurodegener.*, 16, 12, 2021, doi: 10.1186/s13024-021-00474-z.

[102] F. Xiong, W. Ge, C. Ma. Quantitative proteomics reveals distinct composition of amyloid plaques in Alzheimer's disease. *Alzheimers Dement.*, 15, 3,429–440, 3, 2019, doi: 10.1016/j.jalz.2018.10.006.

[103] B. Tahirbegi. A Novel Aβ40 Assembly at Physiological Concentration. *Sci. Rep.*, 10, 1, Art. 1, 6, 2020, doi: 10.1038/s41598-020-66373-3.

[104] A. Serrano-Pozo. Stable Size Distribution of Amyloid Plaques Over the Course of Alzheimer Disease. *J. Neuropathol. Exp. Neurol.*, 71, 8,694–701, 8, 2012, doi: 10.1097/NEN.0b013e31825e77de.

[105] The role of myelin damage in Alzheimer's disease pathology - PMC. DOI: 2023, 7, 20. https://www.ncbi.nlm.nih.gov/pmc/articles/PMC7069444/

[106] C. Depp. Myelin dysfunction drives amyloid-β deposition in models of Alzheimer's disease. *Nature*, 618, 7964, Art. 7964, 6, 2023, doi: 10.1038/s41586-023-06120-6.

Bibliography

KOKOT, Hana, KOKOT, Boštjan, SEBASTIJANOVIĆ, Aleksandar, PODLIPEC, Rok, KRIŠELJ, Ana, ČOTAR, Petra, PUŠNIK, Mojca, UMEK, Polona, PAJK, Stane, URBANČIČ, Iztok, KOKLIČ, Tilen, ŠTRANCAR, Janez, et al. Prediction of chronic inflammation for inhaled particles: the impact of material cycling and quarantining in the lung epithelium. *Advanced materials*. [Online ed.]. 2020, vol. 32, no. 47, str. 2003913-1-2003913-15. ISSN 1521-4095. DOI: 10.1002/adma.202003913. [COBISS.SI-ID 39713539], [JCR, SNIP, WoS up to 8. 5. 2022: no. of citations (TC): 6, without self-citations (CI): 2, without self-citations per author (CIAu): 0,13, Scopus up to 18. 5. 2022: no. of citations (TC): 7, without self-citations (CI): 3, without self-citations per author (CIAu): 0,20]

ŠKET, Robert, PREVORŠEK, Zala, KOŠETO, Deni, SEBASTIJANOVIĆ, Aleksandar, OPARA, Simona, BAJUK, Jerca, STRES, Blaž. Analitski in konceptualni izzivi pri raziskovanju človeške črevesne mikrobiote za potrebe personalizirane večnivojske medicine = Analytical and conceptual challenges in the investigation of human intestinal microbiota for the needs of personalized multidimensional medicine. Medicinski razgledi : [medicinski pregledni, strokovni in raziskovalni članki]. [Tiskana izd.]. 2019, letn. 58, št. 2, str. 211-234, ilustr. ISSN 0025-8121. [COBISS.SI-ID 8932193]

SEBASTIJANOVIĆ, Aleksandar, HLAWACEK, Gregor, MALMBORG, Vilhelm, KRALJ, Slavko, PAGELS, Joakim, VOGEL, Ulla, ZIENOLDDINY-NARUI, Shan, URBANČIČ, Iztok, ŠTRANCAR, Janez. Particulate matter triggers the formation of extracellular amyloid-β and tau-containing plaques and neurite shortening *in vitro*. [Manuscript submitted for publication]

PODLIPEC, Rok, SEBASTIJANOVIĆ, Aleksandar, HILARY, Cassidy, LIANYONG, Han, ČOTAR, Petra, KOKOT, Hana, KOROŠEVIČ, KOSER, Benjamin, VENCELJ, Ana, PIRKER, Luka, UMEK, Polona, HLAWACEK, Gregor, HELLER, Rene, MATALLANAS, David, PELICON, Primoz, STOEGER, Tobias, URBANČIČ, Iztok, VOGEL, Ulla, KOKLIČ, Tilen, ŠTRANCAR, Janez. Genetic instability and carcinogenesis of high aspect ratio TiO_2 nanoparticles originates in cell cycle dysregulation by microtubule disruption and septin binding. [Manuscript submitted for publication]

JANEŽ, Nika, STERNIŠA, Meta, JUG, Blaž, ZUPAN, Tanja, SEBASTIJANOVIĆ, Aleksandar, PERIŠIĆ, NANUT, Milica, KARNIČAR, Katarina, TALER-VERČIČ, Ajda, TURK, Dušan, KLANČNIK, Anja, ŠTRANCAR, Janez. Fungal lectins and protease inhibitors interfere with biofilm development of Listeria monocytogenes and *Listeria innocua*. [Manuscript submitted for publication]